6-2014

Mechanical Routes to Biocontinuous Conductive Polymer Networks for Solar Cell Applications

Erin Waterman
Union College - Schenectady, NY

MECHANOCHEMICAL ROUTES TO BICONTINUOUS CONDUCTIVE POLYMER NETWORKS FOR SOLAR CELL APPLICATIONS

By

Erin R. Waterman

* * * * * * *

Submitted in partial fulfillment
of the requirements for
Honors in the Department of Chemistry

UNION COLLEGE
June 2014

ABSTRACT

WATERMAN, ERIN Mechanochemical Route to Bicontinuous Conductive Polymer Networks for Solar Cell Applications. Department of Chemistry, June 2014.

ADVISOR: Professor Michael Hagerman

We have successfully created the first example of a bicontinuous conductive polymer network for use in hybrid QD-polymer solar cells via a mechanochemical route. Heterometallic dicyanoaurate coordination polymers were used as intercalative hosts to promote in situ growth of emeraldine polyaniline (PANI), which provides electron conduction pathways within the active layer. Cu^{2+}-excanged Laponite RD nanodiscs were used to direct the self-assembly of the bicontinuous polymer networks and nanomorphology within the nanocomposites. These PANI/Laponite coordination polymers were extensively characterized by scanning electron microscopy, attenuated total reflectance-Fourier transform infrared spectroscopy, and ultraviolet-visible absorption spectroscopy in order to probe polymer-nanoparticle and polymer-polymer interactions. PANI and Laponite both serve to template the coordination polymer composites. Nano- and microstructures ranging from flowers to hollow spheres to wires-upon-wires growth were observed. Several bulk heterojunction solar cell active layers were synthesized by mixing varying ratios of the PANI/Laponite coordination polymer with poly(3,4-ethylenedioxythiophene):polystyrene sulfonate (PEDOT:PSS), a hole-conductive polymer, and tris(bipyridine)ruthenium(II) chloride (Rubipy), a chromophore. These active layers were used to fabricate bulk heterojunction solar cells. Future work will include making conductivity measurements on these solar cells, as well as fabricating new solar cells with incorporated CdSe quantum dots. The ability to tune

Au–Au aurophilic and Au-Se interactions may enhance the monodispersion of semiconductor nanoparticle chromophores, leading to improved photoconductivity.

ACKNOWLEDGEMENTS

There are so many people who deserve thanks for this work. First and foremost, I would like to thank my advisor, Professor Michael Hagerman. Professor Hagerman got me started in research when I was still a freshman, helped me to discover my love for nanoscience and materials chemistry, and let me play on the SEM for three years. So much of my personal and academic growth over my college career can be attributed to him; thank you, thank you, thank you!

I would like to thank the rest of the HagerLeague for their help with various aspects of my research over the last three years. A special thanks goes to Suan Quah, who helped me a lot during my thesis. I know she'll do a great job with the project in the future. I would also like to thank Professor Kehlbeck for her expertise on the solar project. Mark Hooker helped me so much with the SEM. I'd like to thank him for his patience and advice. Thanks to the NSF for funding the Interdisciplinary Research Instrumentation Suite (IRIS), which includes the SEM and AFM.

Of course, all of my professors should be thanked for sharing their knowledge and with me. All of them are so passionate about teaching and about their course material, and they have inspired me to choose academia as my career path.

Last, but certainly not least, I would like to thank my friends and family. Without the support, love, and kindness of each and every one of you, I never would have made it this far.

Table of Contents

TABLE OF FIGURES AND TABLES

TABLE	TABLE LEGEND	PAGE
1	Active layer components for six BHJs.	25

1. INTRODUCTION

1.1. The Worldwide Energy Crisis

The world is facing an energy crisis. Worldwide economic growth creates an enormous demand for energy, and that energy no longer comes cheaply. Gas and oil prices have skyrocketed, and these non-renewable fuel sources come at an environmental cost as well. We are consuming oil at four times the rate that we are discovering new oil.[1] In addition, the world energy consumption rate is projected to grow by 1.5% per year, or from 13.5 TW in 2001 to 27 TW by 2050 and to 43 TW by 2100.[2a] While there remains enough fossil energy sources to support this energy consumption rate for a few centuries, the use of these resources is causing a growth in the world's carbon emission rate at the expense of the environment. In fact, the world's carbon emission rate is expected to rise from 6.6 Gt of C per year in 2001 to 11 Gt of C per year in 2050.[2a] Renewable energy sources have gained a lot of attention because if an efficient enough process were to be found, it would eliminate both the need to rely on non-renewable energy sources and the environmental contamination from the combustion of fossil fuels. According to the Energy Information Administration, in 2008, the United States obtained 93% of its energy from non-renewable sources, including petroleum, natural gas, coal, and nuclear power.[2b] Of the 7% of its energy that is renewable, only 1% of that energy came from solar power (Figure 1). Despite the fact that the United States obtains so little of its energy supply from solar energy, it is the most viable form of renewable energy, with 3×10^{24} J of energy striking the Earth per year, 10,000 times more than the world's population is consuming.[3]

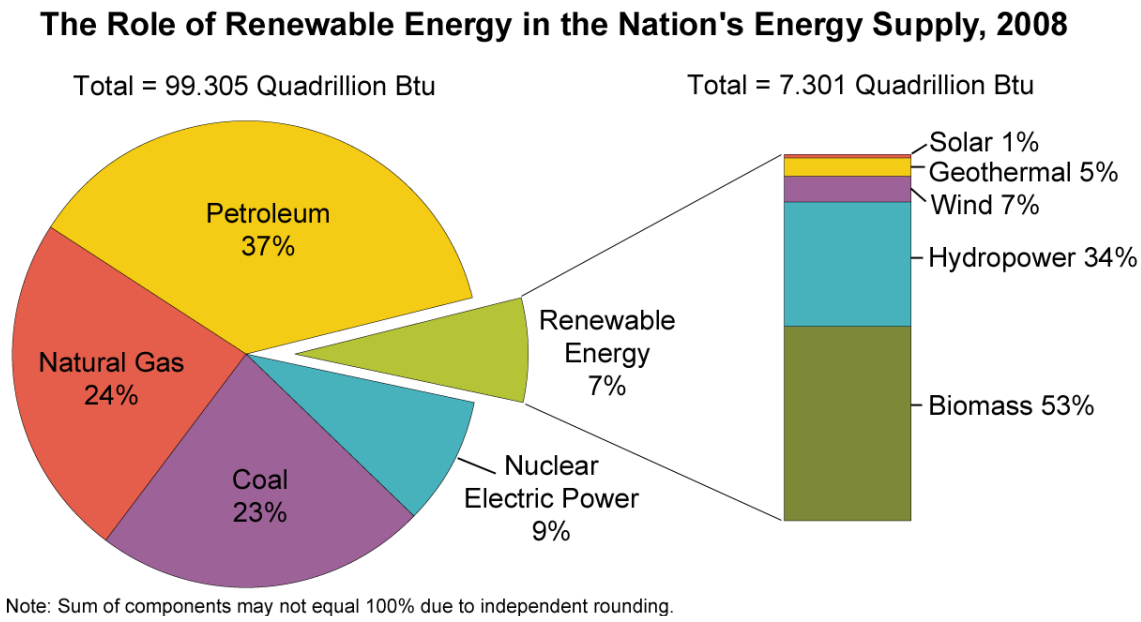

Figure 1. The breakdown of the United States' energy supply. Only 7% of the energy supply is renewable energy. Of that 7%, only 1% comes from solar energy.[2b]

Considerable research has been invested in harvesting solar energy. First-generation solar cells are the familiar single-crystalline silicon devices. While these devices have reasonable efficiencies (15-20%), they are too expensive for widespread use. Second-generation solar cells are $CuInGaSe_2$ thin film semiconductors. While these devices are much less expensive than the first-generation solar cells, they are also much less efficient. Currently, third-generation solar cells are being explored. These devices should be both efficient and inexpensive.[1] In the following sections, we will explore these options in more detail and examine a new synthetic route to realize novel solar materials.

1.2. Generations of Solar Materials: A Brief History

The French scientist Edmond Becquerel first discovered the photoelectric effect in 1839.[3] Simply stated, the photoelectric effect means that atoms will eject electrons when

exposed to light. Furthermore, photons interacting with a semiconductor will give rise to an exciton, or an electron/hole pair. This electron/hole pair is held together by Coulombic forces, and cannot separate very far without recombining and releasing their energy. In photovoltaic devices, the semiconductor should lie at a junction between two materials in order to facilitate charge separation.[3]

Several parameters are used to measure the efficiency of solar cells. These factors are determined from a current-voltage (J-V) curve. first parameter that can be determined from this curve is the short-circuit current (J_{SC}).[4] J_{SC} is defined as the current through the solar cell when there is no voltage across the cell because it is short circuited. J_{SC} is determined from the J-V curve as the maximum current when V = 0. Open-circuit voltage (V_{OC}) is another parameter determined from J-V curves. V_{OC} is defined as the maximum voltage available from a solar cell when there is no current. V_{OC} is a measure of forward bias on the solar cell. [4] It is determined from the J-V curve as the maximum voltage when J = 0. Fill factor (FF) is the third parameter determined from J-V curves. FF is the ratio of the maximum power generated by a solar cell to the product of J_{SC} and V_{OC}. More generally, it is the largest area rectangle that will fit inside a J-V curve. Finally, efficiency (η) can be determined. η is the ratio of the energy output of a solar cell to the input of energy from the sun and depends on many factors, such as the intensity of incident sunlight and temperature of the solar cell. It is usually measured under AM 1.5 conditions, with a temperature of 25 °C. [4] Thus, in order for a solar cell to be efficient, J_{SC}, V_{OC}, and FF must all be optimized.

An example of a J-V curve is shown in Figure 2.[5] In this case, the authors were testing the efficiency of CNT fiber solar cells. The annealed Pt-CNT yarn was found to

be the best option over CNT yarn and non-annealed Pt-CNT yarn because J_{SC}, V_{OC}, FF were optimized, leading to the highest η. It can be seen that the J-V curve for the annealed Pt-CNT yarn is the most "square," which indicates the highest FF.

Charge separation in third-generation solar cells can be optimized in many different ways. Three types of these third-generation devices that have garnered a lot of attention in recent years are dye-sensitized solar cells, bulk heterojunction solar cells, and fiber solar cells. These are the focus of the next sections.

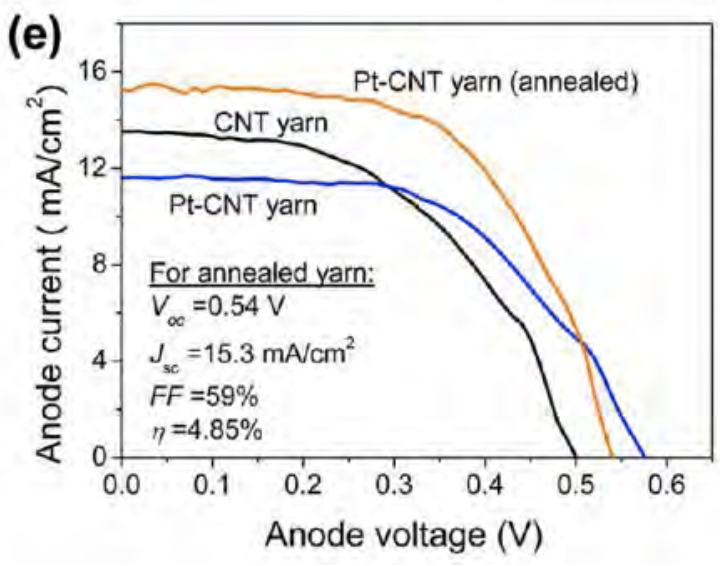

Figure 2. A J-V plot from Zhang, et al.[5] Annealed Pt-CNT yarn was found to be the optimal material for the fiber solar cells because it led to optimized J_{SC}, V_{OC}, FF and, therefore, η.

1.2.1. Dye-Sensitized Solar Cells

Dye-sensitized solar cells (DSSCs) are a class of solar cells in which a dye material is used to sensitize a semiconductor material. TiO_2 is commonly used as the semiconductor because it is very chemically stable and inexpensive, but a sensitizer is often needed, because TiO_2 itself only absorbs ultraviolet (UV) light. R.C. Nelson

discovered in 1965 that, for maximum charge-transfer efficiency, the dye should be adsorbed on the surface of a thin film of the semiconductor material.[6] The true breakthrough for efficient DSSCs came in 1991, witht the use of a mesoporous TiO_2-coated electrode. This electrode has a high internal surface area, which greatly increases efficiency, and supports a monolayer of dye sensitizer.[7] Other meso- and nanostructured metal oxides, such as ZnO or SnO_2, have also been used.[7] DSSCs also feature a liquid electrolyte to balance charge and oxidation-reduction reactions.[7] There are many factors that affect the perfomance of a DSSC and must be taken into consideration when constructing one.

There are several modes of electron-transfer processes in a DSSC. A few are listed here. One of these modes is the injection of an electron from the dye to the conduction band of the TiO_2 semiconductor.[7] This process occurs at the femptosecond time scale. Another mode of electron transfer is electron transport through the mesoporous oxide semiconductor film.[7] Yet another mode is the redox couple between the liquid electrolyte and the semiconductor.[7] Understanding which modes of electron transfer are at work in a particular system will help to optimize the efficiency of a DSSC.

Another factor to consider for a DSSC is the relative positions of the energy levels at the oxide/dye/electrolyte interface. Figure 3 shows an example of an energy level diagram for a DSSC.[7] The energy levels between materials must align in such a way as to minimize the energy for an electron to flow from one electrode to the other. The choice of photosensitizer dye for a particular system is also very important. The dye should absorb light over the entire visible region, and ideally through part of the near-IR. The dye should also be functionalized with specific anchoring groups to bind it to the

semiconductor. The dye also cannot aggregate, so the surface of the dye should be further functionalized to prevent this.[7]

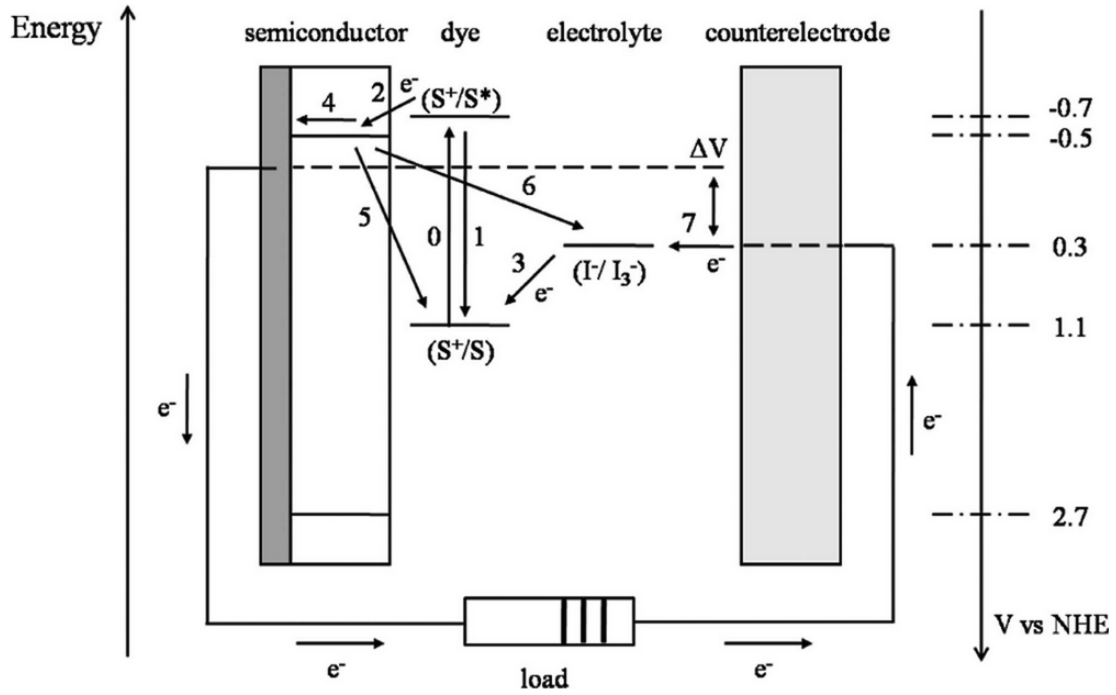

Figure 3. An energy level diagram for a DSSC. The numbers 1-7 indicate different electron-transfer processes. The potentials listed at the right are for a DSSC with the N3 dye, TiO_2 semiconductor, and I^-/I_3^- electrolyte.[7]

The most well-known example of a DSSC is the Grätzel cell (Figure 4).[8a] In the Grätzel cell, TiO_2 nanoparticles are coated on a transparent, conductive glass, indium tin oxide (ITO). The TiO_2 nanoparticles are sensitized with a ruthenium dye. When light strikes the dye, an exciton is generated. The electron must travel through the TiO_2 layers to the ITO electrode, while the hole must travel through the aqueous electrolyte (I_3^-/I^-) to the Pt cathode.[8b]

There are several drawbacks to the Grätzel cell design: first, the liquid electrolyte means that the cell may be unusable in colder climates; second, while most of the materials used in the device are low-cost, the Ru dye and Pt cathode are quite expensive;

third, the use of volatile organic compounds (VOCs) means that the design is not very environmentally-friendly. Because of these drawbacks, scientists have been searching for alternative designs.

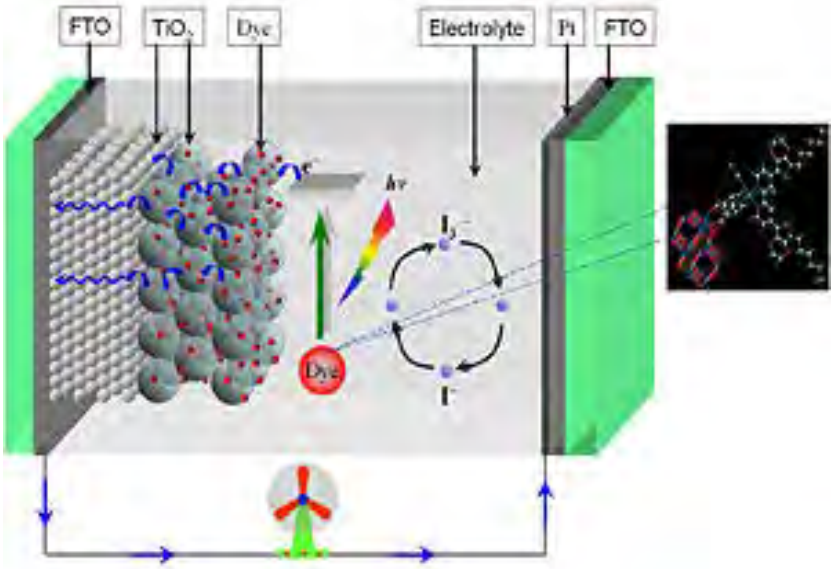

Figure 4. A Grätzel cell. The TiO_2 is shown coated on the electrode surface, with dye molecules adsorbed on the surface of the TiO_2. The structure of the dye molecule is shown at right. The electrolyte reaction between I_3^- and I^- is shown. Pt is coated on the counter-electrode. In this image, ITO is replaced with FTO, fluorine-doped tin oxide.[8a]

1.2.2. Fiber Solar Cells

Another class of third-generation solar cells now being explored is the fiber solar cell (FSC). FSCs are promising because they are highly scalable and flexible, so they can be integrated into clothing or other woven fabrics and portable electronics or covered over irregular surfaces.[9-15] This means that FSCs can be used in many applications that would not be possible for DSSCs. However, many FSCs still rely on the use of a liquid electrolyte and the same general set-up of DSSCs, so they would have the same disadvantages as DSSCs in that regard. Figure 5 shows the working mechanism of a fiber

solar cell constructed by Chen, et al.[12] The cell still uses a TiO_2 nanoparticle layer functionalized with dye molecules and an I^-/I_3^- liquid electrolyte, as with Grätzel cells. The FSCs that do use a DSSC set-up face another problem. The fibers must be in contact with a planar Pt electrode. Pt is commonly used as a counter electrode because it has a favorable work function when compared to ITO.[3] Obviously, there is poor contact between a planar Pt electrode and a fiber, which will result in reduced efficiency and conductivity overall because the planar electrode fails to collect the charges from the fibers.[15] Therefore, some groups have also created fiber counter electrodes to use for increased effective contact area.[9,15] In one study, replacing the planar Pt electrode with a cylindrical one resulted in an increase in efficiency of 3.6 times and resulted in a cell that was easier to package.[15] Figure 6 shows a schematic of this packaged cell with its cylindrical Pt electrode.[15]

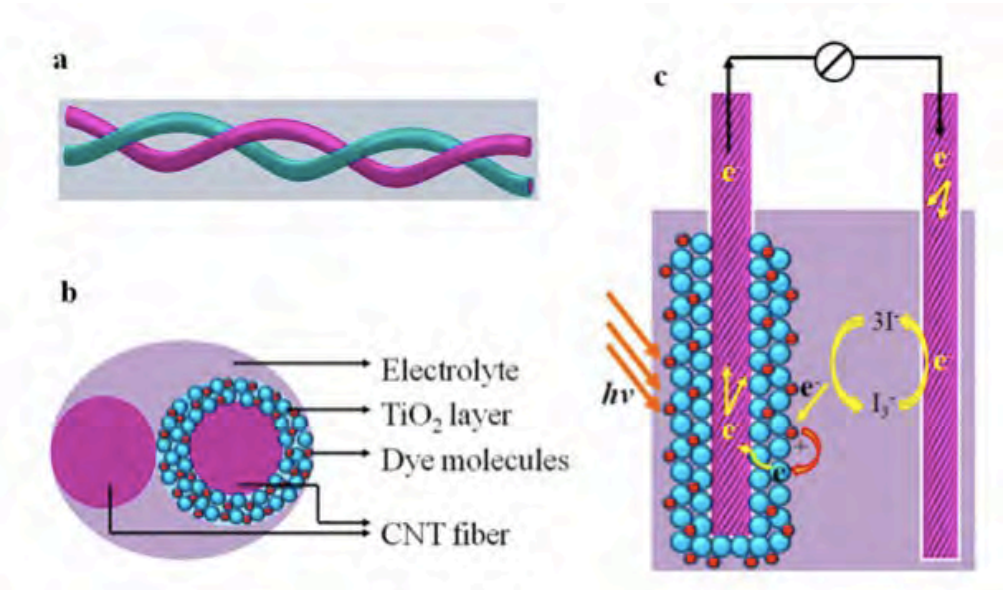

Figure 5. Working mechanism for a fiber solar cell developed by Chen, et al. (a) Twined CNTs create a cell. (b) One CNT is coated in a TiO_2 layer. The TiO_2 nanoparticles are functionalized with dye molecules. (c) The working cell consists of a CNT/TiO_2 working electrode and a bare CNT counter electrode. The fibers are twined together to create the cell, which is immersed in a liquid electrolyte.[12]

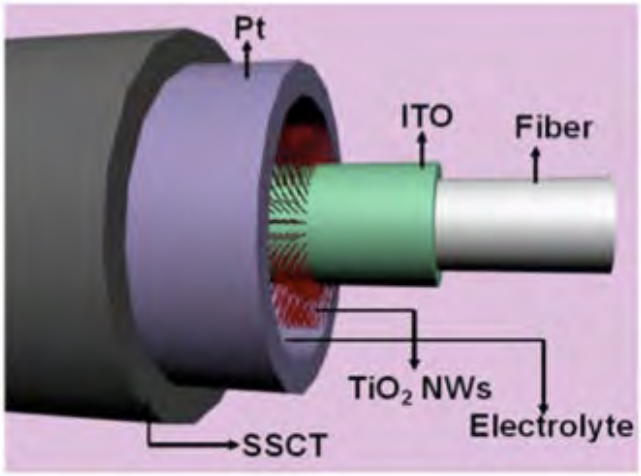

Figure 6. A schematic of the fiber cell by Guo, et al.[15] TiO_2 nanowires are grown off of an optical fiber and Pt is coated on the inside of a stainless steel capillary tube (SSCT). A liquid electrolyte lies between these two layers.

Many FSCs are made using carbon nanotubes (CNTs) for their ideal mechanical strength and high electrical conductivity,[9-12] though some are also made using TiO_2 nanowire arrays.[13-14] For both of these materials, it has been seen that alignment of the nanotubes or nanowires versus a random array is critical for improving efficiency and charge transport, and reducing the number of recombination events.[11] Electrons are not confined to the nanotube or nanowire, and so may cross from one side to the other within a nanotube or may cross from one nanotube to another. This three-dimensional conductivity is what is responsible for the improved efficiency and charge transport.[11] Furthermore, the CNTs themselves are semiconductive, so if the nanowires were highly aligned, there may be no need for TiO_2 nanoparticles. Charge transport and separation would become much faster and more efficient along the nanotubes than along nanoparticles, because of the abundant grain boundaries present in nanoparticles.[11]

1.2.3. Bulk Heterojunction Solar Cells

Bulk heterojunction solar cells (BHJs) are a subset of organic photovoltaics (OPVs). In BHJs, the n-type (electron-conducting) and p-type (hole-conducting) are mixed together into what is called the "active layer" with a random distribution.[15] The BHJ is in contrast to the bilayer solar cell and the ordered heterojunction solar cell (Figure 7). Bilayer solar cells, as the name implies, sandwiches p- and n-type materials around an active chromophore layer. Ordered heterojunction cells are very similar to BHJs, but have an ordered distribution of materials instead of a random one.[15] Bilayer solar cells have low efficiencies because of the small interfacial area between the electron- and hole-conducting materials and the likelihood of recombination at that interface. Ordered heterojunctions are more expensive and difficult to fabricate than BHJs, but both have similar efficiencies.[15] Currently, BHJs have obtained efficiencies of greater than 8%.[15] This efficiency is lower than that for DSSCs because there is a greater chance of recombination of charges due to the increased interfacial area between materials.

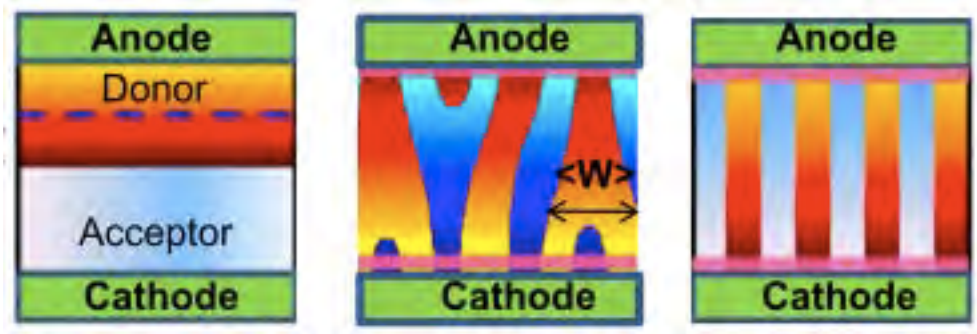

Figure 7. A schematic of three types of OPVs: the bilayer solar cell (left), the BHJ (center), and the "ideal" ordered heterojunction solar cell (right). BHJs are ideal for their ease and cheapness to manufacture and their relatively high efficiencies.[15]

Charge mobility plays a large role in the efficiency of BHJs. Therefore, it is important to understand the morphology of and interface between the materials within the BHJ.[15]

By far the most common BHJ system is regioregular poly(3-hexylthiophene) (P3HT) and a functionalized fullerene, [6,6]-phenyl-C_{61}-butyric acid methyl ester (PCBM). The structures of P3HT and PCBM are shown in Figure 8.[16] P3HT/PCBM systems have reached efficiencies of about 5%.[17]

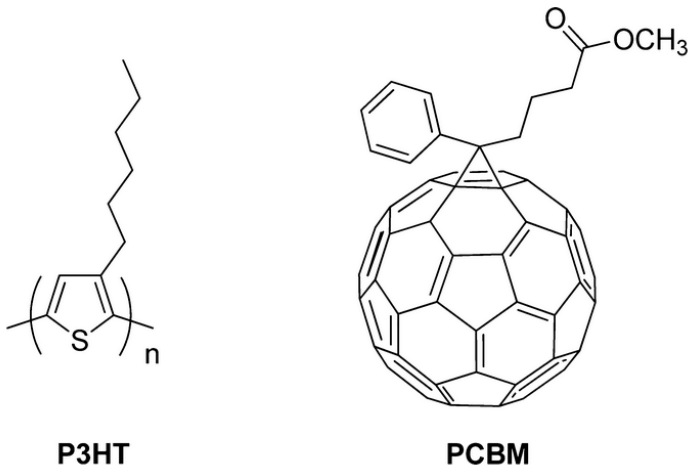

Figure 8. Structures of P3HT and PCBM.[16]

The success of the P3HT/PCBM system relies on the fact that excitons can only separate of distances of about 10 nm, and the polymer and fullerene components can be phase separated on the same length scale. Therefore, theoretically every electron should be able to diffuse from the P3HT region to a fullerene within its lifetime, greatly increasing efficiency by reducing recombination.[17] P3HT is used because of its regioregularity. This increases its hole mobility and extended conjugation.[16] However, the high regioregularity of P3HT increases phase separation when PCBM is also present. This could lower efficiency because of the smaller interfacial area. A lower regioregular P3HT leads to less phase separation, but lower efficiency.[16] The morphology of P3HT/PCBM films can be

controlled by changing various parameters either during or after film formation. Different morphologies may affect the efficiency of the system.[16,18]

1.3. Hybrid Designs

Recently, advances in solar energy have focused on combining techniques and materials from DSSCs, FSCs, and OPVs, as well as incorporating novel materials such as quantum dots (QDs). QDs are semiconductor nanocrystals that have been used as chromophores in solar cells.[19] The most common QD used for chromophores in solar cells is CdSe, but many other dots, such as PbS, PbSe, and CdTe, have also been used. These QDs have been incorporated into many solar cell designs (Figure 9).[19]

QD solar cells currently have efficiencies which are similar to DSSCs and OPVs, with efficiencies around 7% for solid state QD solar cells.[19] One route to achieve hybrid systems is through mechanochemical synthesis.

1.4. Mechanochemical Routes to Nanocomposites

Mechanochemical reactions are solid-solid state reactions that can take place either in a mortar and pestle or in a ball mill; they can also be liquid-assisted or solvent-free. The mechanical energy from the grinding induces chemical reactions and phase transformations.[20]

There are several advantages to mechanochemical reactions: mechanochemical methods have applications in green chemistry, and can themselves be green as there may not be any volatile solvents;[20,21] these methods can also sometimes be faster than the corresponding solvent-based reaction.[21] The grinding can also have many different

effects on the solids, such as heating, local melting, and particle size reduction, which will cause an increase in surface area.[22] Another advantage is that products are easily separated to obtain a pure product.[23]

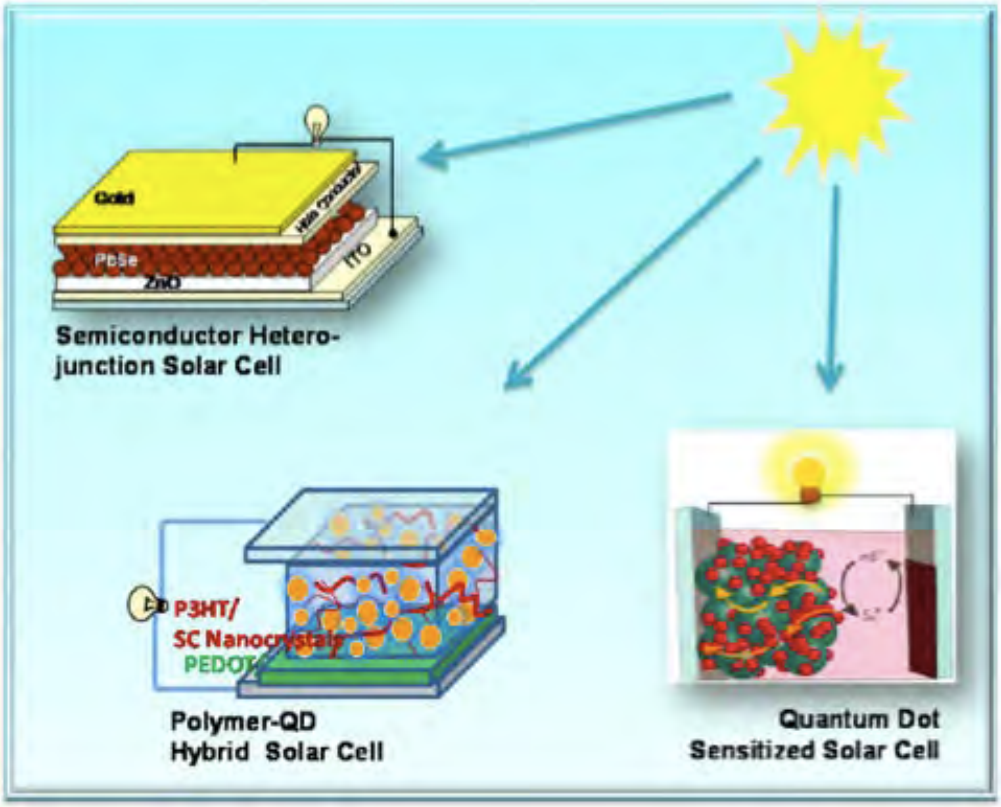

Figure 9. Schematic of three examples of hybrid design solar cells. The first (top left) is a semiconductor heterojunction solar cell, which combines OPV design with two semiconductors: QDs and a metal oxide. The second (bottom left) is a polymer-QD solar cell, which incorporates QDs into a polymeric BHJ. The third (bottom right) is a QD-sensitized solar cell, which combines DSSCs with QDs.[19]

An immediate disadvantage can be seen in the fact that there are few reactions that can be carried out through mechanochemical methods. Another disadvantage is that the mechanical forces experienced during grinding at the molecular level can translate to the formation of cracks and, ultimately, material failure, at the macroscale.[23] Therefore, mechanochemical methods may not be ideal for large-scale reactions.

Mechanochemical reactions have already been very successfully used to synthesise metal-organic frameworks (MOFs)[24,25] and conducting polymers, such as polyaniline and coordination polymers.[21,26] We have employed mechanochemical strategies to explore novel hybrid solar materials in the Hagerman/Kehlbeck/Waterman design.

1.5. The Hagerman/Kehlbeck/Waterman Design

We have created the first example of a bicontinuous network of polyaniline (PANI) and dicyanoaurate-based coordination polymers (CPs) for use in polymer-QD hybrid solar cells. PANI is a widely-studied conductive polymer that can assume several morphlogies. Alan MacDiarmid, 2000 Nobel Laureate in Chemistry and foremost among PANI researchers, once said that, "…there are as many different types of polyaniline as there are people who make it!"[27] PANI is so widespread because of its facile synthesis via many different routes, environmental stability, redox chemistry, and unique acid/based doping/dedoping.[28,29] PANI has three oxidation states: leucoemeraldine, emeraldine, and pernigraniline.[27,28] Leucoemeraldine is the most reduced form, pernigraniline is the most oxidized form, and emeraldine is the conductive form. Figure 10 shows the general structure of PANI, as well as the structures of the three oxidation states of PANI and the conductive emeraldine salt form.

As MacDiarmid hinted, small changes in synthetic parameters can result in large changes to PANI morphology. Figure 11 shows some of the synthetic routes that can lead to various PANI morphologies.[27] This incredible range of morphology is what has lead to PANI being incorporated into many applications, including batteries, sensors, actuators,

antistatic coating, and solar energy.[28] One issue with PANI, however, is that it is water insoluble.[28] For applications that require films, such as solar energy, it is necessary to add a film agent. One such film agent is Laponite, a water-processable clay.

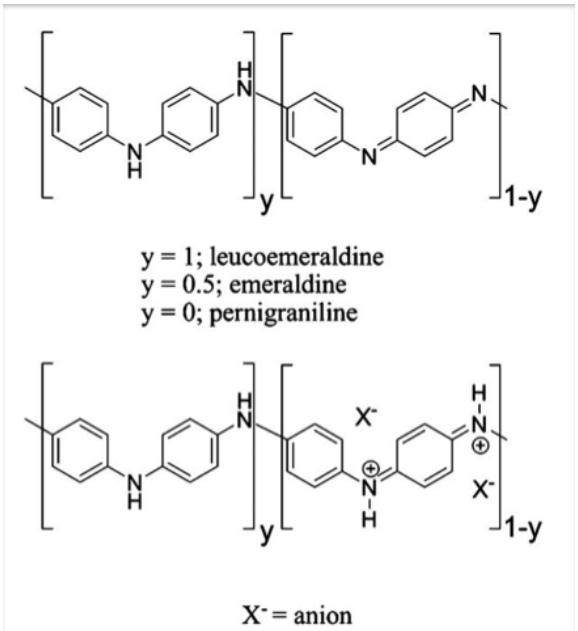

Figure 10. The general structure of the three oxidation states of PANI (top) and the conductive emeralinde salt form of PANI (bottom).[27]

Laponite is an inorganic silicate clay material that can be used to help form electrically-conductive films. Laponite RD is a sodium lithium magnesium silicate clay that is used to form water-processable films. It has the empirical formula $Na_{0.7}^{+}[(Li_{0.3}Mg_{5.5}Si_8)O_{20}(OH)_4]^{-0.7}$, but in this work we use a Cu-exchanged form of Laponite RD.[30] Figure 12 shows an idealized schematic of the structure of Laponite.[30] Laponite forms nanodiscs that are made up of a single tetrahedral-octahedral-tetrahedral layer. Two of these disks stack on top of each other, and since the top and bottom surfaces of the nanodisks are negatively charged, there is an interlayer region between the disks with trapped cations.[30]

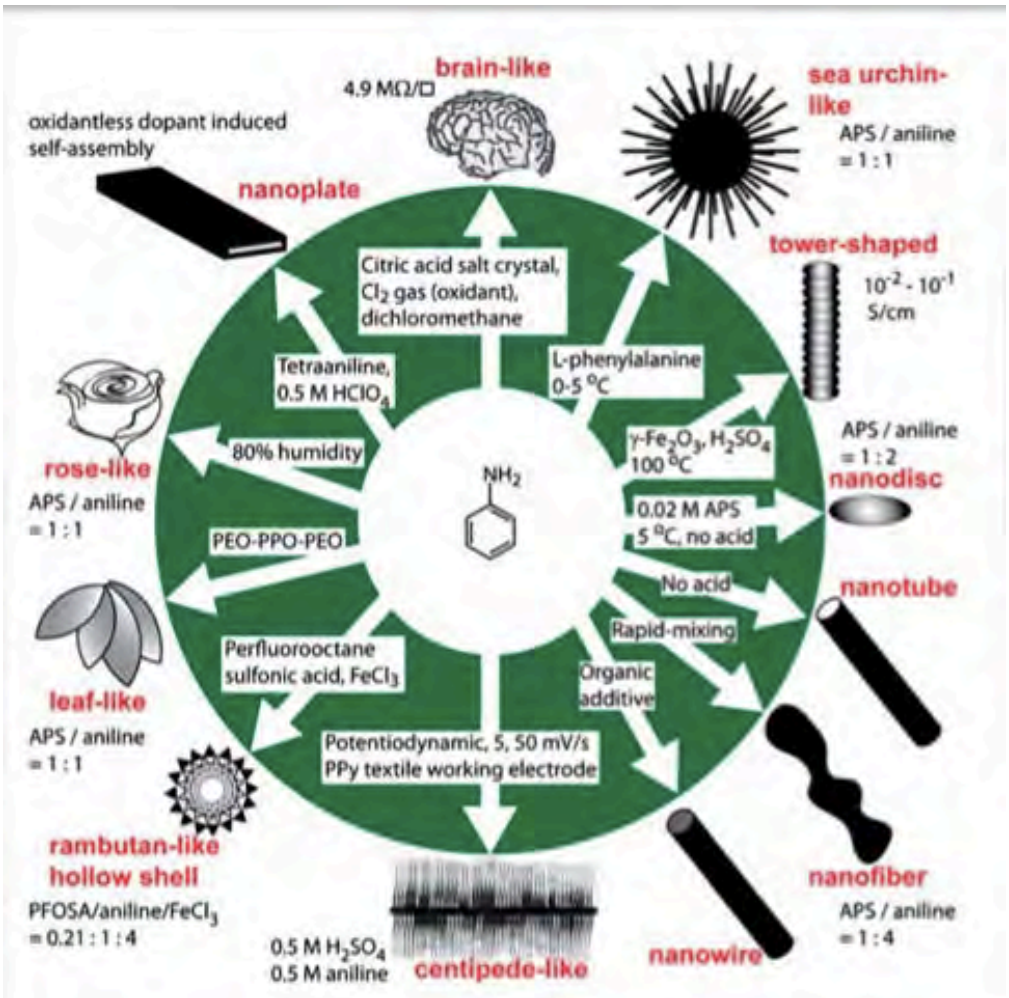

Figure 11. A schematic showing some of the different morphologies PANI can adopt through different synthetic routes.[27]

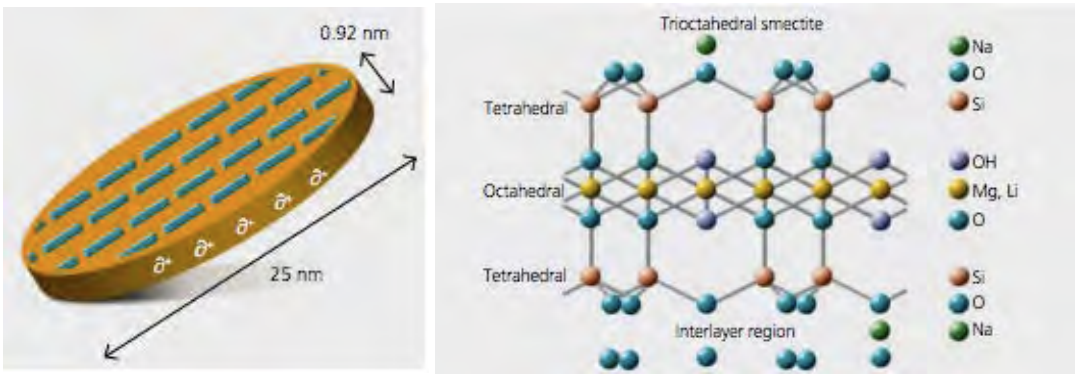

Figure 12. A schematic showing the Laponite nanodisc (left) and the tetrahedral-octahedral-tetrahedral stacking pattern of the discs (right).[30]

Another key component of the bicontinuous polymer network is coordination polymers (CPs). CPs have been shown to have interesting vapochromic properties,[21] but they are also conductive.[31a] One reason for interest in these CPs is the high dimensionality of the material. This is due in part to "aurophillic interactions," or the interactions between d^{10} Au (I) ions.[21,31a] An example of these aurophillic interactions leading to a high-dimensional material is shown in Figure 13.[31a]

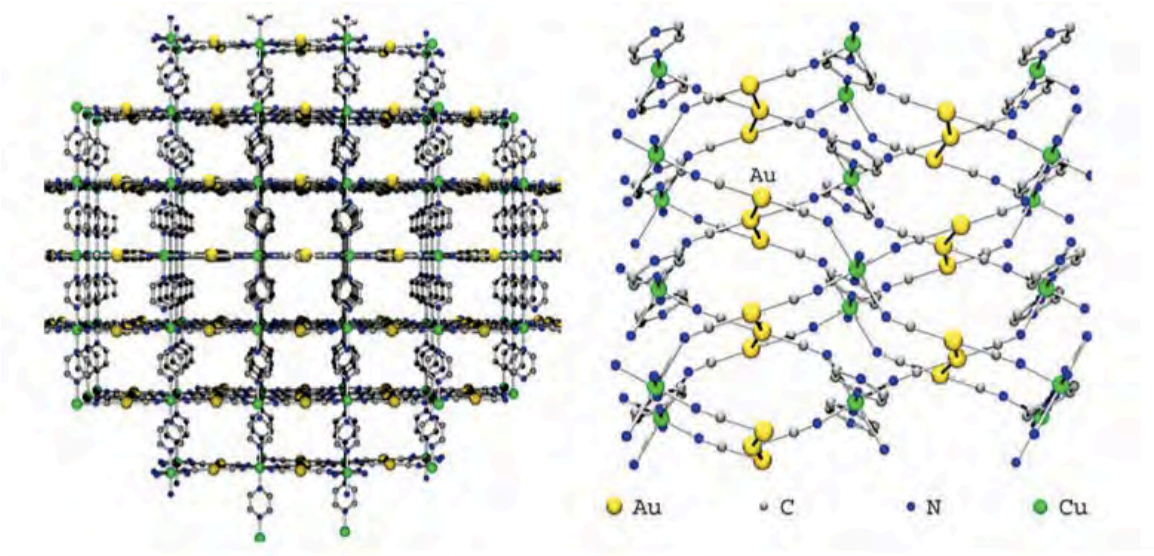

Figure 13. A schematic of the 3D extended framework of Cu(pyrazine)$[Au(CN)_2]_2$ (left) and the aurophillic interactions that support the interpenetrating networks (right).[31a]

These materials have also been explored as sensitizers in third-generation solar cells.[31b] Heterometallic Cu(I)-Ni(II) coordination polymers with halide briding ligands and hexamethylene dithiocarbamate ligands were synthesized. HOMO and LUMO levels were determined using UV-vis-NIR. The HOMO levels were low enough in energy to accept electrons from a redox electrolyte of a DSSC, and the LUMO levels matched with the energy of the conduction band of the TiO_2 semiconductor, thus allowing the coordination polymers to serve as dyes for DSSCs.[31b]

We plan to tether CdSe quantum semiconductor nanocrystals to the Au atoms in the backbone of the dicyanoaurate polymer in our bicontinuous network. This would allow for simple monodispersion of the chromophore, which is important for increasing efficiency. If PEDOT:PSS is also incorporated, the holes may be able to be transported to the cathode. In this way, we could create a “tricontinuous” active layer for a BHJ solar cell with three polymer networks: CP, PANI, and PEDOT:PSS. This active layer would also be templated by Laponite nanodiscs and have monodispersed chromophores. Scanning electron microscopy (SEM), attenuated total reflectance-Fourier transform infrared spectroscopy (ATR-FTIR), ultraviolet-visible spectroscopy (UV-vis), and X-ray diffraction spectroscopy (XRD) were used to study nanoparticle-polymer and polymer-polymer interactions.

2. EXPERIMENTAL

2.1. Materials

Laponite RD was donated by Laporte Industries, UK. All other reagents were purchased from Sigma Aldrich and used without further purification.

2.2. Mechanochemical Routes to Polyaniline

Cu^{2+} Laponite and aniline hydrochloride powders were ground in an agate mortar and pestle at varying weight percents (25:75, 50:50, 75:25, and 85:15 weight percent anilinium hydrochloride: Laponite) for fifteen minutes. The resulting powders were left to age for a period of a few days exposed to the air, then in a sealed vial stored at ambient conditions. The effect of washing the product powders was also examined for a few samples.

An iron (III) chloride/polyaniline powder was synthesised at 80:20 weight percent $FeCl_3 \cdot 6H_2O$:PANI by grinding each powder separately for two minutes, then grinding the two powders together for twenty minutes. The resulting polyaniline was then washed with deionised water using vacuum filtration. A small portion of the wash liquid with dispersed polyaniline was also cast into films on various substrates.

Various morphosynthetic strategies for PANI were investigated. These included: varying the oxidant used to polymerize PANI (Cu^{2+} and Fe^{3+}), varying the reagent ratios, varying the time of grinding of powders, adding a small amount of solvent during grinding, and washing after grinding.

2.3. Mechanochemical Routes to a Heterometallic, Dicyanoaurate-Based Coordination Polymer

A heterometallic, dicyanoaurate-based coordination polymer (CP) was synthesized as reported in Jobággy, et al.[21] $K[Au(CN)_2]$ (100 mg) and $CuCl_2 \cdot 2H_2O$ (30 mg) were ground for 35 min in an agate mortar and pestle. Within a minute of grinding, the powder turned into a light yellow-green color, eventually darkening into a more green color. After grinding, the product was washed with DI water. The obtained dry product was light green in color.

CPs were synthesized with Cu^{2+} Laponite RD instead of $CuCl_2 \cdot 2H_2O$. Lap CP-A was synthesized by grinding $K[Au(CN)_2]$ (100 mg) and Laponite (10 mg) in an agate mortar and pestle for 35 minutes. The color change observed with Lap CP-A was the same as CP. After grinding, the product was washed with DI water. The dry product was light green. Lap CP-B was synthesized by grinding 100 mg $K[Au(CN)_2]$ and 50 mg Laponite in an agate mortar and pestle for 35 minutes. The color change observed with Lap CP-A was the same as Lap CP-A. After grinding, the product was washed with DI water. The dry product was light green.

2.4. Mechanochemical Routes to a Polyaniline-Incorporated Coordination Polymer

A PANI CP was attempted to be synthesized by two different methods. In the first, aniline HCl (100 mg), $K[Au(CN)_2]$ (100 mg), and $CuCl_2 \cdot 2H_2O$ (30 mg) were ground together in an agate mortar and pestle for 35 minutes. However, although this method generated PANI, it did not generate CP. The second method involved first grinding $K[Au(CN)_2]$ (100 mg) and $CuCl_2 \cdot 2H_2O$ (30 mg) for 35 minutes to generate CP

and then adding aniline HCl to the mortar and grinding for an additional 35 minutes. PANI CP was synthesized by grinding CP (25 mg) with anilne HCl (100 mg). Upon grinding, the powder turned light green. The product was washed with DI water. The dry product was light green.

Five different PANI Lap CPs were synthesized. PANI Lap CP-A was synthesized by grinding $K[Au(CN)_2]$ (100 mg) and Cu^{2+} Laponite (50 mg) for 35 minutes. Aniline HCl (100 mg) was added to the mortar and the powders were ground for an additional 35 minutes. The product was washed with DI water. The dry product was light green. PANI Lap CP-B and -C were synthesized by varying the amount of Cu^{2+} Laponite added. PANI Lap CP-B was synthesized by grinding $K[Au(CN)_2]$ (100 mg) and Cu^{2+} Laponite (25 mg) for 35 minutes. Aniline HCl (100 mg) was added to the mortar and the powders were ground for an additional 35 minutes. The product was washed with DI water. The dry product was light green. PANI Lap CP-C was synthesized by grinding $K[Au(CN)_2]$ (100 mg) and Cu^{2+} Laponite (100 mg) for 35 minutes. Aniline HCl (100 mg) was added to the mortar and the powders were ground for an additional 35 minutes. The product was washed with DI water. The dry product was light green. PANI Lap CP-D and -E were synthesized by varying the amount of aniline HCl added. PANI Lap CP-D was synthesized by grinding $K[Au(CN)_2]$ (100 mg) and Cu^{2+} Laponite (50 mg) for 35 minutes. Aniline HCl (50 mg) was added to the mortar and the powders were ground for an additional 35 minutes. The product was washed with DI water. The dry product was light green. PANI Lap CP-E was synthesized by grinding $K[Au(CN)_2]$ (100 mg) and Cu^{2+} Laponite (50 mg) for 35 minutes. Aniline HCl (200 mg) was added to the mortar and the

powders were ground for an additional 35 minutes. The product was washed with DI water. The dry product was light green.

2.5. Casting Films

Films were cast on a variety of substrates, including glass slides, SEM stubs, and ITO/PET. Films were cast on both quarter- and half glass slides. In order to cast a film on a glass slide, the slide was first soaked in deionized water for at least 30 min. The slide was then rinsed generously first with acetone and then with deionized water. Next, the slide was placed in a plastic weigh boat to dry with a second weigh boat on top, offset, as a cover. Once dry, the film was cast on the entirety of the slide and the weigh boat cover was again placed offset as a cover. The films were then left overnight to dry. In order to cast a film on an SEM stub, the stubs were first lightly rinsed with deionized water and then set to dry in a stub holder with a weigh boat covering the stub holder. Once dry, a film was cast directly on the SEM stub at the center and the weigh boat cover was replaced. The films were then left overnight to dry. In order to cast a film on ITO, a piece of ITO was cut from the sheet. The side without the blue plastic backing was placed face-down in a weigh boat. Once the film was ready to be cast, the blue plastic backing was removed and the film was cast on approximately three-quarters of the ITO piece.

PANI Lap CP-A was used to cast films on glass slides. PANI Lap CP-A (50 mg) was dispersed in 10 mL of water in a 15 mL centrifuge tube. The solution was vortexed until it was evenly dispersed. Serial dilutions were prepared by taking 1 mL of the previous solution and diluting back to 10 mL of solution. Four total solutions were prepared and cast on glass slides. The most concentrated solution was also cast on an

SEM stub. The most concentrated film was used for XRD characterization. The second-most concentrated film was used for UV-vis characterization. The two least-concentrated films were too dilute to be used for characterization.

PANI Lap CP-B, -C, -D, and -E were also used to cast films on glass slides. 25 mg of each composite were dispersed in 10 mL water to make a concentrated film. 1 mL of this solution was diluted to 10 mL to make a less-concentrated film. Each of the more-concentrated solutions was also cast on an SEM stub.

Films were also cast from PEDOT:PSS, a hole-conducting polymer. 1:5, 1:10, 1:25, 1:60, and 1:100 dilutions of PEDOT:PSS in DI water were prepared and cast on glass slides. The 1:60 dilution was qualitatively determined to give the best film for BHJs based on its optical transparency and color.

2.6. Constructing Heterojunctions

Six BHJs were cast on ITO. First, 500 μL 1:60 dilution PEDOT:PSS was cast on three-quarters of the ITO slide and left to air dry for one week. Next, 500 μL total volume of an active layer consisting of PANI Lap CP-A, PEDOT:PSS, and Rubipy (1×10^{-5} M) was cast on top of the PEDOT:PSS layer. The second-most concentrated film solution of PANI Lap CP-A was used. Table 1 gives the ratios of the active layer components for each BHJ.

2.7. Characterization

Samples were characterized by a variety of methods, including scanning electron microscopy, attenuated total reflectance-Fourier transform infrared spectroscopy,

ultraviolet-visible absorption spectroscopy, and X-ray diffraction spectroscopy. These methods were used in order to: study nanoparticle-polymer and polymer-polymer interactions; study structure-property relationships; and verify the successful synthesis of composites.

Scanning electron microscopy (SEM) was used to investigate the surface morphology of samples. Various parameters were optimized to image each sample. The accelerating voltage (EHT) was tuned between 3 and 15 keV. A lower EHT reduced charging and allowed for more surface-level morphology to be seen. A higher EHT gave rise to higher-quality images. Spot size was also changed on a case-by-case basis. Lowering the spot size helped with charging, but also darkened the image.

Both powders and films were imaged using a Zeiss Evo 50 SEM. In order to image powders, conducting carbon tape was placed on an SEM stub. A transmission electron microscopy (TEM) grid was then placed on the carbon tape. Finally, a small amount of powder was sprinkled onto the SEM stub, with care that the TEM grid was covered. The SEM stub was then gently tapped to remove any loose, excess powder. In order to image films, a film was cast directly on an SEM stub.

Attenuated total reflectance-Fourier transform infrared spectroscopy (ATR-FTIR) was used to investigate samples. All spectra were collected at 2 cm^{-1} resolution with 128 scans on a Nicolet Avatar 330 FTIR with a SmartOrbit ATR attachment.

Ultraviolet-visible absorption spectroscopy (UV-vis) was used to determine where composite films absorbed across the ultraviolet and visible regions of light. An Agilent 8453 spectrophotometer was used. Films were held in front of the sample holder, in the

path of the light, while a spectrum was collected. Several spectra can be collected from the same film by placing different areas of the film in front of the path of the light.

X-ray diffraction spectroscopy (XRD) was performed on a Philips PW 1840 X-ray diffractometer with a PW 1729 X-ray generator in order to determine the crystallinity of samples. Half-glass-slide films were cast and placed on an aluminum sample holder. Spectra were run for 12.5 h at 0.6° per minute between 5 and 50° 2θ with Co Kα radiation, λ = 1.79 Å.

Table 1. Active layer components for six BHJs.

BHJ	PANI Lap CP-A (µL)	PEDOT:PSS (µL)	Rubipy (µL)	DI H_2O (µL)
1	125	125	125	125
2	125	125	250	--
3	125	250	125	--
4	250	125	125	--
5	125	125	50	200
6	225	225	50	--

3. Results and Discussion

3.1. Structure and Morphology of Reagents

It is important and interesting to note that the morphologies of all four reagent powders (aniline HCl, Cu^{2+} Laponite RD, $K[Au(CN)_2]$, and $CuCl_2 \cdot 2H_2O$) are distinct, and their morphology may or may not be conserved in the composites.

Aniline HCl salt was examined by ATR-FTIR spectroscopy and SEM. The ATR-FTIR spectrum is shown in Figure 14. Major peaks can be seen at 2800 cm^{-1}, 1600 cm^{-1}, 1490 cm^{-1}, and 1025 cm^{-1}, which are attributed to C-H alkyl stretching, N-H bending, C-C aromatic ring stretching, and C-N stretching, respectively.

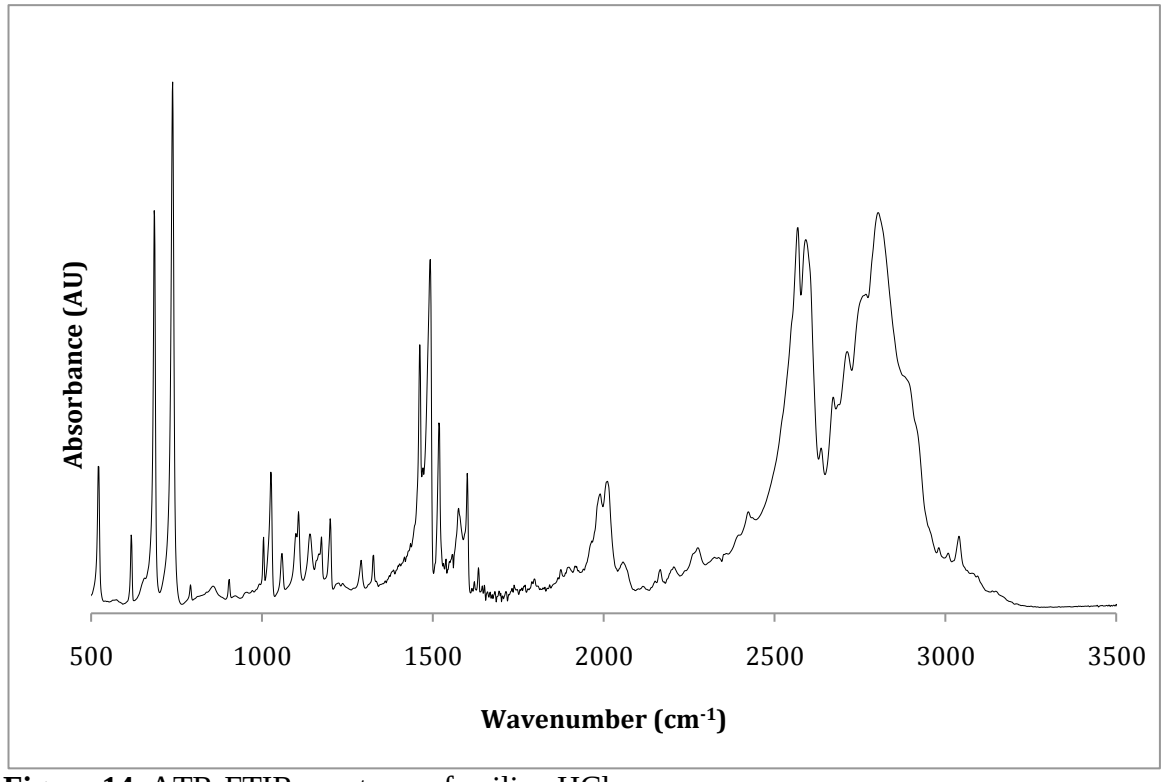

Figure 14. ATR-FTIR spectrum of aniline HCl.

SEM images of aniline HCl are shown in Figures 15-16. The aniline HCl crystals are approximately 200 μm in diameter and fairly flat, with some small flake-like

morphology visible at the surface of the crystals. Figure 16 reveals that the flake-like morphology can resemble lamellar stacking as well.

Anhydrous Cu^{2+}-exchanged Laponite RD powder was also examined by ATR-FTIR spectroscopy and SEM. The ATR-FTIR spectrum is shown in Figure 17. Major peaks can be seen at 3100 cm^{-1}, 1050 cm^{-1}, and 850 cm^{-1}, which are attributed to O-H stretching, a combination of internal and surface Si-O stretching, and edge Si-O stretching.

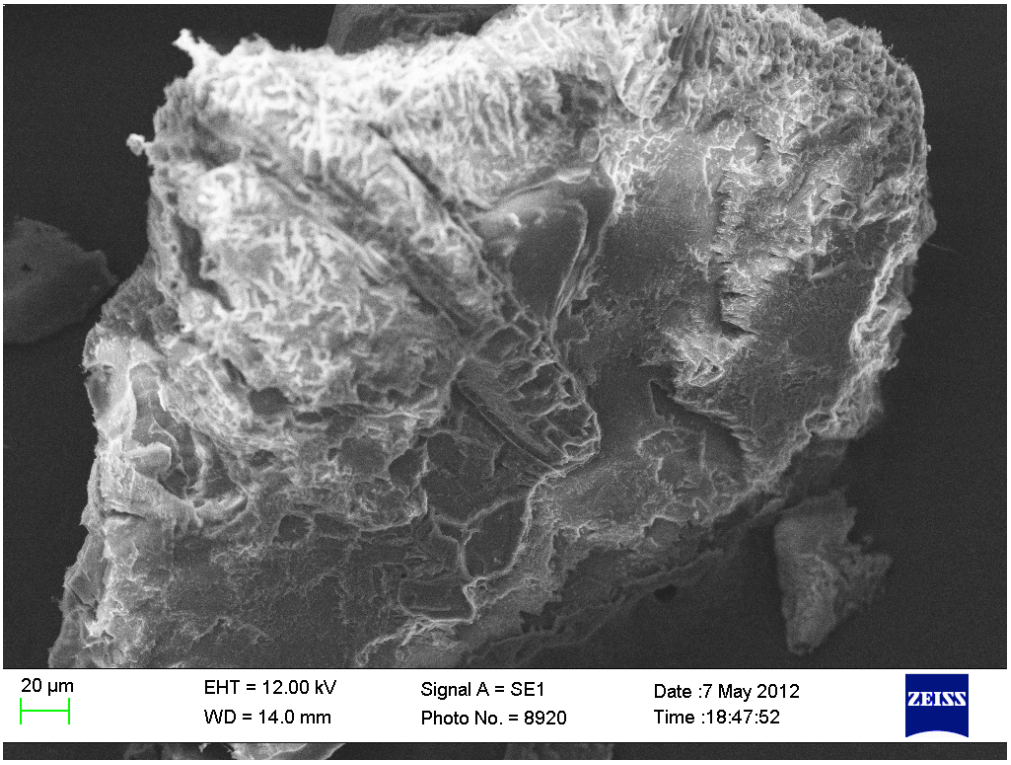

Figure 15. A SEM image of a salt crystal of aniline HCl (scale bar = 20 µm). The crystal is large and fairly flat, with some small flake-like morphology at the surface.

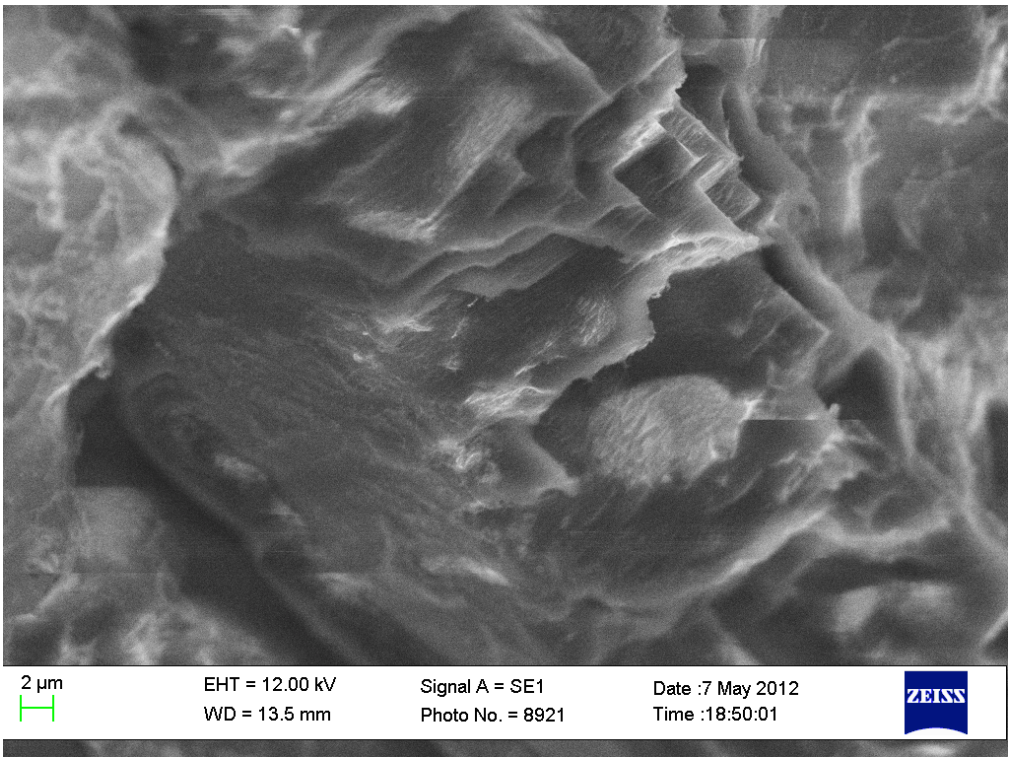

Figure 16. A SEM image of a close-up of the aniline HCl crystal in Figure 15 (scale bar = 2 µm). Lamellar stacking morphology can be seen.

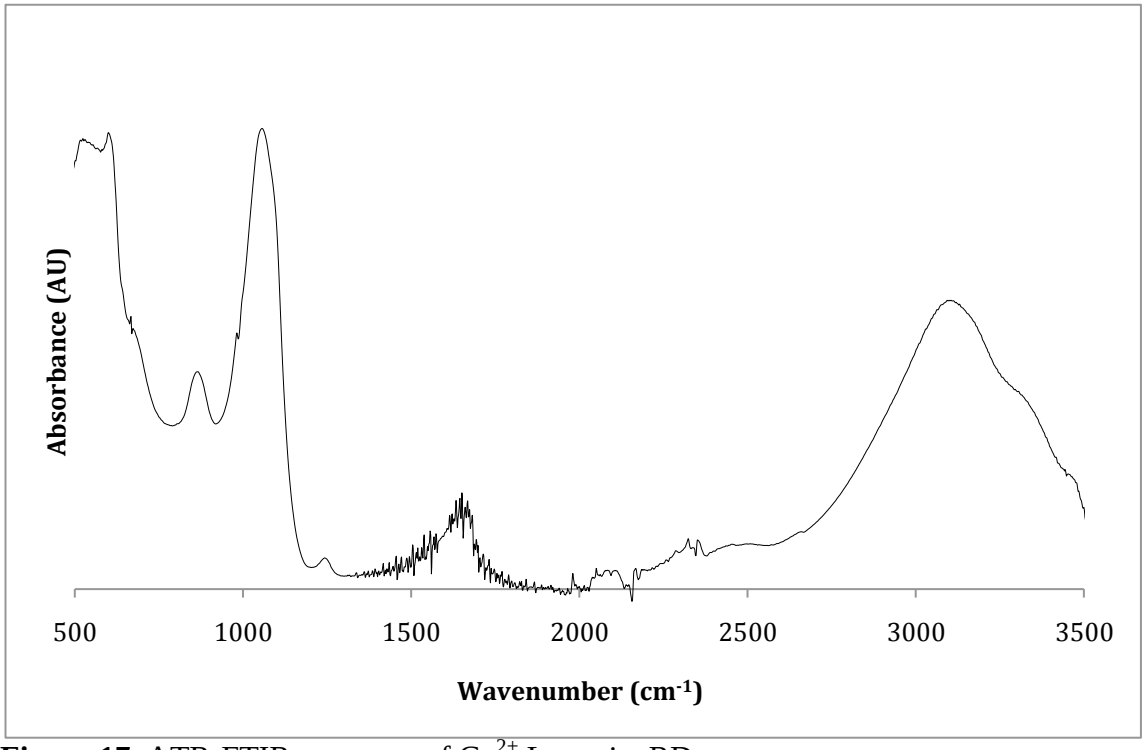

Figure 17. ATR-FTIR spectrum of Cu^{2+} Laponite RD.

SEM images of Cu^{2+} Laponite are shown in Figures 18-19. Under the SEM, The Cu^{2+} Laponite RD powder appears to be agglomerated platelets. The platelets, approximately 2-3 μm in diameter, may be made up of Laponite disks.

$K[Au(CN)_2]$ powder was examined by ATR-FTIR spectroscopy and SEM. The ATR-FTIR spectrum is shown in Figure 20. The major peak at 2140 cm^{-1} is attributed to C≡N stretching. The other peaks are likely from water.

SEM images of $K[Au(CN)_2]_2$ are shown in Figures 21-22. At first glance, $K[Au(CN)_2]$ morphology somewhat resembles that of aniline HCl, but $K[Au(CN)_2]$ crystals are much smaller, at a diameter of about 30 μm, and flatter, with less flake-like morphology. Instead, there are stacking faults on the sides, as can be seen in Figure 22.

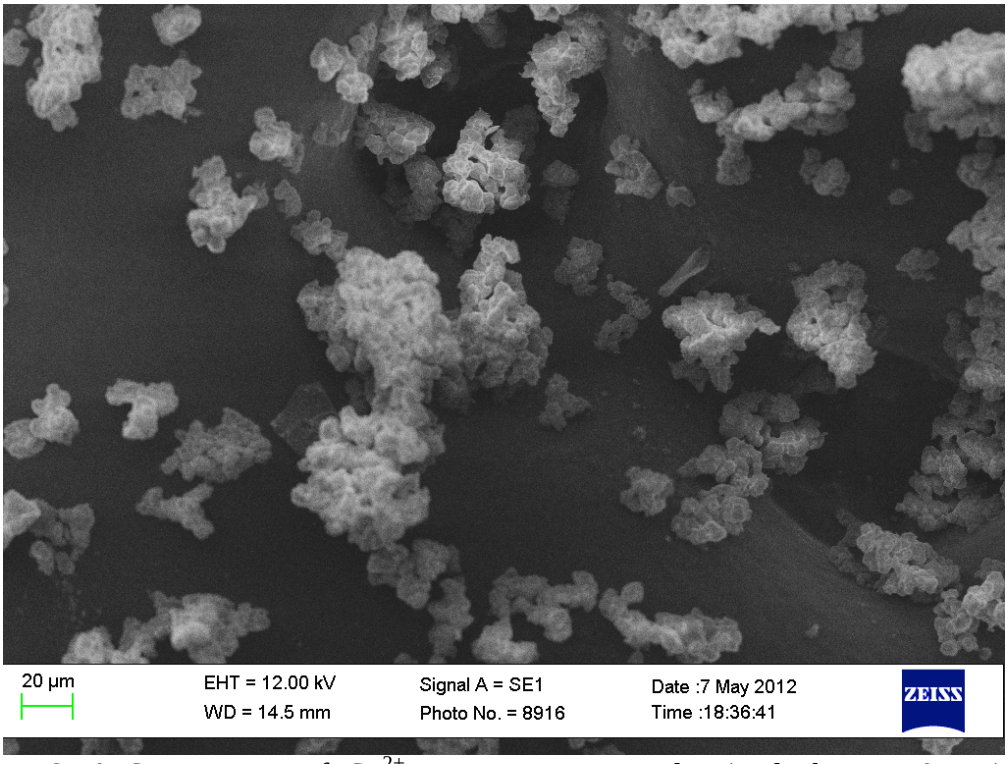

Figure 18. A SEM image of Cu^{2+} Laponite RD powder (scale bar = 20 μm). The morphology resembles agglomerated platelets.

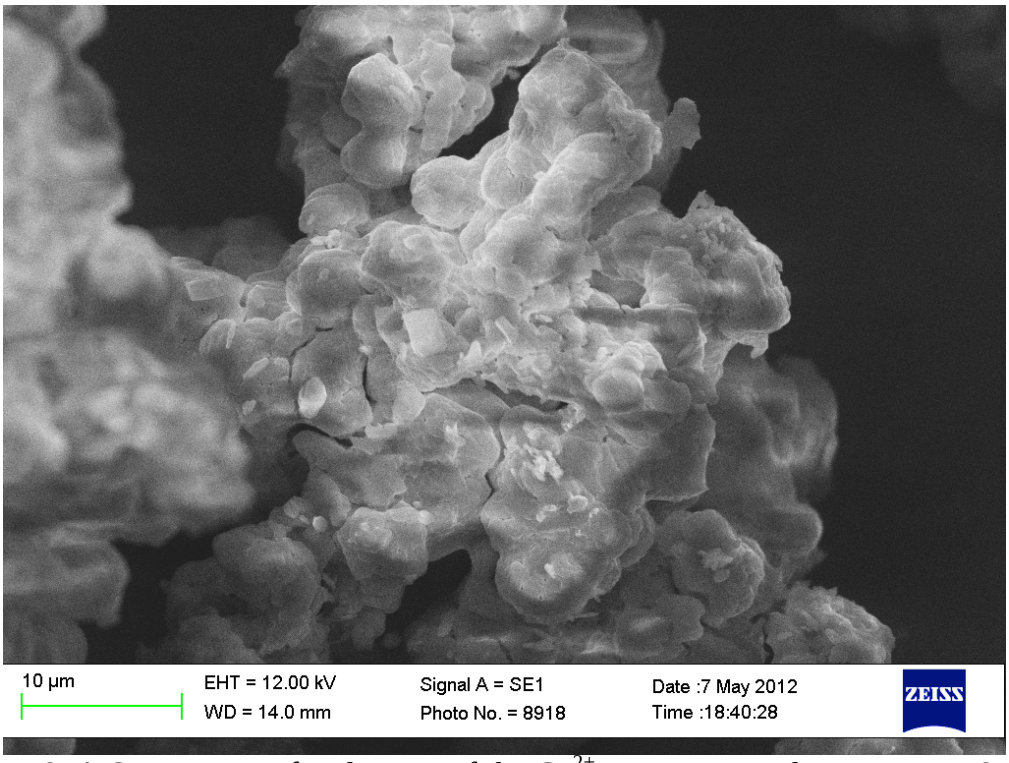

Figure 19. A SEM image of a close-up of the Cu^{2+} Laponite powder in Figure 18 (scale bar = 10 µm). The platelets appear to be approximately 2-3 µm in diameter.

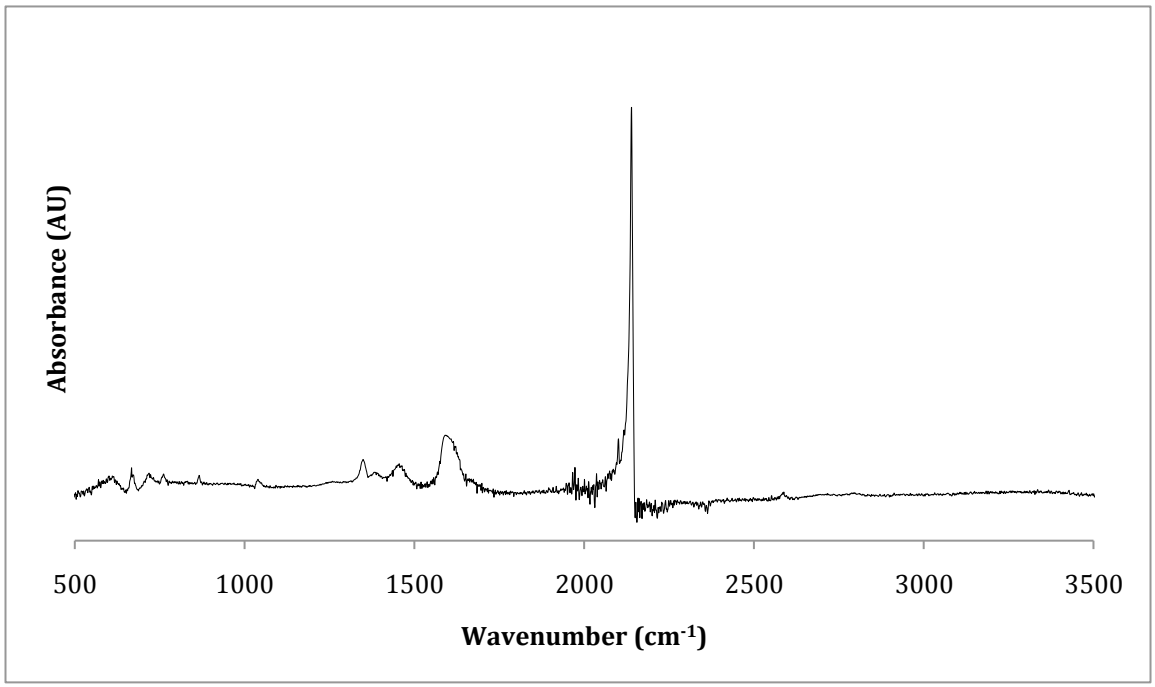

Figure 20. ATR-FTIR spectrum of $K[Au(CN)_2]$.

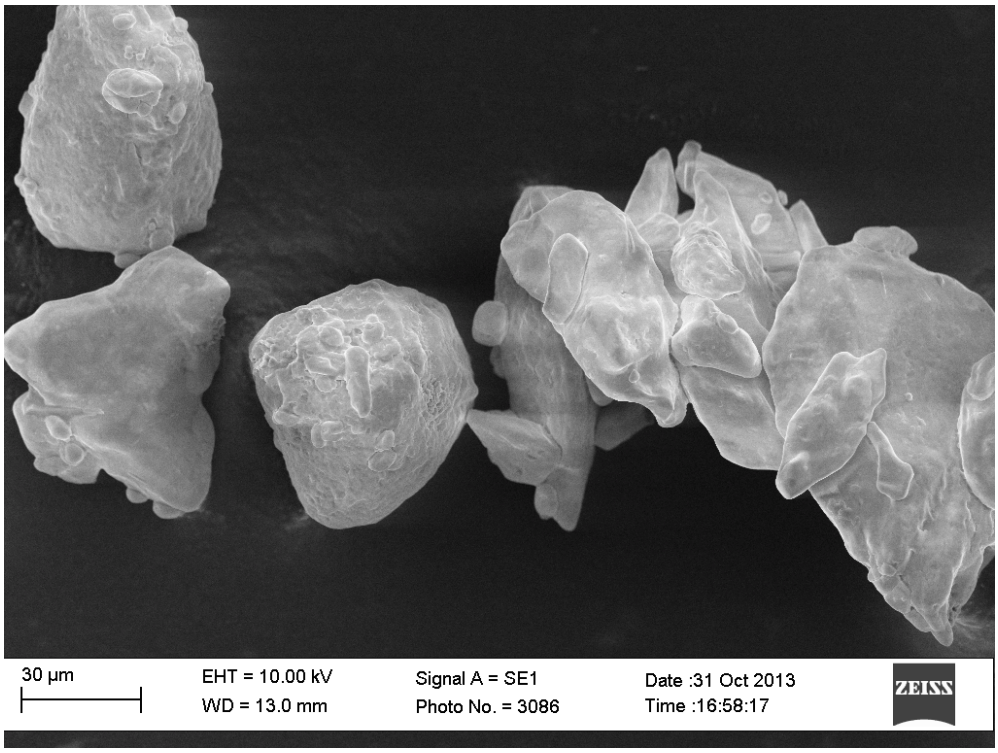

Figure 21. A SEM image of $K[Au(CN)_2]$ powder (scale bar = 30 µm). Crystals are relatively large and quite smooth.

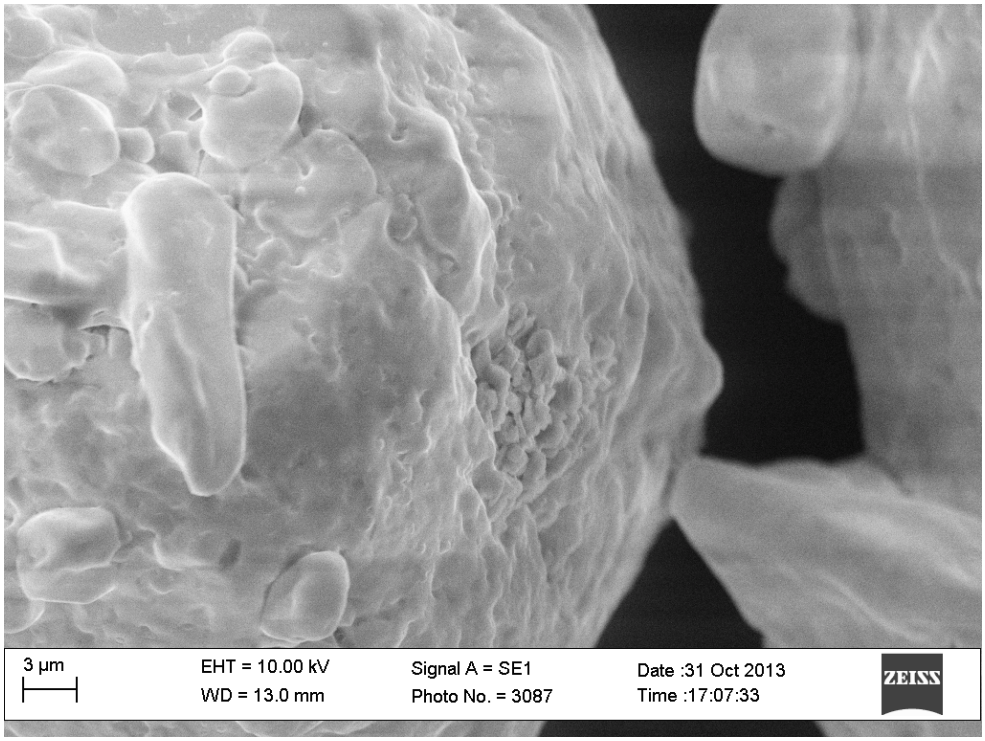

Figure 22. A SEM image of a close-up of Figure 21 (scale bar = 3 µm). Dimpling can be seen on the sides of the $K[Au(CN)_2]$ crystal.

$CuCl_2 \cdot 2H_2O$ powder was examined by ATR-FTIR spectroscopy and SEM. The ATR-FTIR spectrum is shown in Figure 23. Major peaks can be seen at 3315 cm^{-1} and 3155 cm^{-1}, which are attributed to two O-H stretches. Other peaks are also from hydrate water.

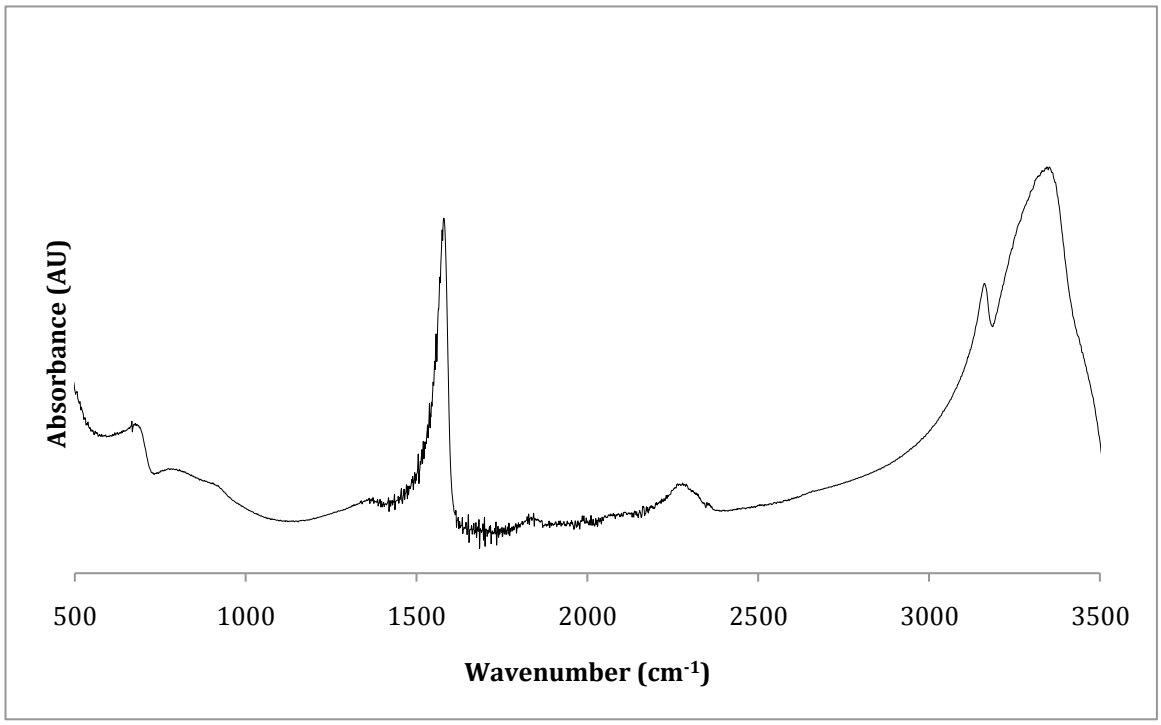

Figure 23. ATR-FTIR spectrum of $CuCl_2 \cdot 2H_2O$.

SEM images of $CuCl_2 \cdot 2H_2O$ are shown in Figures 24-25. $CuCl_2 \cdot 2H_2O$ powder morphology resembles large, rod- or rectangular-prism-like structures, which vary vastly in their dimensions. The surfaces of the structures are very smooth and show little surface morphology.

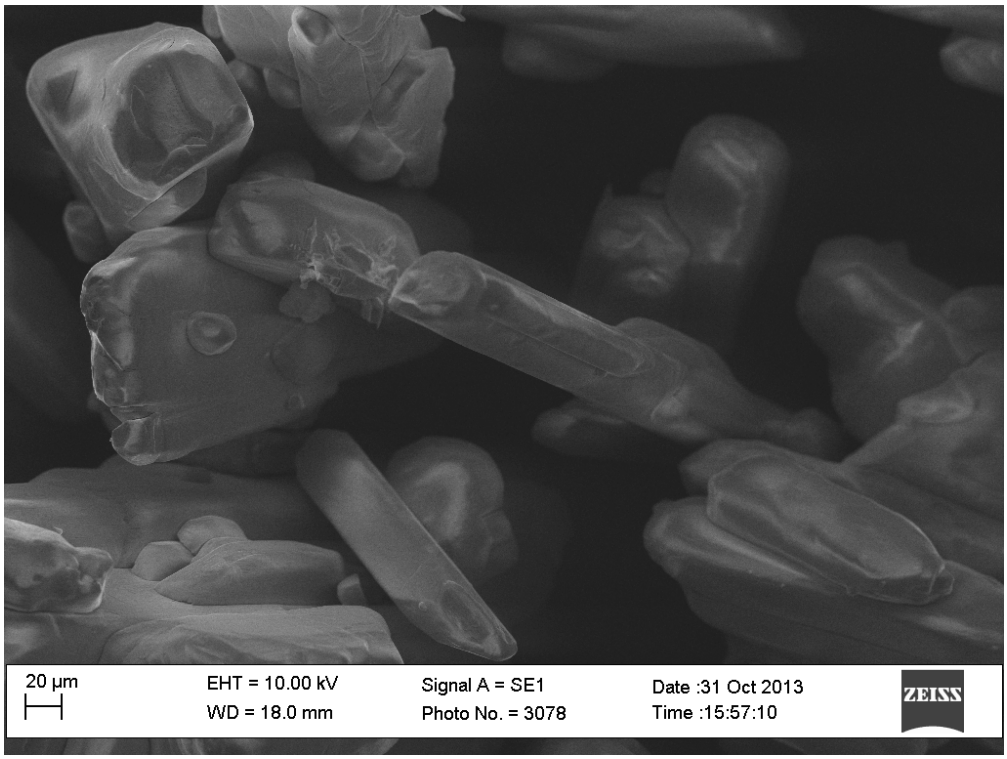

Figure 24. A SEM image of $CuCl_2 \cdot 2H_2O$ powder (scale bar = 20 µm). There are varying sizes of rod- and rectangular-prism-shaped structures.

Figure 25. A SEM image of a close-up of Figure 24 (scale bar = 10 µm). The structures are very smooth, with little surface morphology.

3.2. Structure and Morphology of Composites

Jobággy, et al. reported mechanochemical syntheses of various heterometallic dicyanoaurate-based coordination polymers (CPs).[21] One of particular interest to the Hagerman group was the CP produced from the grinding of $K[Au(CN)_2]$ and $CuCl_2 \cdot 2H_2O$ powders. The resultant CP had Au and Cu metals in the backbone of the polymer with CN bridging ligands.[21] This CP was first reproduced as reported and then a new CP (Lap CP) was synthesized using Cu^{2+} Laponite instead of $CuCl_2 \cdot 2H_2O$. CP was examined by ATR-FTIR spectroscopy and SEM. The ATR-FTIR spectrum is shown in Figure 26. Major peaks can be seen at 2215 cm^{-1} and 2170 cm^{-1}, attributed to C≡N stretching. The two different peaks indicate that there are two different C≡N coordination environments as a result of the cyano ligand being bound to two different metals.[21]

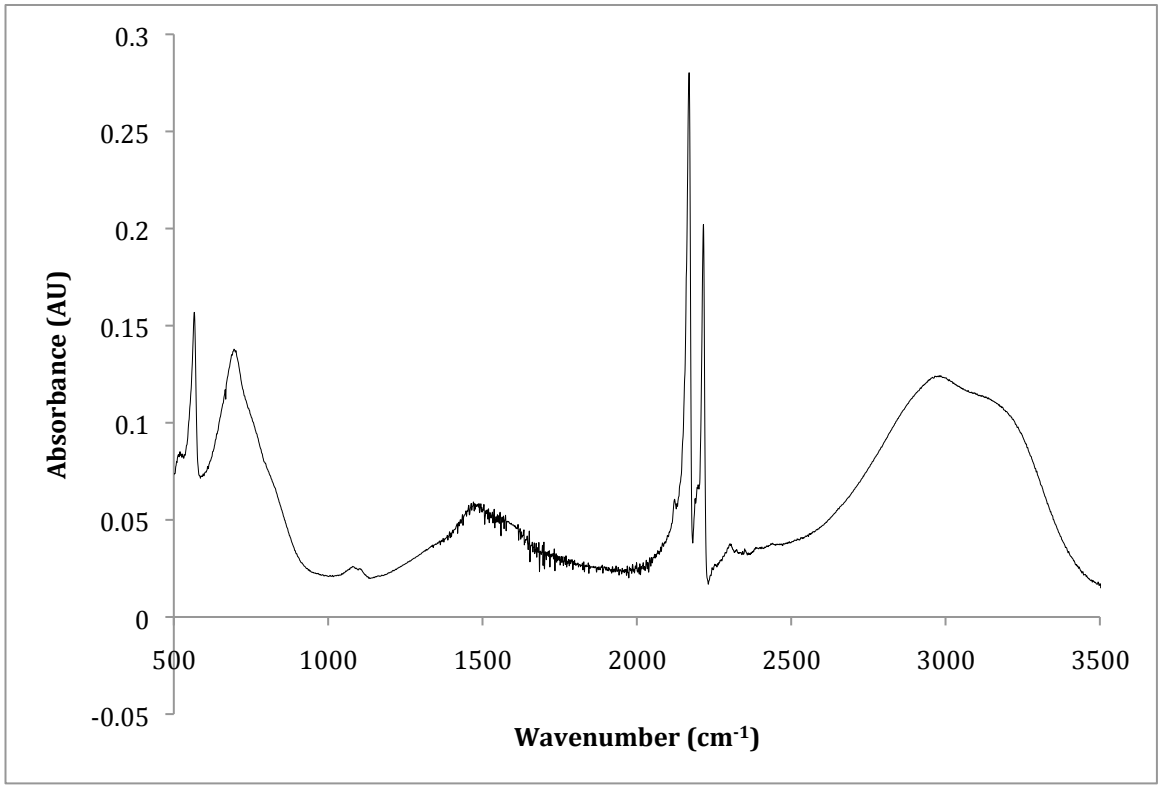

Figure 26. ATR-FTIR spectrum of CP.

SEM images are shown in Figures 27-28. The alphanumeric grid seen in Figure 27 is a transmission electron microscopy (TEM) grid. The TEM grid allows for aging studies, as the same spot can be returned to after a period of time to see if any differences can be noted. CP morphology looks different than any of the control morphologies, resembling crystals of varying sizes, small to large, with a polymeric overgrowth.

Lap CPs were synthesized at two different mass ratios of Laponite: Lap CP-A was synthesized at 10:1 g $K[Au(CN)_2]$:Cu^{2+} Laponite and Lap CP-B was synthesized at 2:1 g $K[Au(CN)_2]$:Cu^{2+} Laponite. Both Lap CP powders were investigated using ATR-FTIR spectroscopy and SEM. The ATR-FTIR spectrum of Lap CP-A is shown in Figure 29. Major peaks can be seen at 2215 cm^{-1}, 2170 cm^{-1}, and 1060 cm^{-1}. The first two peaks are attributed C≡N stretching and the third peak is attributed to Si-O stretching. The ATR-FTIR spectrum of Lap CP-B is shown in Figure 30. Major peaks can be seen at 2215 cm^{-1}, 2170 cm^{-1}, and 1080 cm^{-1}. Again, the first two peaks are attributed to C≡N stretching and the last is attributed to Si-O stretching. In both spectra, it appears that the surface and internal Si-O stretches are both in the broad Si-O peak, while the edge Si-O stretch is likely buried in the broad peak at 680 cm^{-1}.

SEM images of Lap CP-A are shown in Figures 31-32. The powder has crystals of about 20 μm in diameter coated in polymer overgrowth, similar to CP. However, the polymeric overgrowth observed in Lap CP-A has more wire-like structures than in CP. This indicates that the Laponite is templating the polymer in a different way than the $CuCl_2 \cdot 2H_2O$.

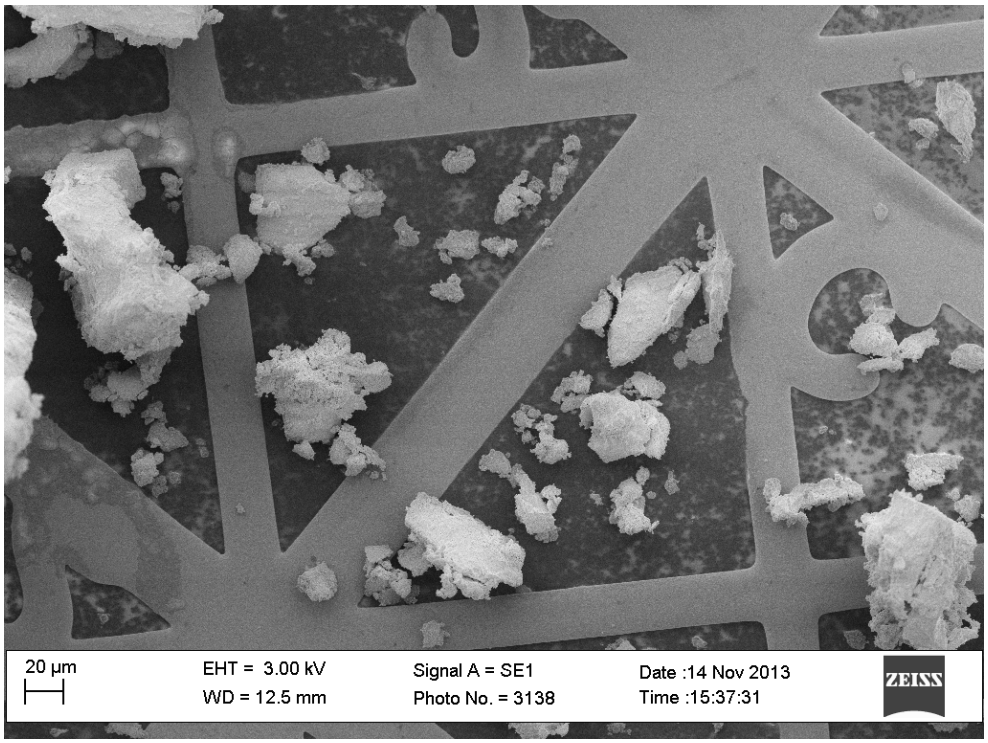

Figure 27. A SEM image of CP powder (scale bar = 20 µm). As can be seen, the crystals vary quite wildly in size. The alphanumeric grid seen in the background is a TEM grid.

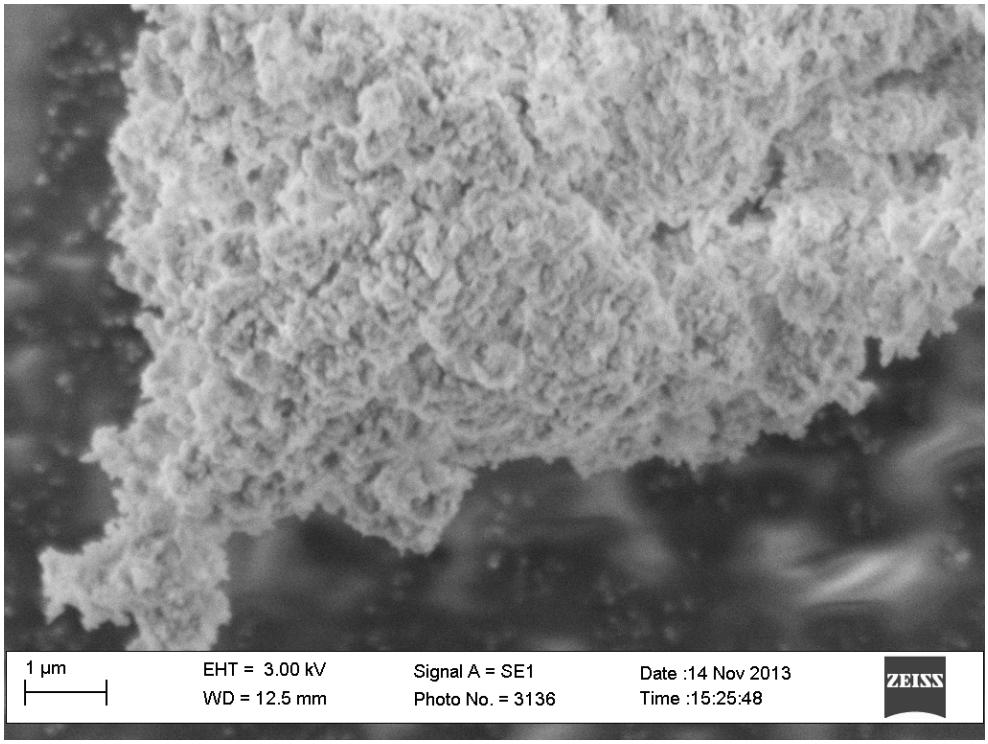

Figure 28. A SEM image of a close-up of a CP crystal (scale bar = 1 µm). Polymeric overgrowth coats the entire crystal.

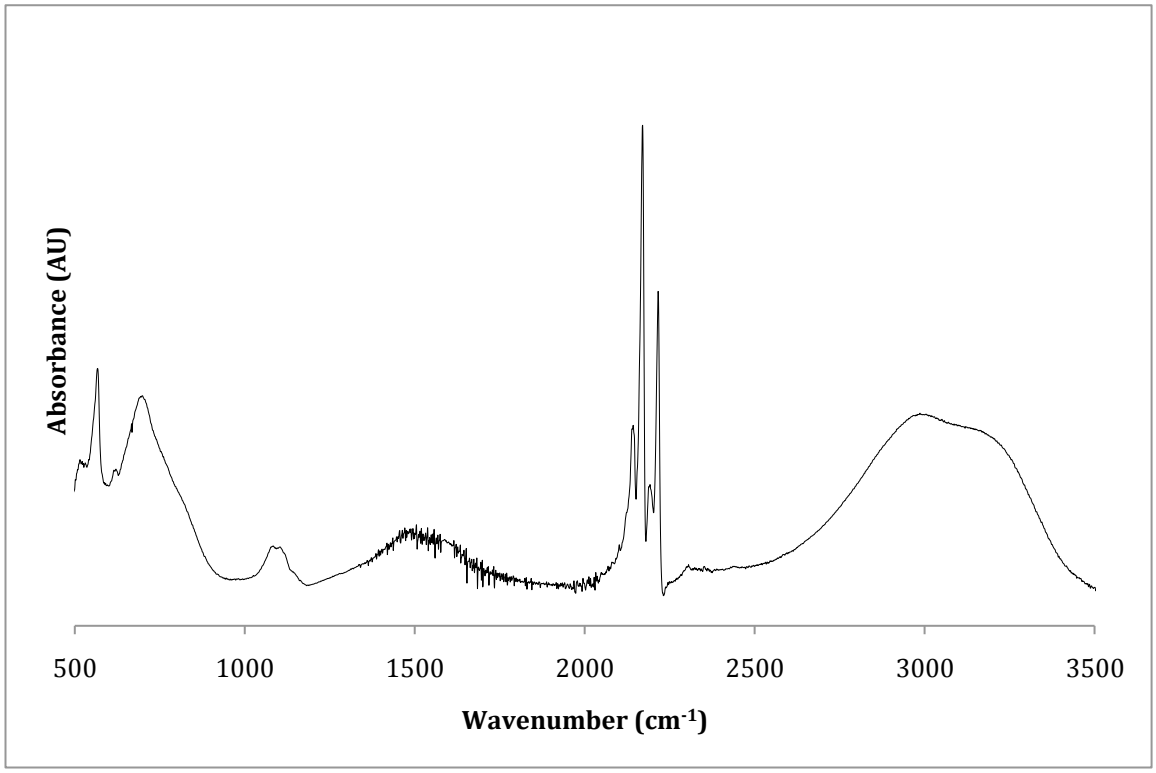

Figure 29. ATR-FTIR spectrum of Lap CP-A

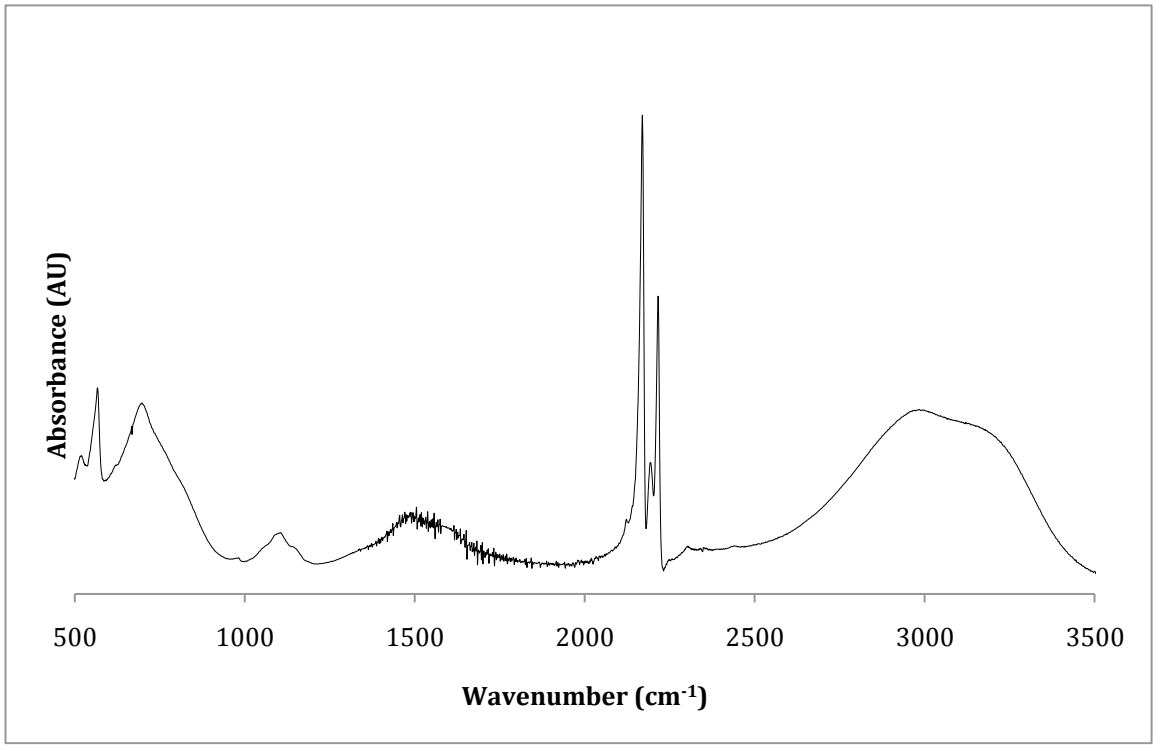

Figure 30. ATR-FTIR of Lap CP-B

SEM images of Lap CP-B are shown in Figures 33-34. The morphology of Lap CP 2 is more porous than Lap CP-A or CP. In addition, the polymeric overgrowth observed in Lap CP-B has more wire-like structure. This indicates that the addition of Laponite to the CP increases the porosity of the Lap CP and creates a more wire-like polymeric overgrowth with increasing amount of Laponite. Similar morphology has been observed with Cu-based coordination polymers.[31c] Thus, it is likely that the Cu from Laponite is templating this morphology, especially as it becomes more apparent as more Laponite is added. The porosity of the structure will likely be beneficial to the design of the heterojunction, as the porous structure will allow for a greater interface between materials and more efficient electron-hole transport. If a liquid electrolyte were to be used, as in the Grätzel cell, the porous structure would allow for penetration of the electrolyte throughout the material, again increasing the interfacial area between materials and increasing efficiency.

The CP-templated polymerization of PANI was attempted in two different processes: the two-step synthesis and the one-step synthesis (PANI CP-A and -B, respectively). Both PANI CP powders were investigated using ATR-FTIR spectroscopy and SEM. The ATR-FTIR spectrum of PANI CP-A is shown in Figure 35. Major peaks can be seen at 2800 cm^{-1}, 2215 cm^{-1}, 2170 cm^{-1}, 1600 cm^{-1}, 1570 cm^{-1}, and 1460 cm^{-1}. These are attributed to C-H stretching, two C≡N stretches, C-C aromatic ring stretching, quinoid breathing modes, and benzene breathing modes, respectively.

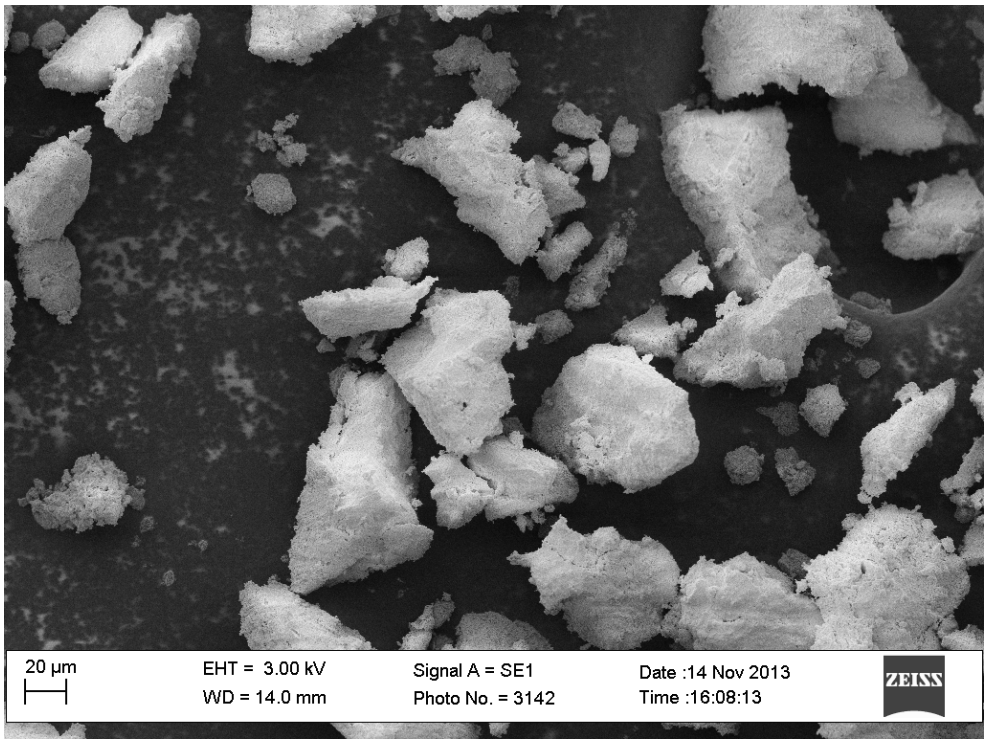

Figure 31. A SEM image of Lap CP-A powder (scale bar = 20 µm). Crystals are about 20 µm in diameter with some polymer overgrowth.

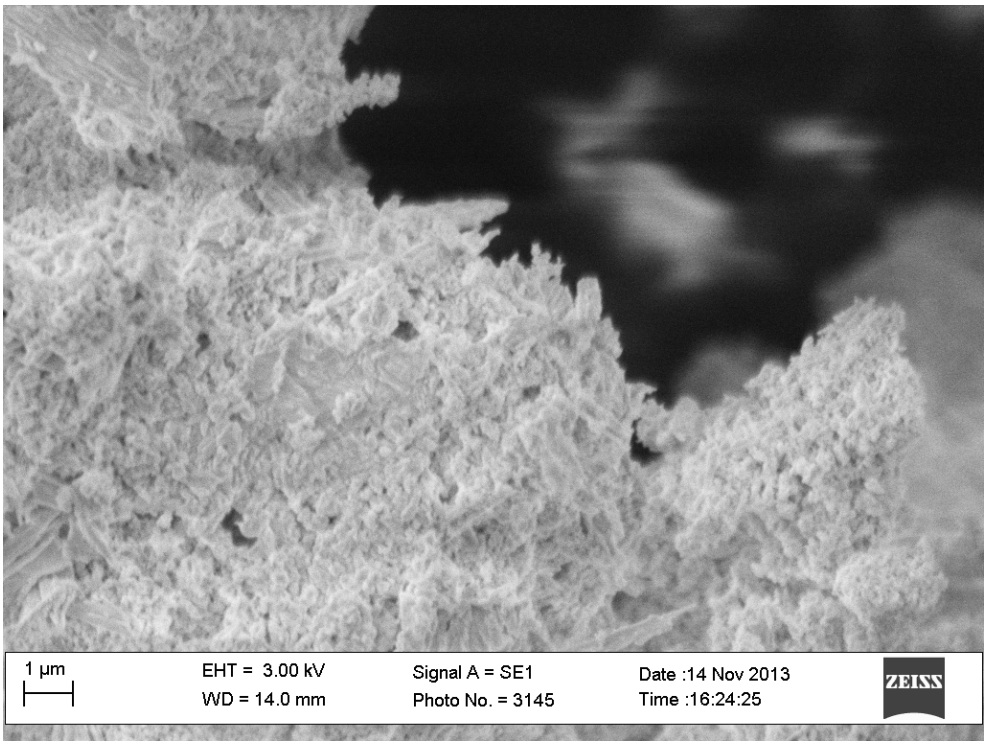

Figure 32. A SEM image of a close-up of a Lap CP-A crystal (scale bar = 1 µm). Polymer overgrowth shows more wire-like structure than in CP.

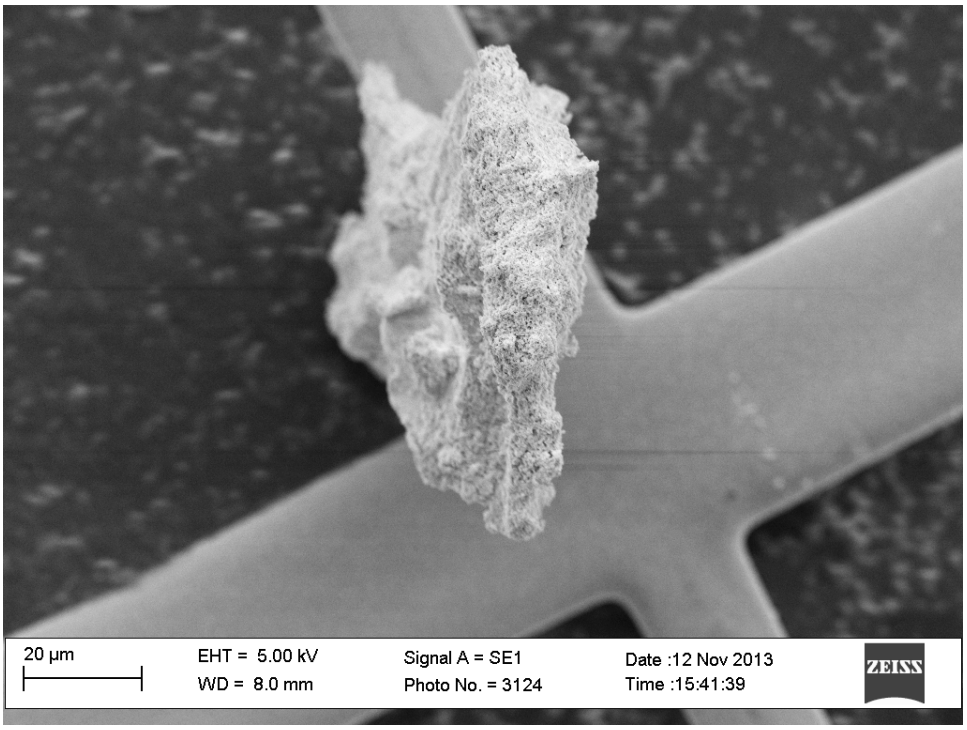

Figure 33. A SEM image of Lap CP-B powder caught upright (scale bar = 20 µm). The structure is much more porous than either Lap CP-A or CP.

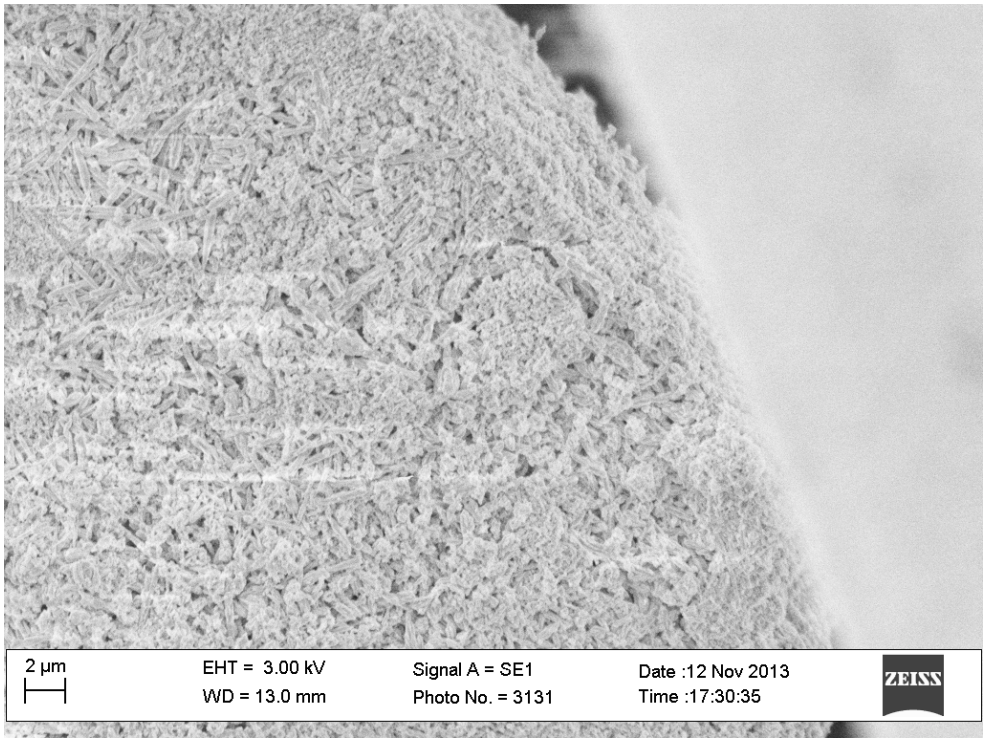

Figure 34. A SEM image of a close-up of Lap CP-B (scale bar = 2 µm). Even more wire-like growth is observed in Lap CP-B than was observed in Lap CP-A. The structure is more porous in Lap CP-B as well.

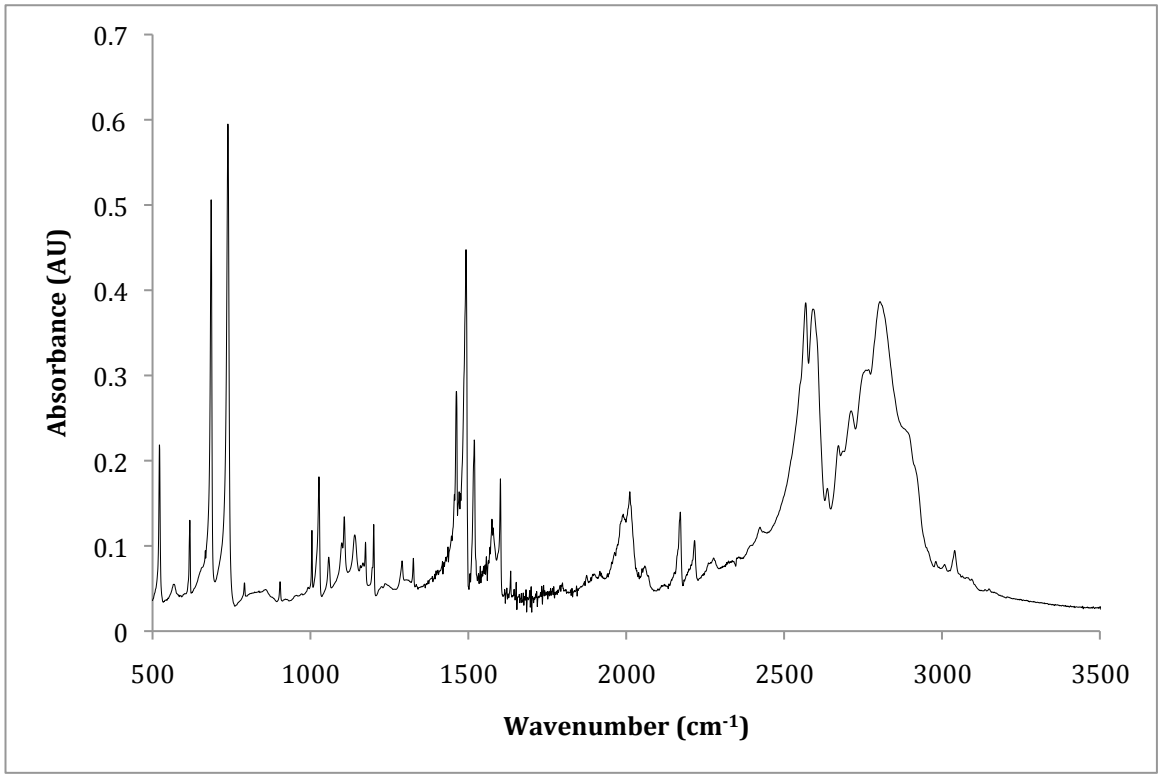

Figure 35. ATR-FTIR spectrum of PANI CP-A.

The ATR-FTIR spectrum of PANI CP-B is shown in Figure 36. Major peaks can be seen at 2215 cm^{-1} and 2170 cm^{-1}, which are both attributed to C≡N stretching. There are no visible peaks attributed to PANI for PANI CP-B. Therefore, it was determined that a one-step synthesis method was not adequate to polymerize PANI and that a two-step synthesis method should be used. A two-step synthesis method was used to polymerize PANI in all other samples.

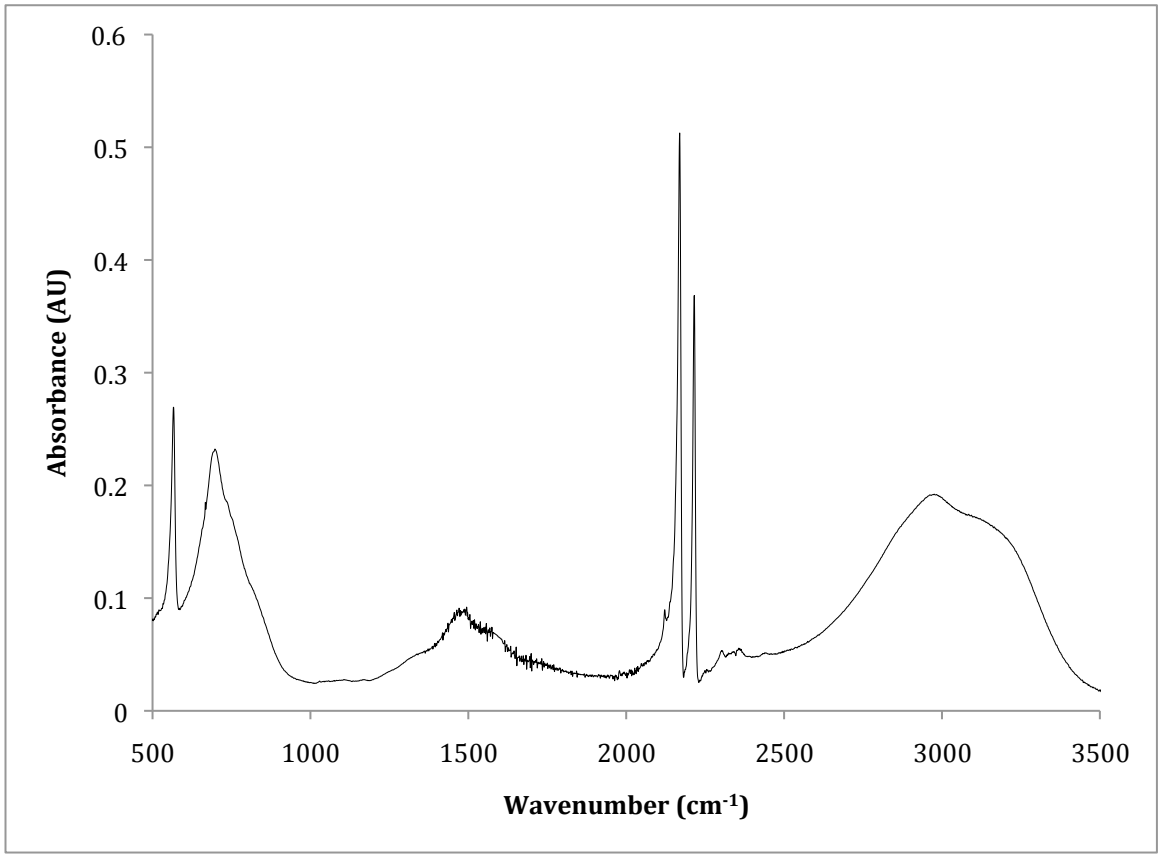

Figure 36. ATR-FTIR spectrum of PANI CP-B.

SEM images of PANI CP-A are shown in Figures 37-38. Crystals of varying diameters (2 μm – 5 μm) can be seen. In all crystals, there seems to be an interface between a light region and a dark region. The light region looks like PANI overgrowth, so the dark region is likely the CP. The two polymers clearly have an interface and an interaction. In Figure 38, a long fibrial polymeric growth can be seen connecting two crystals. An SEM image of PANI CP-B is shown in Figure 39. The morphology of PANI CP-B looks more similar to CP than to PANI CP-A. There is no interface between polymers. It does not appear that there was any PANI synthesized in this approach. Therefore, the one-step synthesis method is inadequate to polymerize PANI. Instead, the two-step synthesis method should be used.

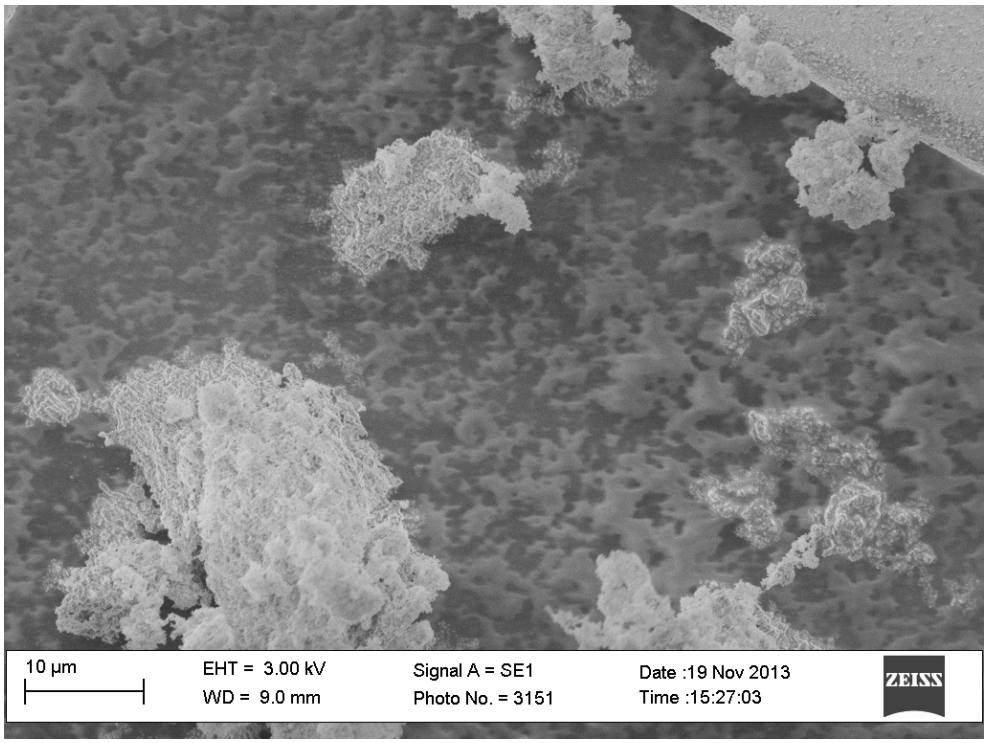

Figure 37. A SEM image of PANI CP-A powder (scale bar = 10 µm). Two different materials can be seen to interface on each crystal.

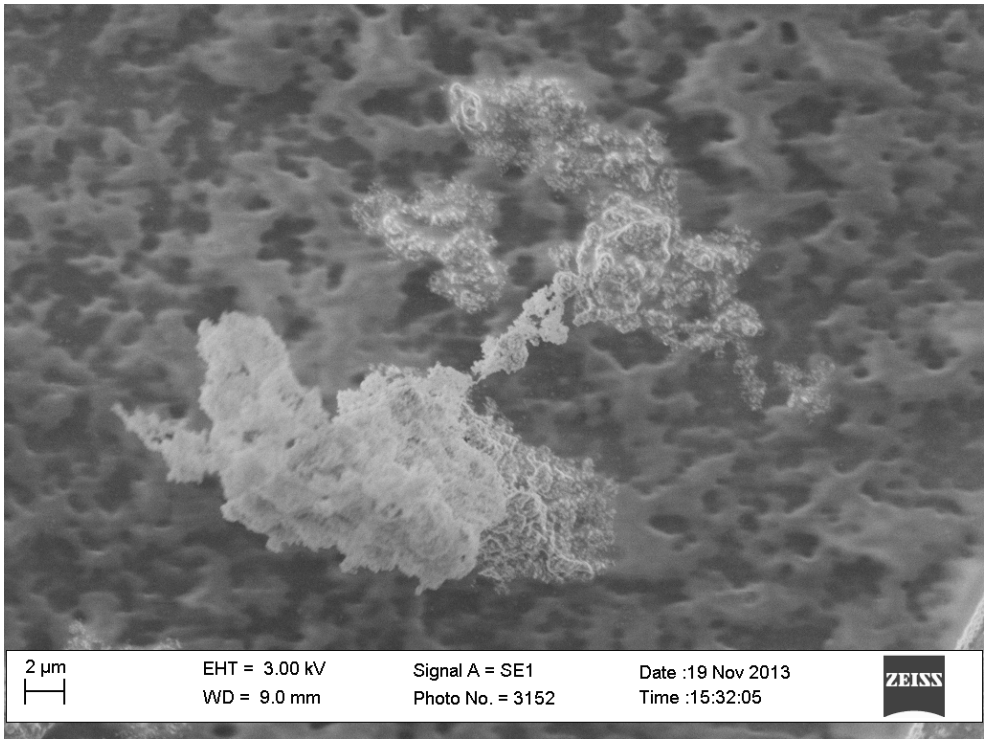

Figure 38. A SEM image of a close-up of Figure 37 (scale bar = 2 µm). A long fibrial polymeric growth can be seen to extend from one material to another.

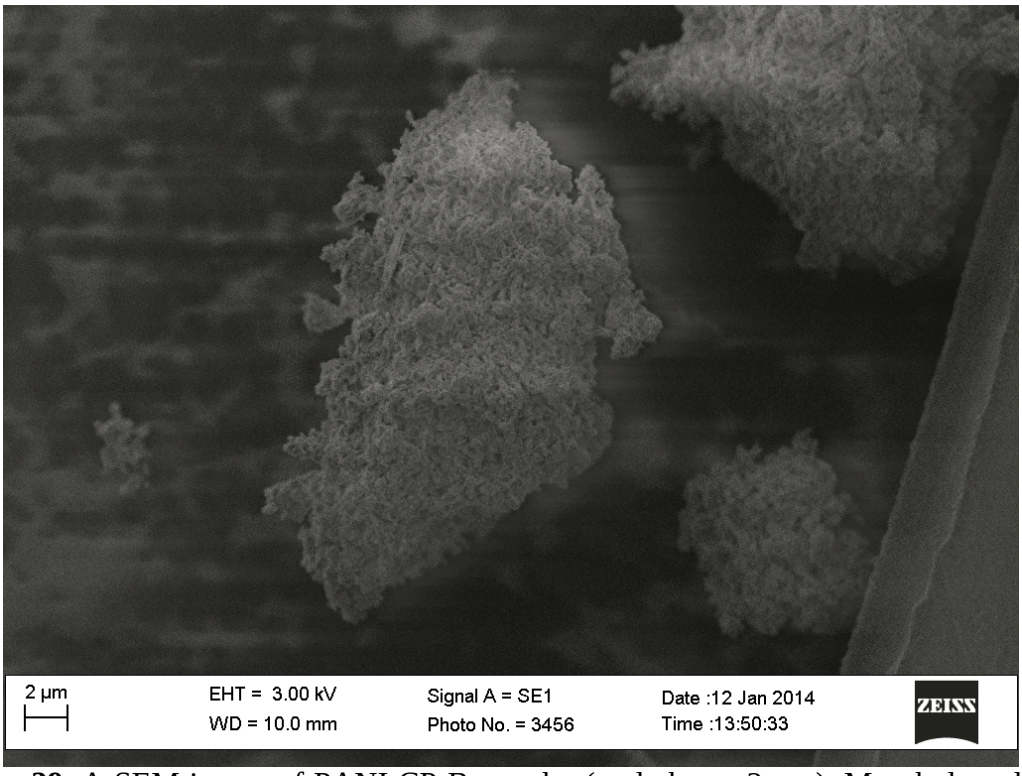

Figure 39. A SEM image of PANI CP-B powder (scale bar = 2 µm). Morphology looks similar to CP. No heterointerfaces were seen.

PANI was polymerized from Lap CP in a two-step synthesis (PANI Lap CP-A). PANI Lap CP-A was examined by ATR-FTIR spectroscopy and SEM. The ATR-FTIR spectrum is shown in Figure 40. Important peaks can be seen at 2950 cm^{-1}, 2210 cm^{-1}, 2170 cm^{-1}, 1100 cm^{-1}, 1060 cm^{-1}, and 830 cm^{-1}, which are attributed to C-H stretching, two C≡N stretches, and internal, surface, and edge Si-O stretches, respectively. When PANI is added to CP composite, the internal and surface Si-O stretches are now distinct peaks. This indicates that the PANI is causing some kind of additional interaction—perhaps a π-bonding interaction—with the surface Si-O, causing its bonding environment to change.

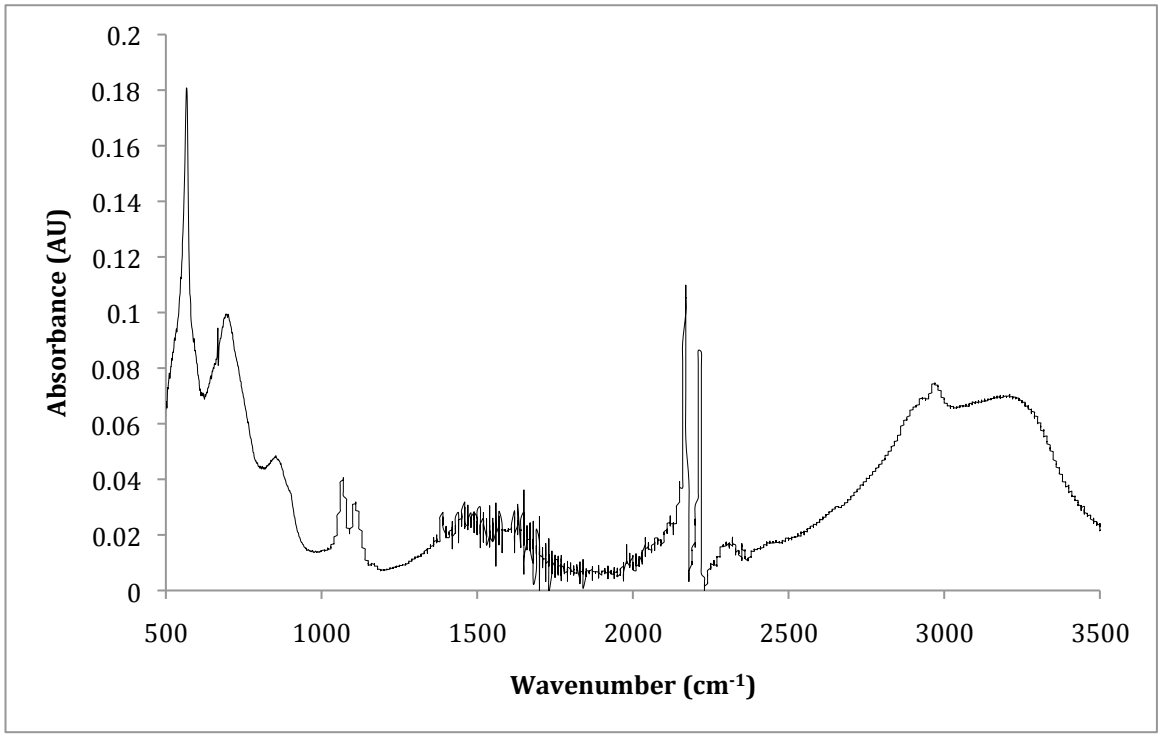

Figure 40. ATR-FTIR spectrum of PANI Lap CP-A.

SEM images of PANI Lap CP-A are shown in Figures 41-42. The polymeric overgrowth seen in PANI Lap CP-A is different from either PANI CP or Lap CP. In PANI Lap CP-A, the polymers are not separated into two distinct phases as in PANI CP. This indicates that the Laponite is templating the polymers in such a way as to increase their interface and interaction with one another, intermingling them into one phase.

Four more PANI Lap CPs were synthesized by changing the ratios of reagents ($K[Au(CN)_2]$, Cu^{2+} Laponite, and aniline HCl). PANI Lap CP-B and -C were synthesized by changing the amount of Laponite, while PANI Lap CP-D and -E were synthesized by changing the amount of aniline HCl. The ATR-FTIR spectra are shown in Figures 43-46.

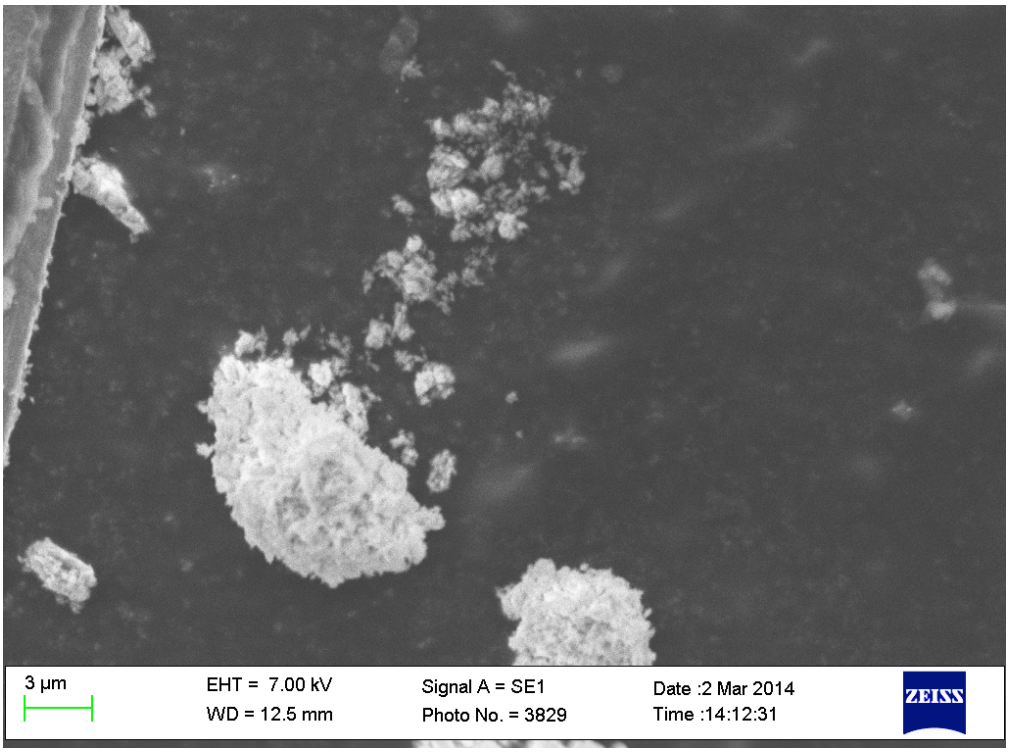

Figure 41. A SEM image of PANI Lap CP-A powder (scale bar = 3 µm). Only one polymer phase is present.

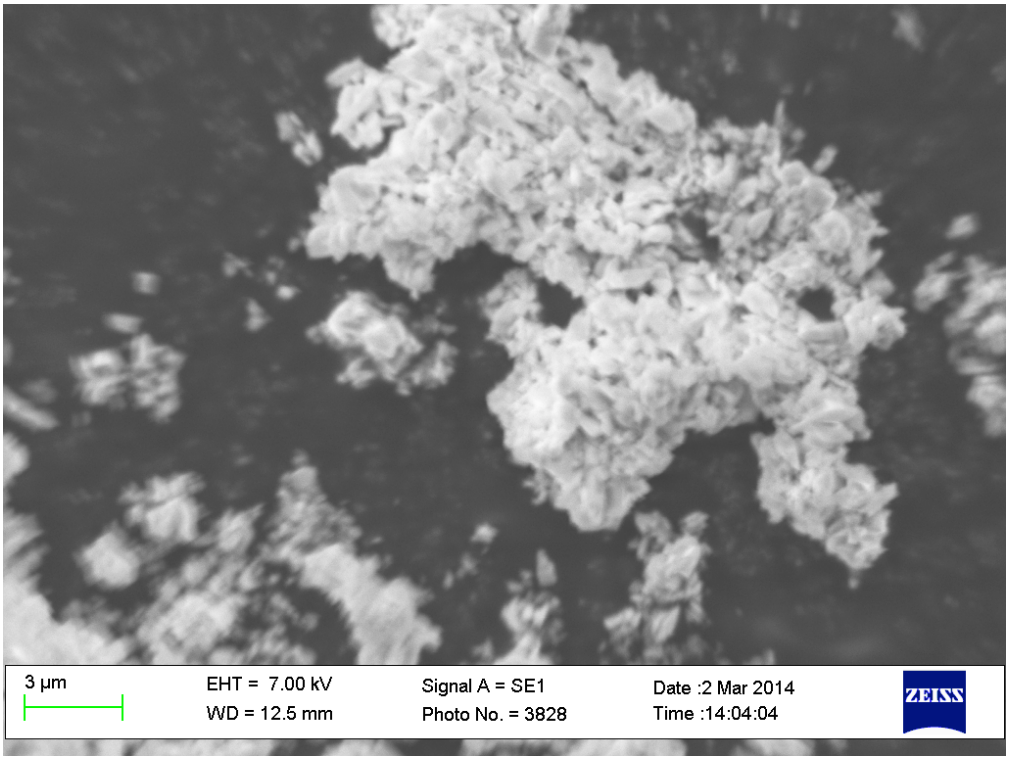

Figure 42. A SEM image of PANI Lap CP-A powder (scale bar = 3 µm). The polymeric growth has different morphology than in either Lap CP or PANI CP.

Major peaks for PANI Lap CP-B can be seen at 2215 cm^{-1}, 2170 cm^{-1}, 1490 cm^{-1}, 1115 cm^{-1}, 1080 cm^{-1}, and 1020 cm^{-1}, which are attributed to two C≡N stretches, C=C benzenoid breathing modes, an internal Si-O stretch, and two surface Si-O stretches. The appearance of a second surface Si-O stretch indicates either that there are two different kinds of surface interactions or that there is some free Laponite and some Laponite that is participating in a surface interaction with another material.

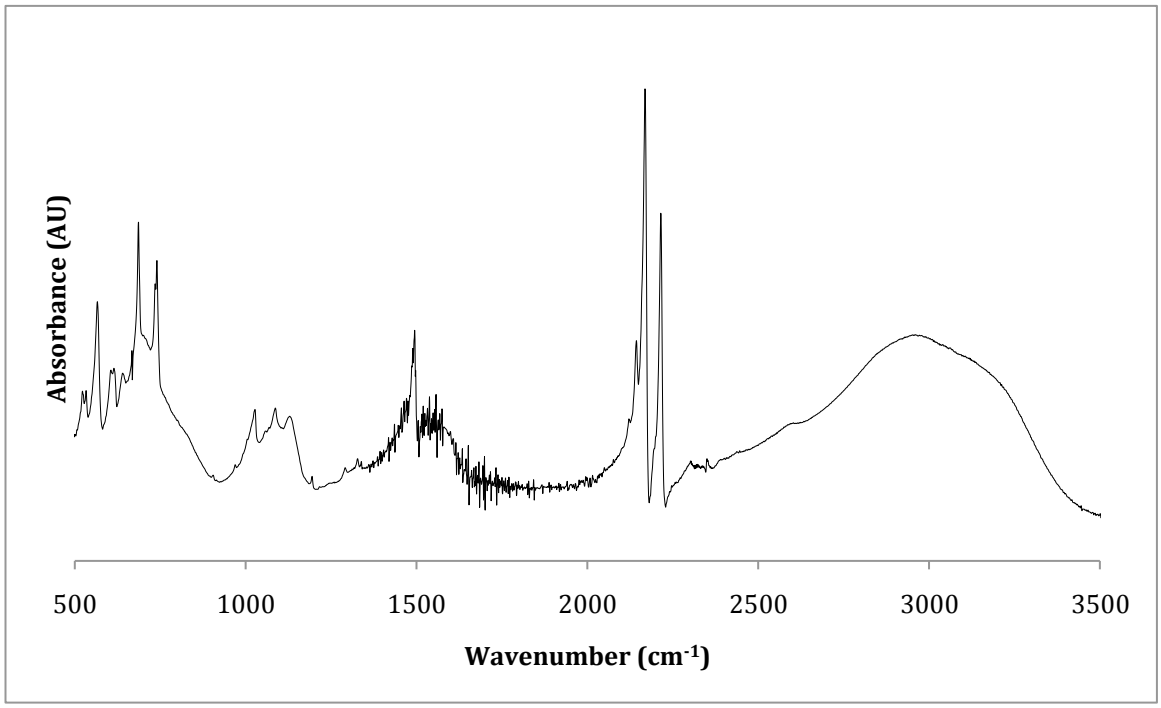

Figure 43. ATR-FTIR spectrum of PANI Lap CP-B.

Major peaks for PANI Lap CP-C can be seen at 2215 cm^{-1}, 2170 cm^{-1}, and 1080 cm^{-1}, which are attributed to two C≡N stretches and a surface Si-O stretch.

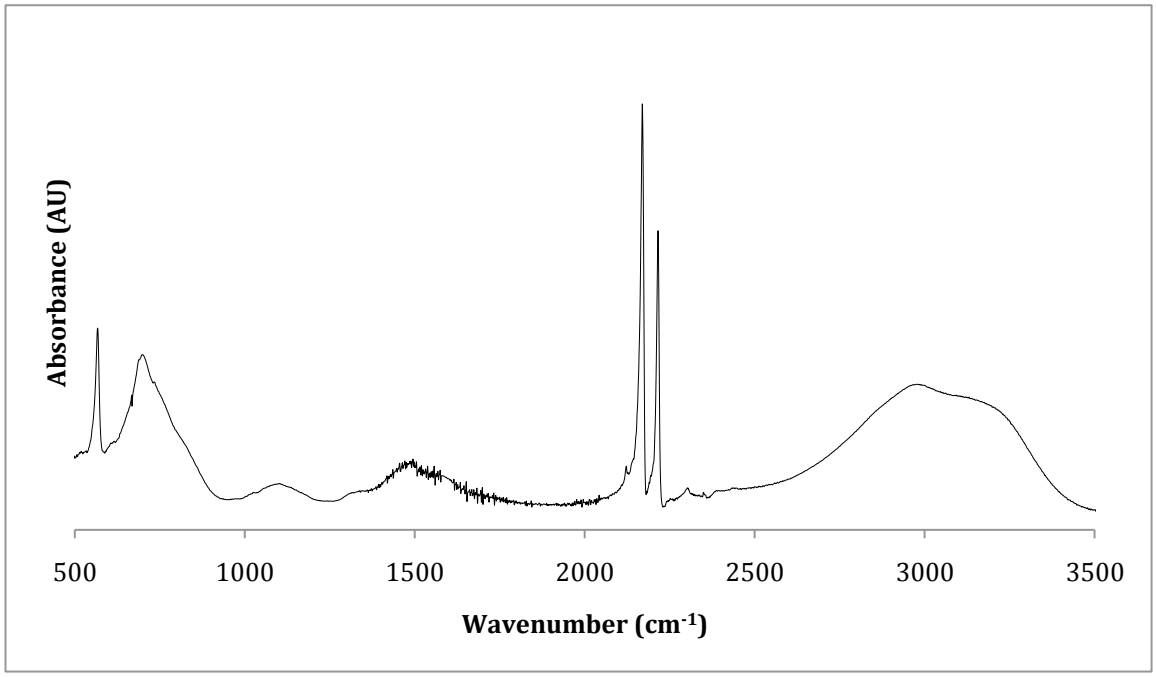

Figure 44. ATR-FTIR spectrum of PANI Lap CP-C.

Major peaks for PANI Lap CP-D can be seen at 2215 cm^{-1}, 2170 cm^{-1}, and 1080 cm^{-1}, which are attributed to two C≡N stretches and a surface Si-O stretch.

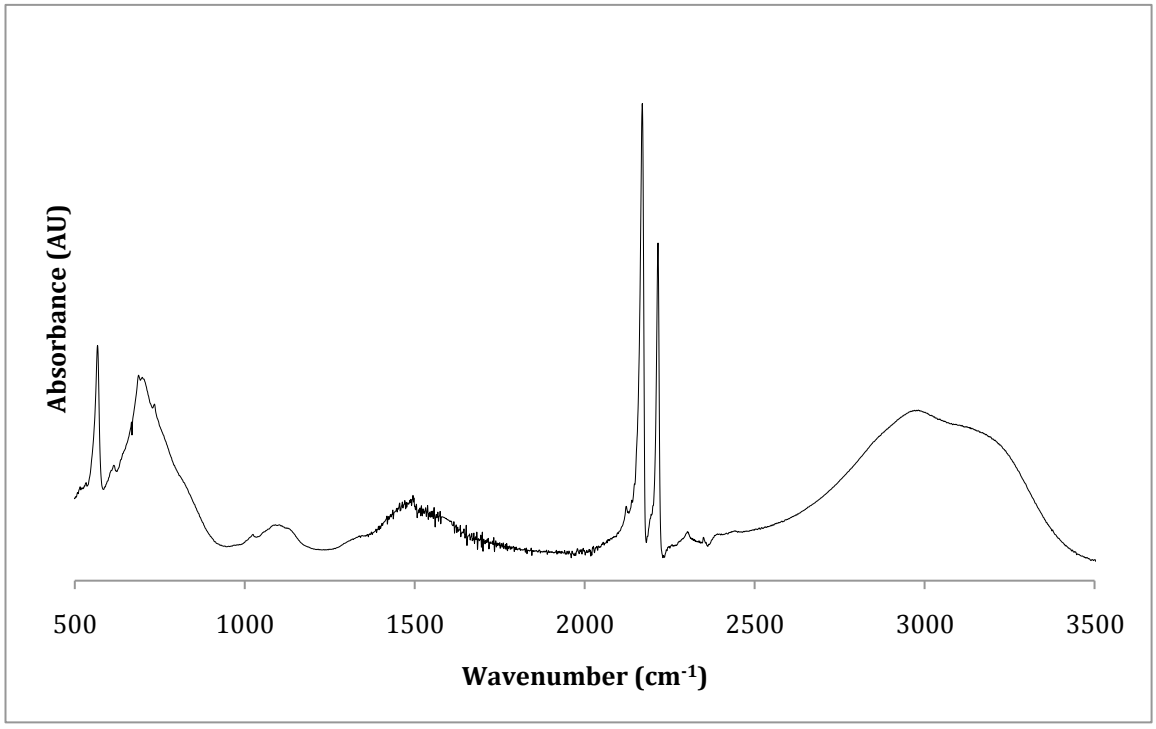

Figure 45. ATR-FTIR spectrum of PANI Lap CP-D.

Major peaks for PANI Lap CP-E can be seen at 2215 cm^{-1}, 2170 cm^{-1}, 1490 cm^{-1}, 1120 cm^{-1}, 1080 cm^{-1}, and 1015 cm^{-1}, which are attributed to two C≡N stretches, a C=C benzenoid breathing mode, an internal Si-O stretch, and two surface Si-O stretches.

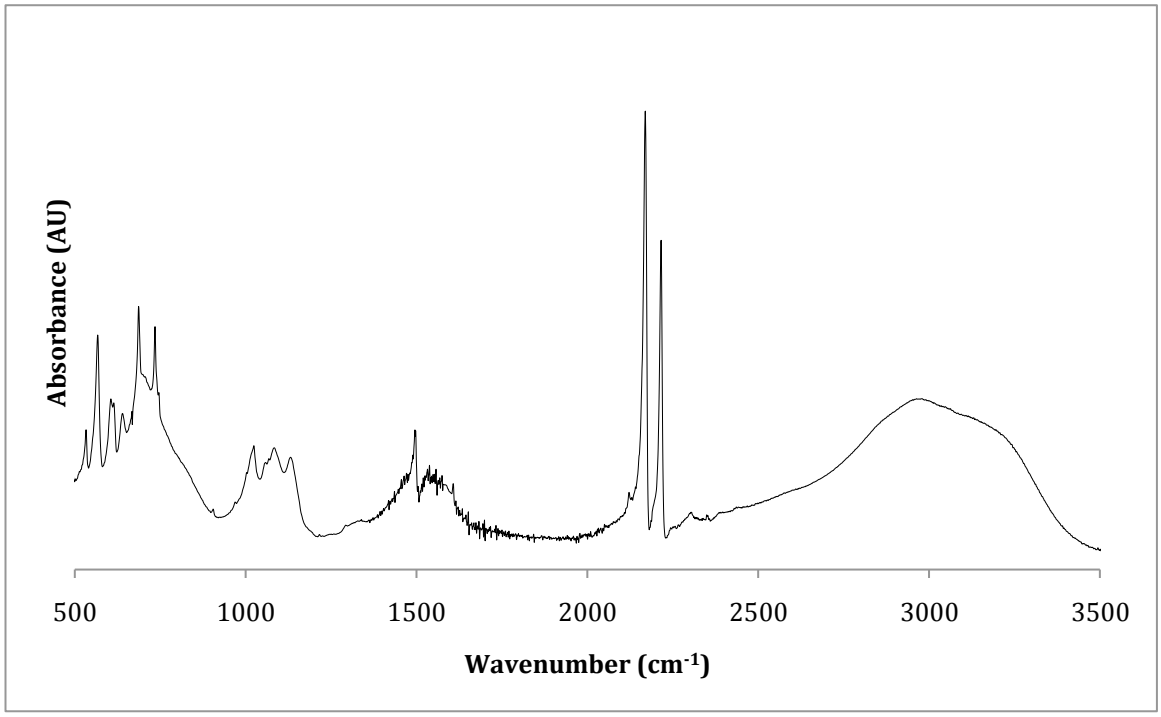

Figure 46. ATR-FTIR spectrum of PANI Lap CP-E.

From the IR spectra, PANI Lap CP-C and -D do not seem to contain PANI. However, hyperfine interference from water and O-H stretching from water may obstruct the characteristic PANI peaks. -C and -D also seem to contain only one bonding environment for the Si-O stretches, or else the peaks have shifted so that they are all overlapping. PANI Lap CP-B and -E, however, both have visible peaks for PANI and three distinct peaks for the Si-O stretches. However, instead of one edge, one surface, and one internal peak, there seem to be two surface peaks and one internal peak in both cases.

3.3. Structure and Morphology of Films

Films were cast from water for the five PANI Lap CP composites. A PANI Lap CP (a) film that was cast on glass was examined by UV-vis spectroscopy. Its UV-vis spectrum is shown in Figure 47. The composite absorbs over a wide range of wavelengths from the ultraviolet to visible region. While we have not yet loaded our material with the chromophore, this photoabsorption within the material may serve to increase photoabsorption within the chromophore. However, if the photoabsorption within the material is preventing photoabsorption within the chromophore, it will prove deleterious to the device efficiency. Further UV-vis studies in conjunction with bulk conductivity and pcAFM measurements will help to shed light on this issue.

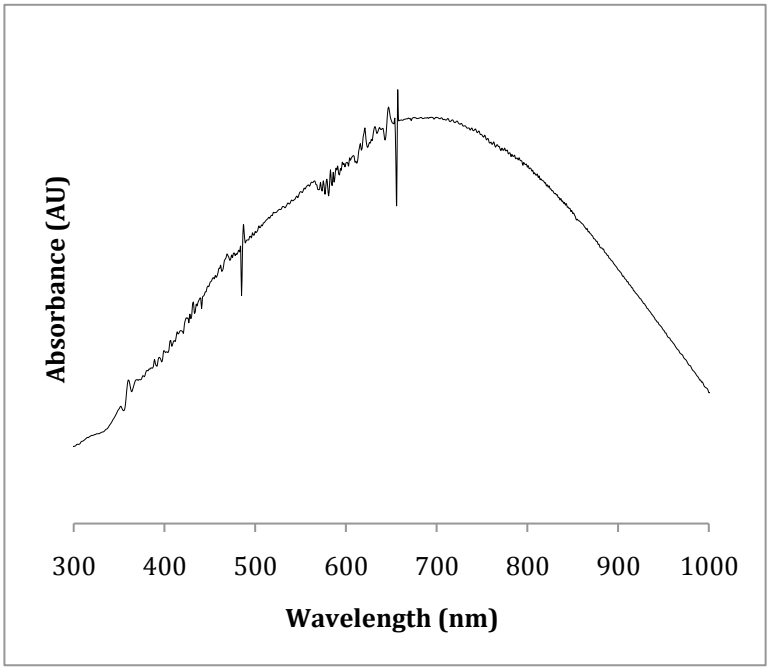

Figure 47. UV-vis absorption spectrum of PANI Lap CP-A.

XRD spectroscopy was also conducted for a PANI Lap CP-A film cast on glass. The XRD spectrum is shown in Figure 48. The XRD indicates that at least some portion of the composite exhibits long-range order. The CP can exhibit long-range order because

of Au···Au aurophillic interactions.[21,31a] The Au atoms between polymer chains can align in such a way as to create a three-dimensional stacked array of polymer chains. The Au atoms could also participate in intra-chain interactions.[31a] PANI can also be ordered as it has the ability to H-bond and π-stack with itself or other materials[31d-e]

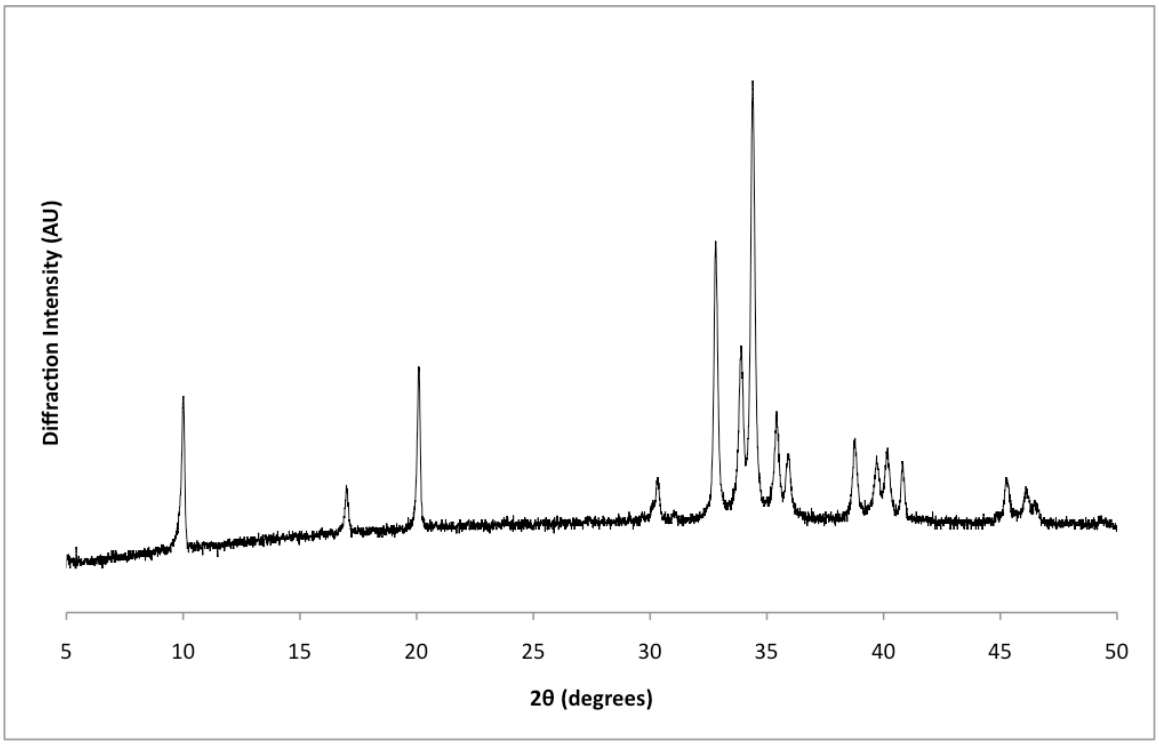

Figure 48. XRD spectrum of PANI Lap CP-A film.

All five PANI Lap CP composites were cast directly on an SEM stub for imaging. SEM images of PANI Lap CP-A film are shown in Figures 49-53. The film is quite continuous and smooth. Some polymer overgrowth on the film can be observed in Figure 53. This polymer overgrowth resembles that for PANI Lap CP-A powder. Where the film has cracked (likely as a result of drying too quickly), some material has pulled out from inside the film. If the cracks are narrow enough, wire- and wires-upon-wires-like growth stretches from one side of the crack to the other, as if it were pulled out when the film cracked (Figures 50-53). Some of the wire-like growth resembles the stacked-tower

PANI growth described by Tran, et al.[27] (Figures 51 and 53). Additionally, lamellar stacking is observed in the cracks (Figure 51). This is typical morphology for Laponite.[32] Thus, it is likely that Laponite is templating polymer-chain stacking when the composite is dispersed in water.

SEM images of PANI Lap CP-B film are shown in Figures 54-57. The -B film does not resemble the -A film; instead, there is a continuous film with thick polymeric overgrowth. In addition, agglomerated sac-like structures could be observed throughout the film (Figure 56). The individual sacs were about 1 μm or less in diameter and agglomerated to form structures with an average diameter of about 2 μm. PANI spheres have been observed before.[27,33] pH appears to be an important factor in the formation of PANI spheres, though the pH was not adjusted at all during the mechanochemical synthesis. Finally, a few open tubular structures were observed (Figure 57). These may have been the result of polymer chains forming sheets, and then the polymer sheets rolling into a tube.

SEM images of PANI Lap CP-C film are shown in Figures 58-66. PANI Lap CP-B exhibits an incredible range of morphologies. There are hollow colloidosomes, different kinds of flower-like growth, nanoweb growth, flat sheets, and fractal growth, among other things. This incredible variety was not noted among the other PANI Lap CP films. The film itself more closely resembles -B than -A in that it simply has a layer of polymer overgrowth. In -C, however, the polymer layer is much thinner than in -B (Figure 58).

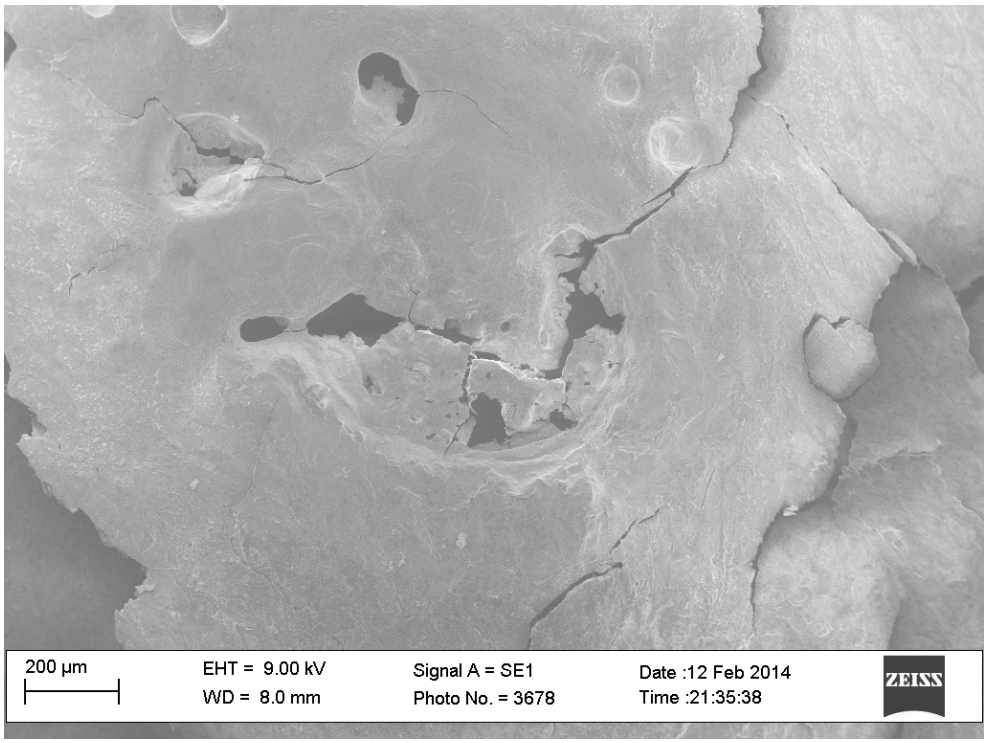

Figure 49. A SEM image of PANI Lap CP-A film (scale bar = 200 µm). The film is quite continuous with some small cracks or holes.

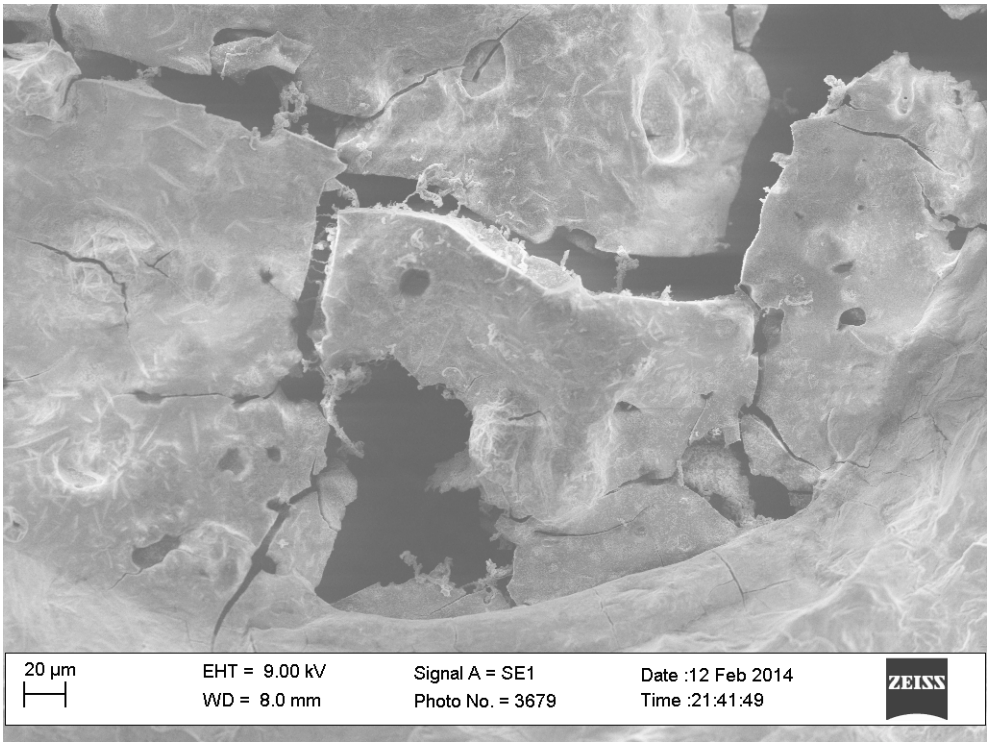

Figure 50. A SEM image of a close-up of Figure 49 (scale bar = 20 µm). The material has pulled out where the film is cracked.

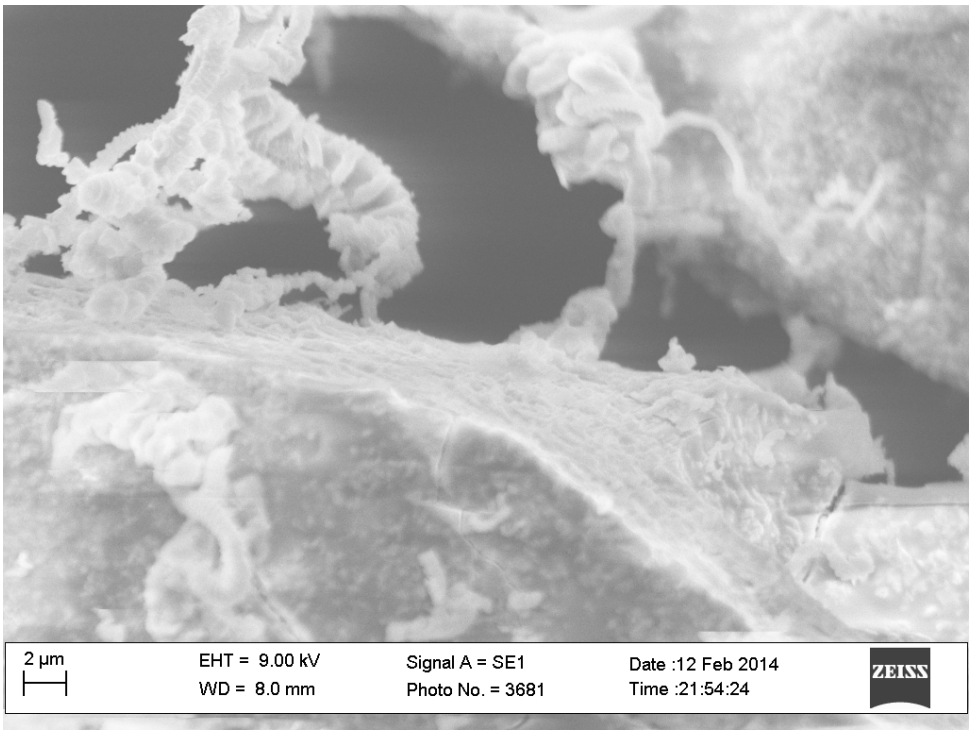

Figure 51. A SEM image of a close-up of Figure 50 (scale bar = 2 µm). There are wires and wires-upon-wires growing across the cracks. Lamellar stacking can also be seen inside the crack.

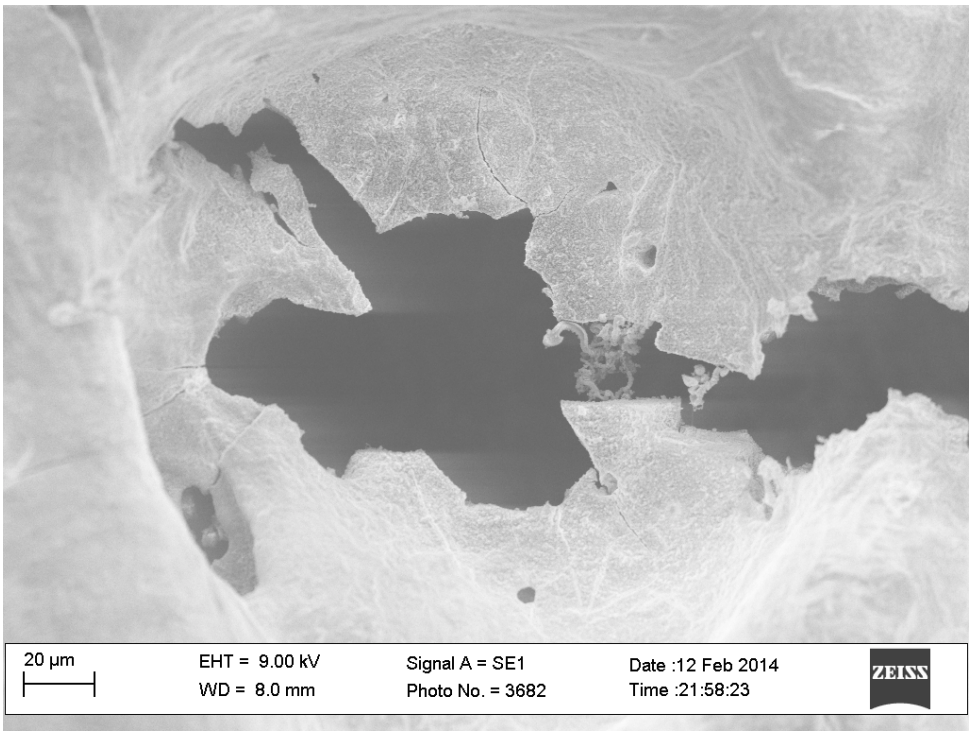

Figure 52. A SEM image of PANI Lap CP-A film (scale bar = 20 µm). Where the cracks are narrow enough, wires and wires-upon-wires grow between the cracks.

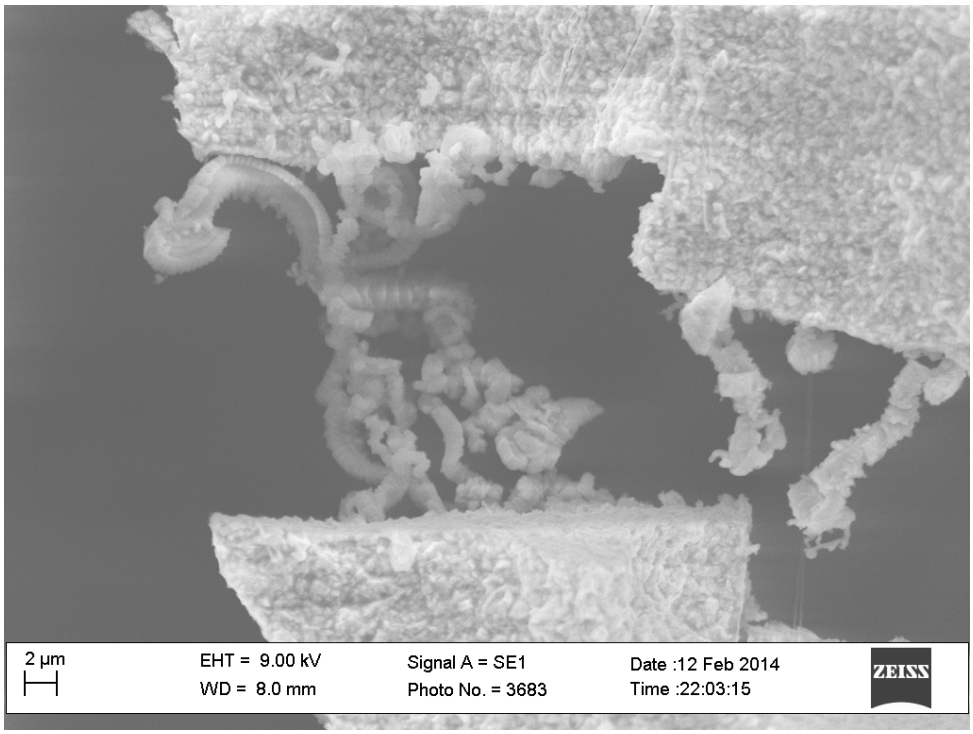

Figure 53. A SEM image of a close-up of Figure 52 (scale bar = 2 µm). The polymeric overgrowth on the film can be seen clearly. The wire-like growth resembles stacked-tower PANI growth.

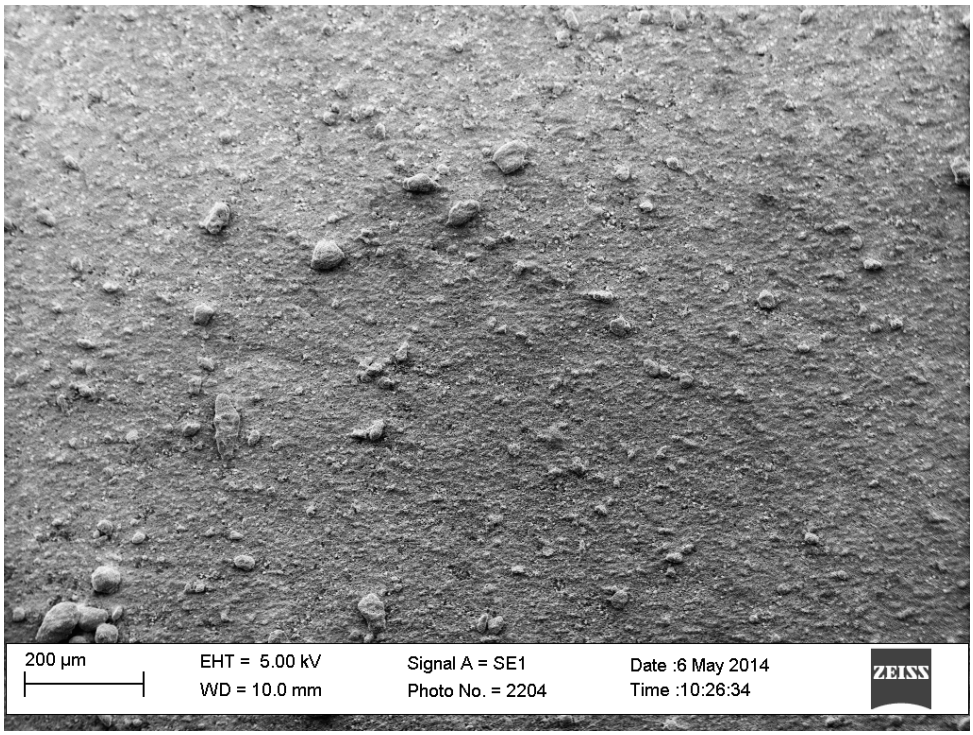

Figure 54. A SEM image of PANI Lap CP-B film (scale bar = 200 µm). The film is fairly smooth with thick polymeric overgrowth.

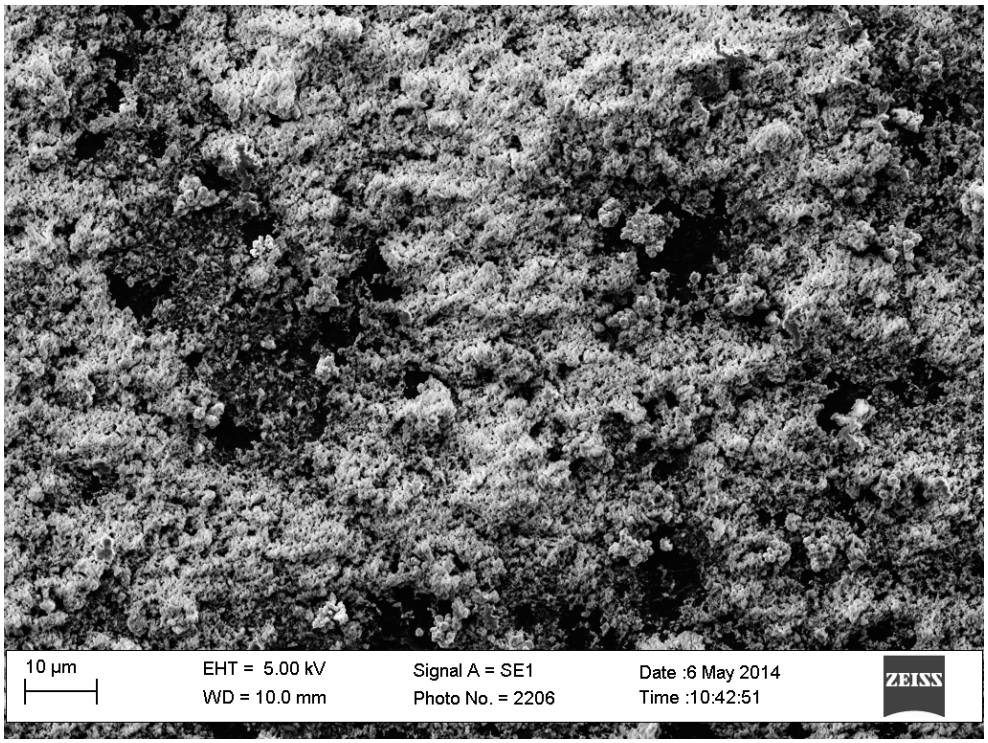

Figure 55. A SEM image of a close-up of Figure 54 (scale bar = 10 µm). Thick polymeric overgrowth is present over the film.

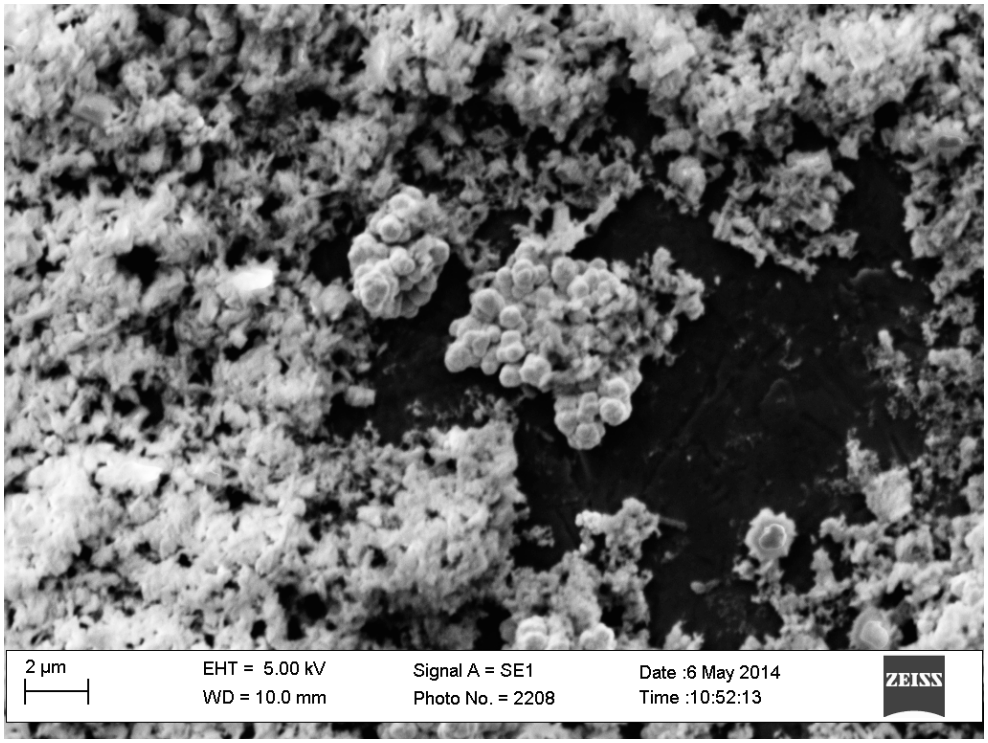

Figure 56. A SEM image of polymeric growth and agglomerated sac-like structures (scale bar = 2 µm).

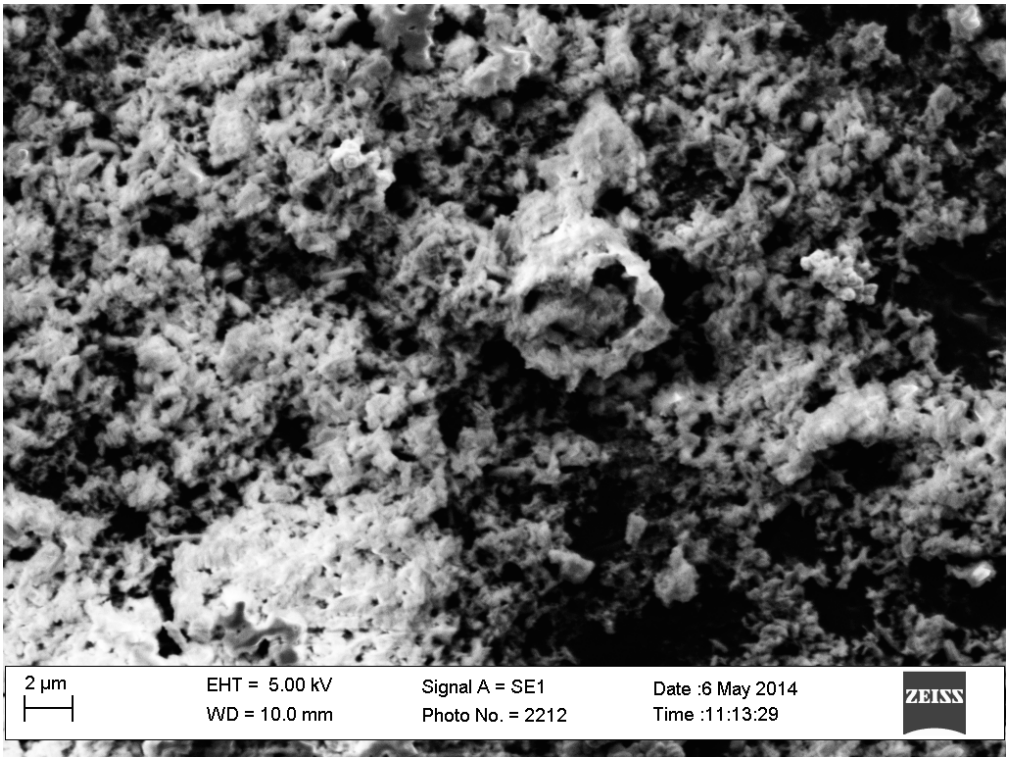

Figure 57. A SEM image of an open tubular structure (scale bar = 2 µm). The tubular structure may be the result of polymer sheets rolling up.

The first major structure observed was hollow colloidosomes (Figures 58-61). These colloidosomes were large, with an average diameter of about 20 µm. They were hollow and made up of what appears to be polymeric growth. In Figure 60, it can be clearly seen that the inside of the colloidosome matches the outside, indicating that, again, polymer sheets may have wrapped around another material to form the colloidosomes, similar to the tubular structures observed in -B. In Figure 62, there is what appears to be either an unfinished or burst colloidosome. This seems to indicate that there is some sort of templating growth that was once inside the colloidosomes. The colloidosomes produced here are somewhat similar to the "hollow sphere" PANI structures described by Tran, et al.[27]

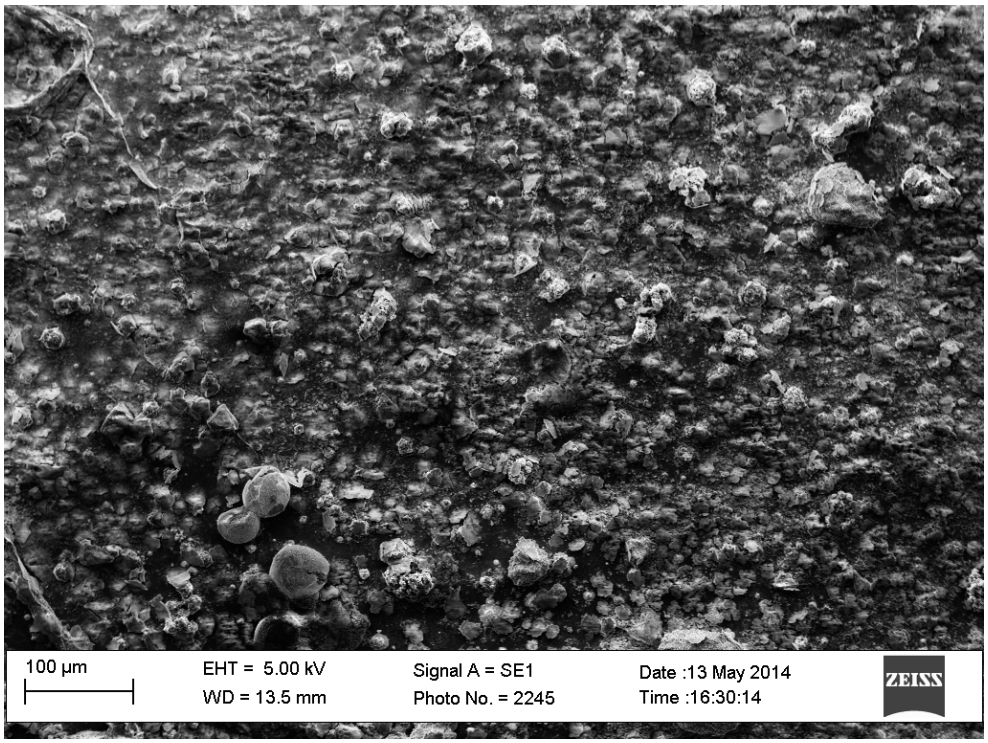

Figure 58. A SEM image of PANI Lap CP-C film (scale bar = 100 µm). The surface is somewhat smooth with plenty of polymer overgrowth.

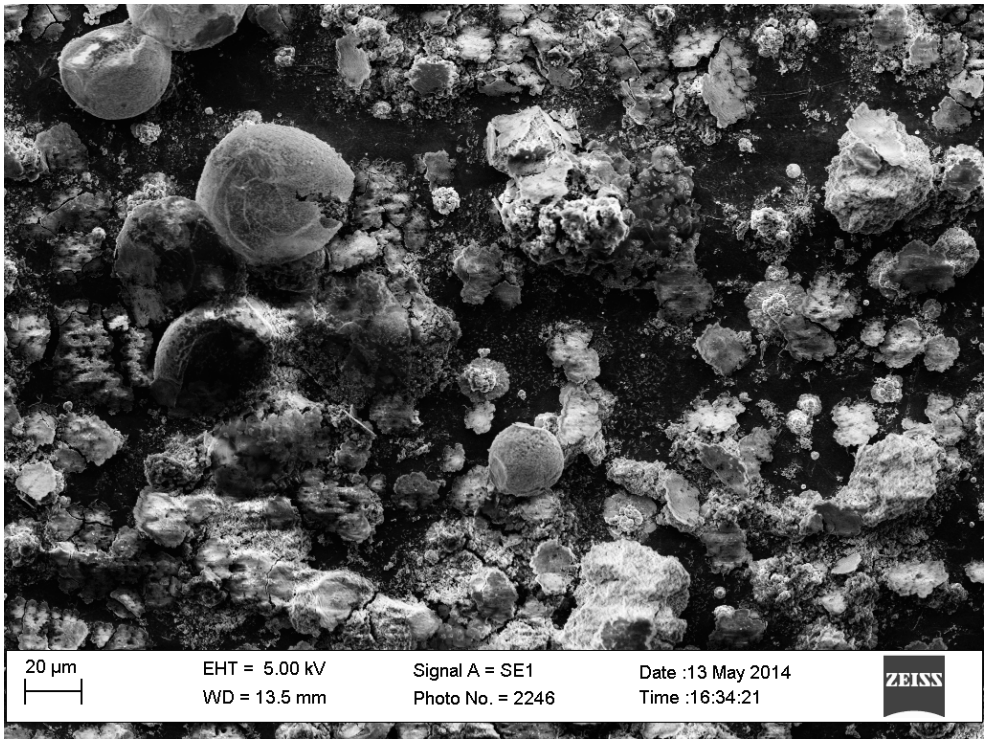

Figure 59. A SEM image of a close-up of Figure 58 (scale bar = 20 µm). The number of different kinds of structures present in the film can be seen quite obviously.

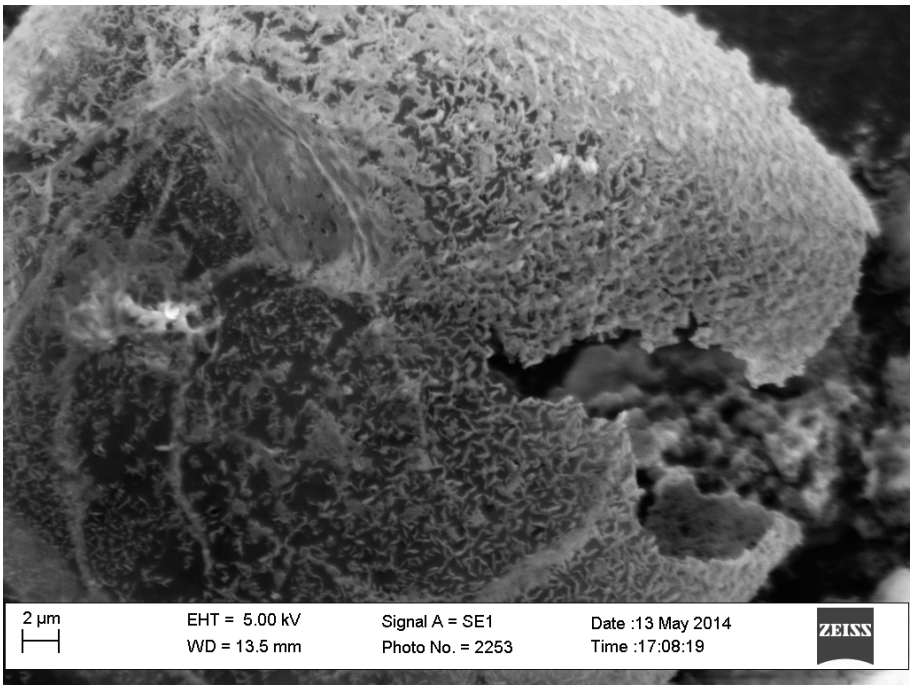

Figure 60. A SEM image of a close-up of Figure 59 (scale bar = 2 µm). Several colloidosome structures formed in the composite film. They are mostly hollow. In this image, it can be seen that the inside and the outside of the colloidosome share the same morphology.

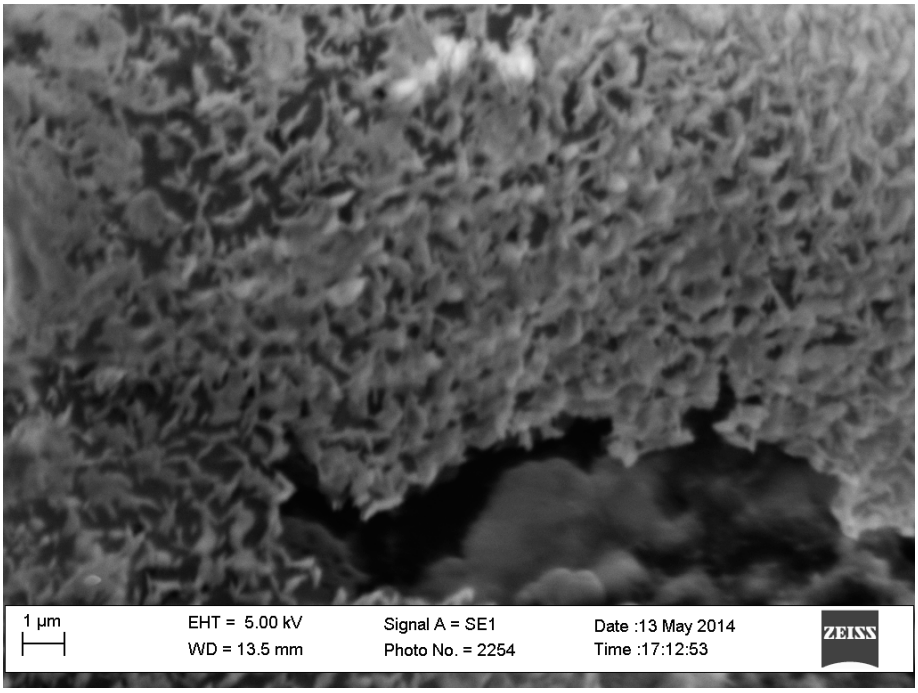

Figure 61. A SEM image of a close-up of Figure 60 (scale bar = 1 µm). The colloidosome is coated in polymeric growth.

In the bottom-right of Figure 62, small rose-like growth can be observed. The flowers are 1-2 μm in diameter, with nanoscale petals. Tran, et al also describes PANI roses.[27] In Figure 63, a different kind of flower-like growth is seen. This flower in about 5 μm in diameter, with microscale petals. On the surface of the film, nanoscale petal-like structures can be observed. These are similar in shape to the polymeric growth making up the colloidosomes. This second type of flower-like growth has been observed previously. Guo, et al. observed similar structures when aniline was added to a gold salt.[34] To the left of Figure 63, urchin-like structures can be seen. Again, Tran, et al describe the ability for PANI to make that type of structure.[27] Peace, et al also saw urchin-like structures in vanadium-templated PANI films.[35a] In Figures 64, 65, and 66, nanoweb growth, sheets, and fractal growth, respectively, are also observed. Zhang, et al describe the ability of Zn-based coordination polymers to form similar sheet-like structures to what is observed in Figure 65.[35b]

A future goal will be to tune the morphosynthetic parameters to yield control over morphology and to determine why so many structures are seen. One reason why so many structures are formed may be the use of the mechanochemical route. In the corresponding aqueous-based PANI reactions, the product is usually uniform in morphology. However, in the mechanochemical synthesis, a mix of morphologies is observed. Perhaps this is because in the solution-based reactions, generally only one morphosynthetic parameter may be changed. For example, the reaction could be run at a specific pH or a specific temperature, and this parameter will be the same throughout the solution. In the mechanochemical reaction, however, the reaction conditions may not be uniform throughout. Even the ratio of reagents may not be the same in different areas of the

mortar, so the composite could be ground together at several different ratios even within the same mortar. The temperature could also vary as some portion of the powder is ground and some portion is not. The variation in these parameters could certainly lead to the variety of morphologies seen.

Even though the ATR-FTIR of -C indicates that there may not be much, if any, PANI in the composite, it is clear from the number and type of structures present here that there is PANI and that it is playing a key role in the formation of these structures. The increased amount of Laponite seems to increase the number of different structures that can be templated. It is obvious from these SEM images that Laponite can act as a structure-directing agent leading to varied morphologies.

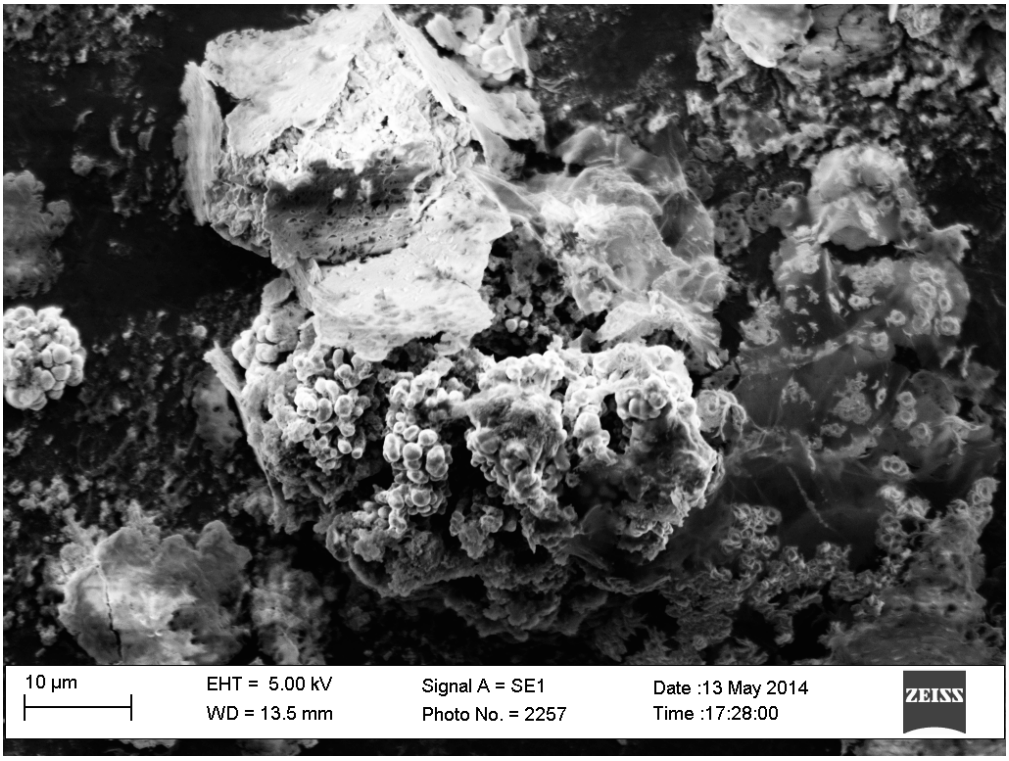

Figure 62. A SEM image of some structures that may be incomplete or burst colloidosomes (scale bar = 10 µm). To the left, an agglomerated sac-like structure (as in -B) can be seen. In the bottom right, rose-like structures can be seen.

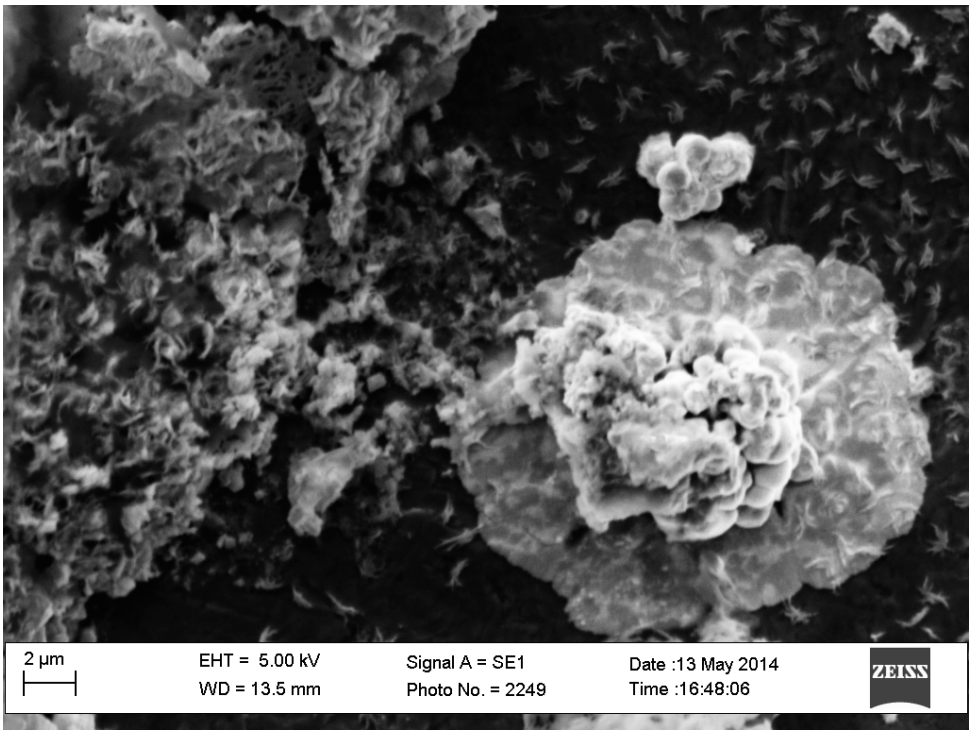

Figure 63. A SEM image of another flower-like structure (scale bar = 2 µm). At the surface of the film, small petal-like structures are seen. Urchin-like structures can also be observed to the left.

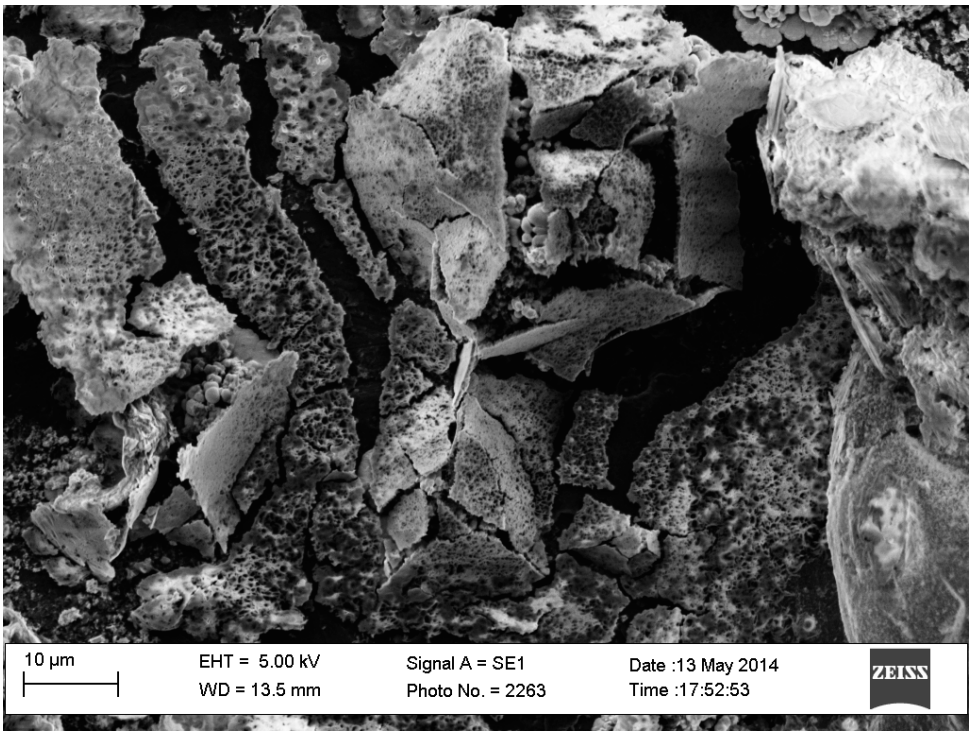

Figure 64. A SEM image of nanoweb growth covering two-dimensional sheets (scale bar = 10 µm).

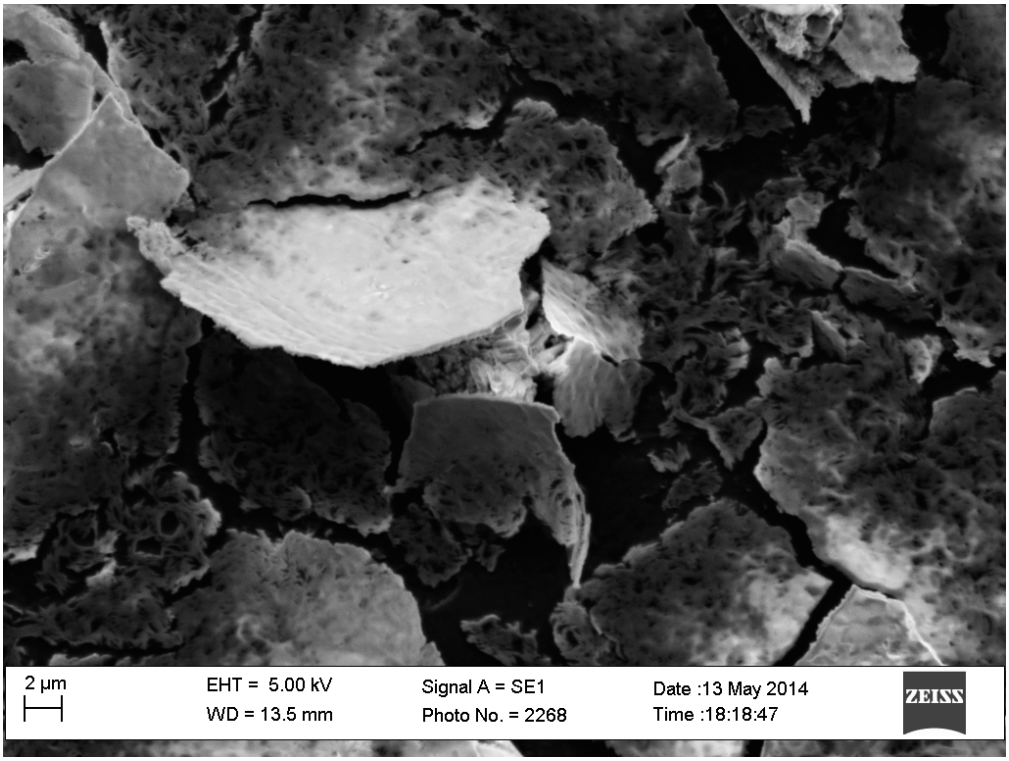

Figure 65. A SEM image of two-dimensional sheets (scale car = 2 µm).

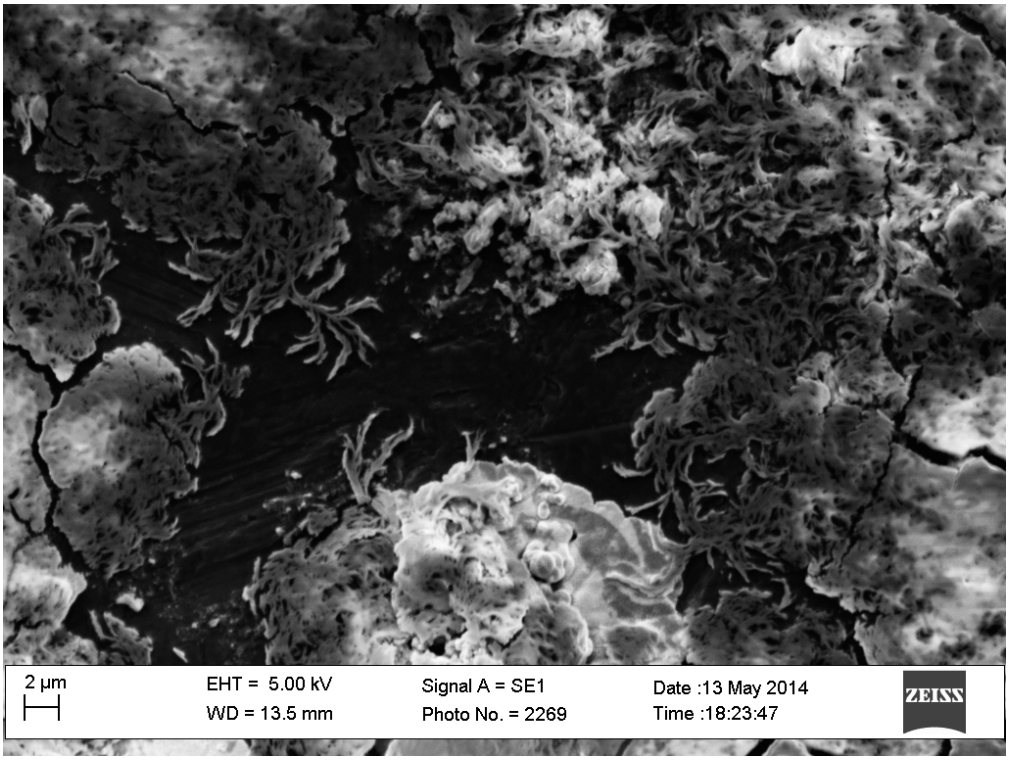

Figure 66. A SEM image of fractal growth (scale bar = 2 µm).

SEM images of PANI Lap CP-D are shown in Figures 67-71. The polymeric growth in -D results as evenly-sized, evenly-dispersed particles. In Figure 68, agglomerated sac-like growth can be seen yet again. Figure 69 reveals another hollow tubular polymer structure. Figure 70 shows a region where the polymeric growth is thicker. In many places, that thicker growth has an urchin-like structure (Figure 71).

SEM images of PANI Lap CP-E are shown in Figures 72-77. The overall film morphology looks similar to that in -D, but a region of thicker growth was mostly explored (Figure 72). This film also had fairly varied morphologies. The thick polymeric growth seen in Figure 73 resembles PANI overgrowth. In Figure 74, a large structure with some sheet-like morphology can be seen. The bottom center of the structure is coated with small nanoscale dots. These may be agglomerated Laponite nanodisks. Figure 75 shows a large sheet-like structure as well as some lamellar stacking. Finally, the wires-upon-wires growth was observed again (Figures 76 and 77). A hollow sphere structure is also observed in Figure 76. This structure more closely resembles the hollow spheres depicted in Tran, et al.[27] and is likely comprised of only PANI nanostructures.

Because the wires-upon-wires growth was observed only in films that had a relatively large amount of aniline HCl, it is likely that the wires-upon-wires growth is indeed the result of an interface between the CP and PANI.

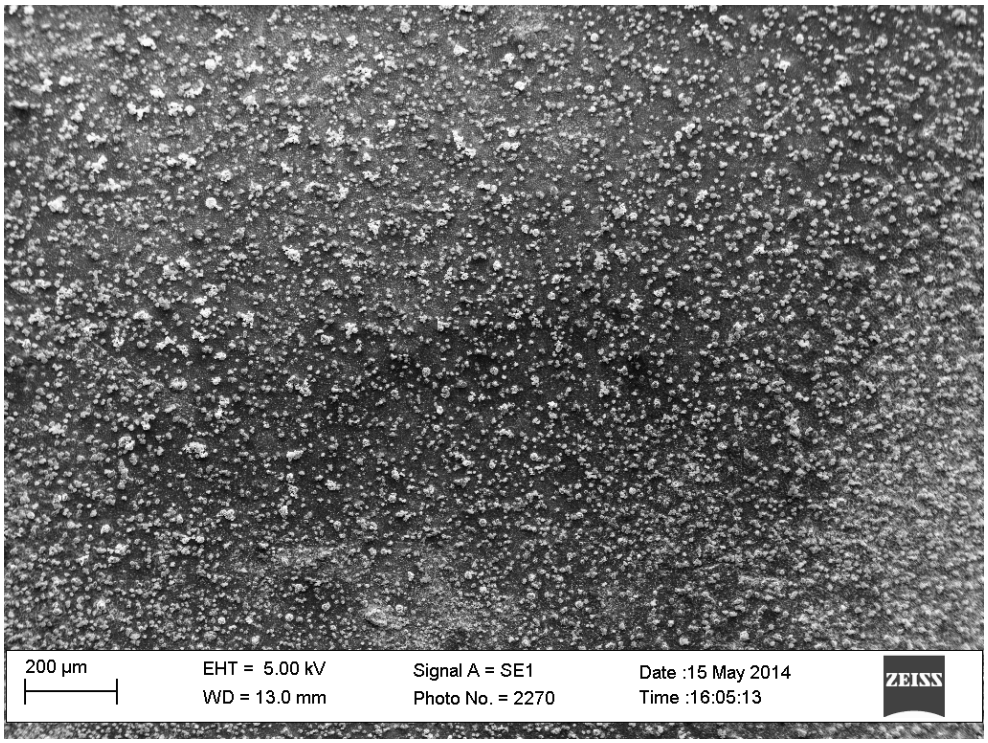

Figure 67. A SEM image of PANI Lap CP-D film (scale bar = 200 µm). The polymeric growth results in evenly-sized and distributed particles.

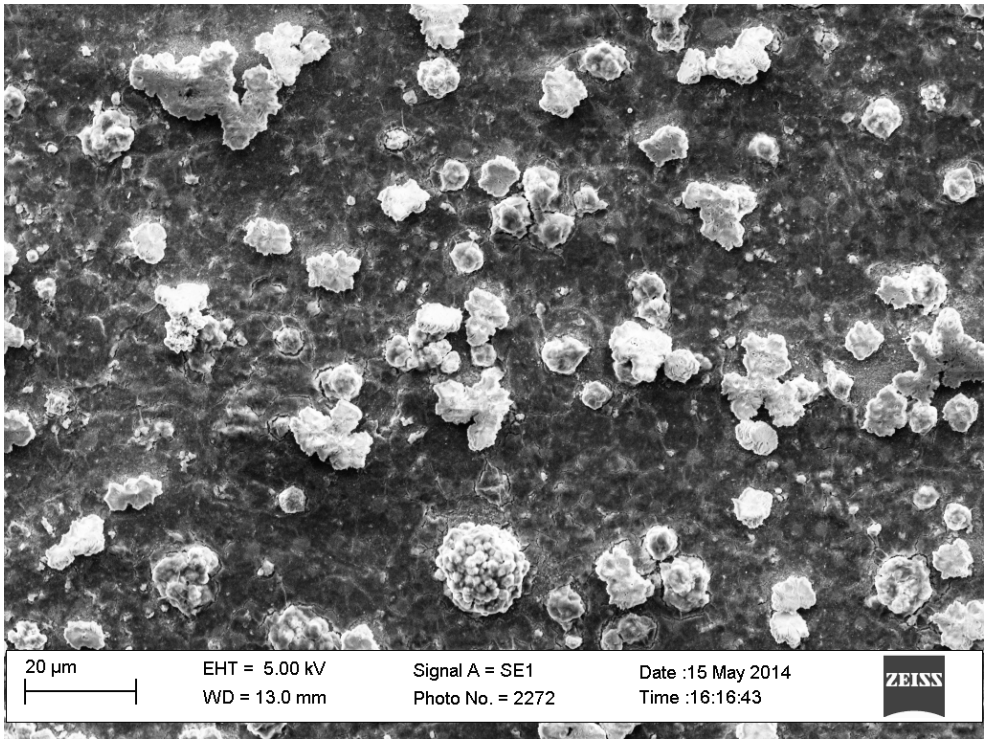

Figure 68. A SEM image of a close-up of Figure 67 (scale bar = 20 µm). More agglomerated sac-like structures are observed.

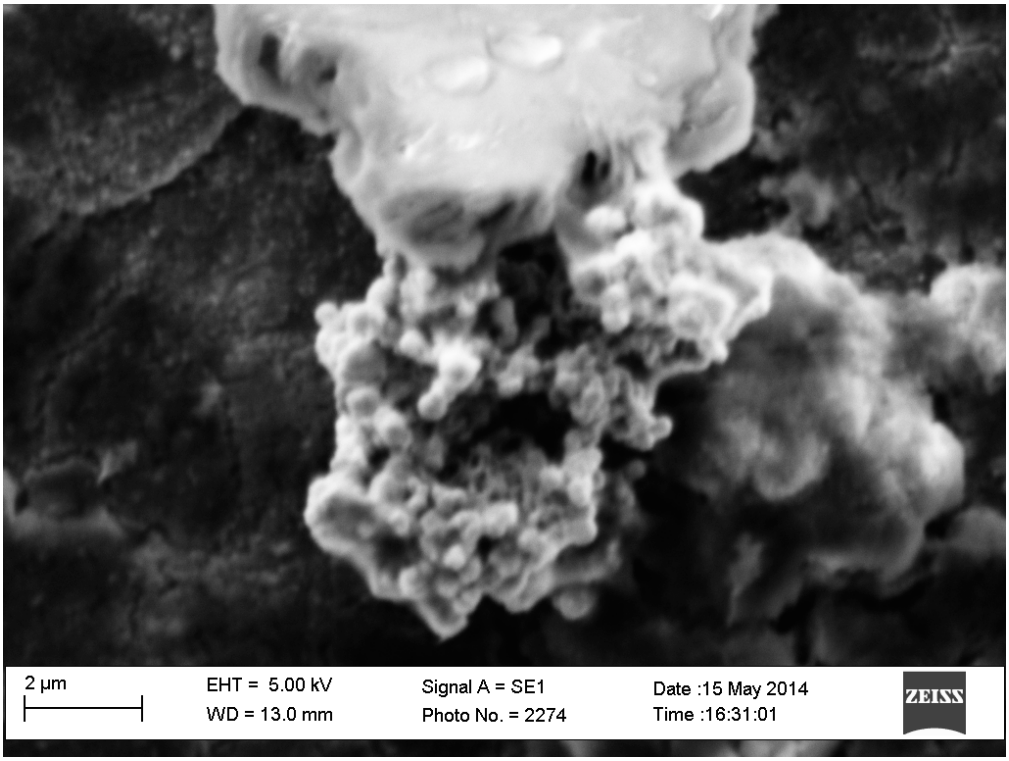

Figure 69. A SEM image of a hollow tubular structure (scale bar = 2 µm).

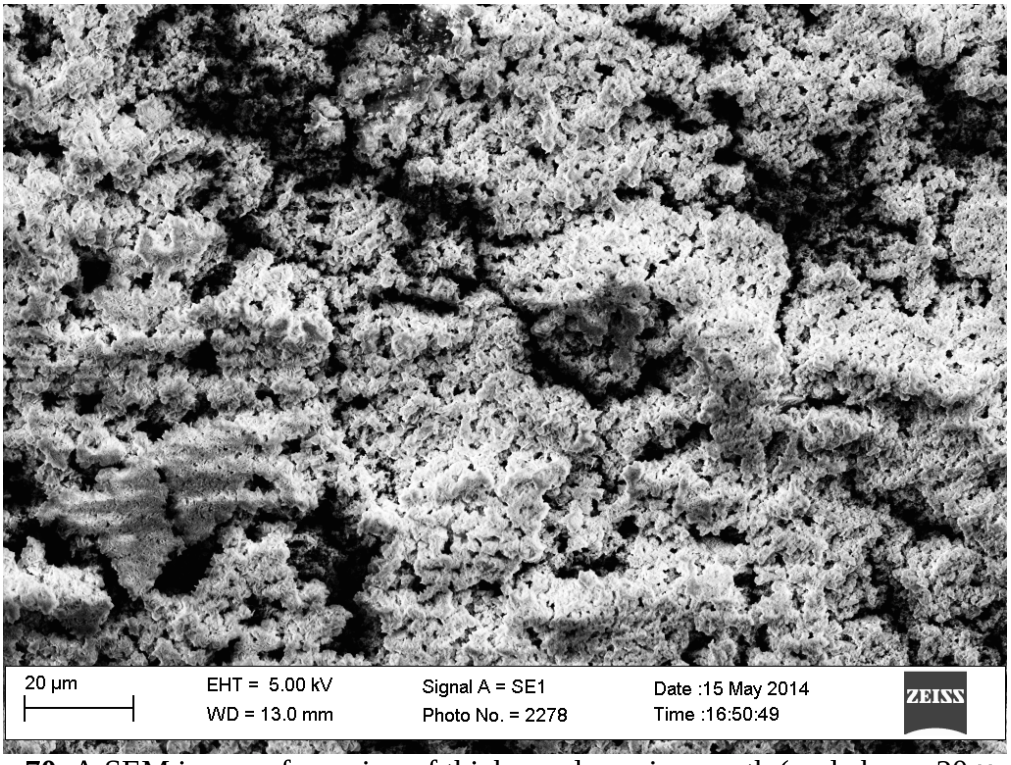

Figure 70. A SEM image of a region of thicker polymeric growth (scale bar = 20 µm).

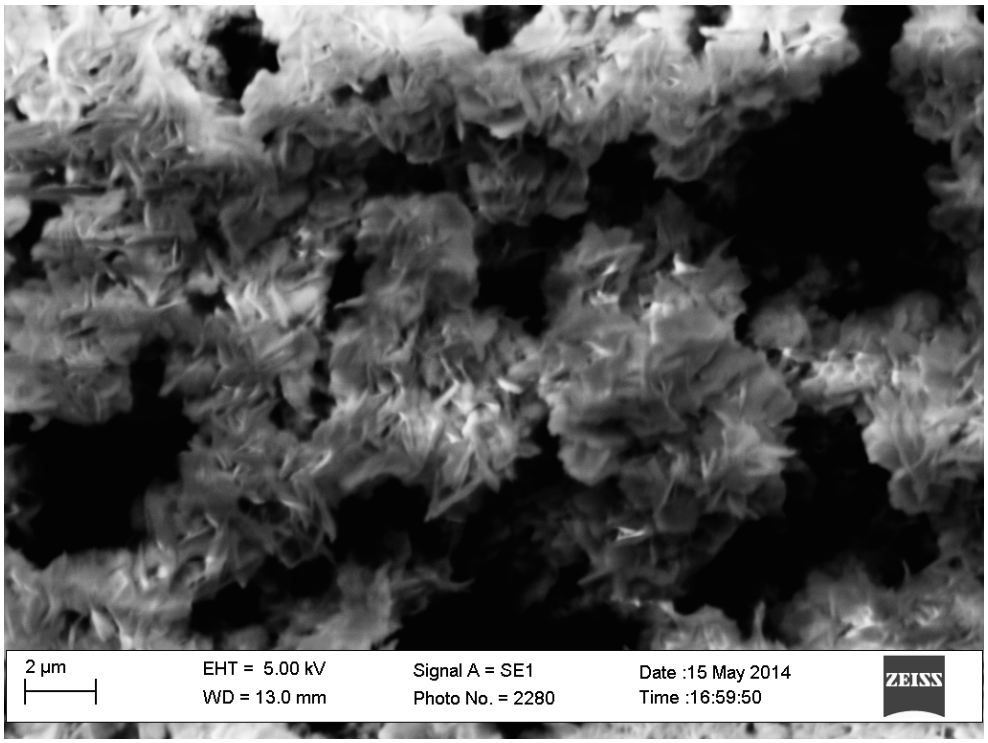

Figure 71. A SEM image of a close-up of Figure 70 (scale bar = 2 µm). Urchin-like growth is observed.

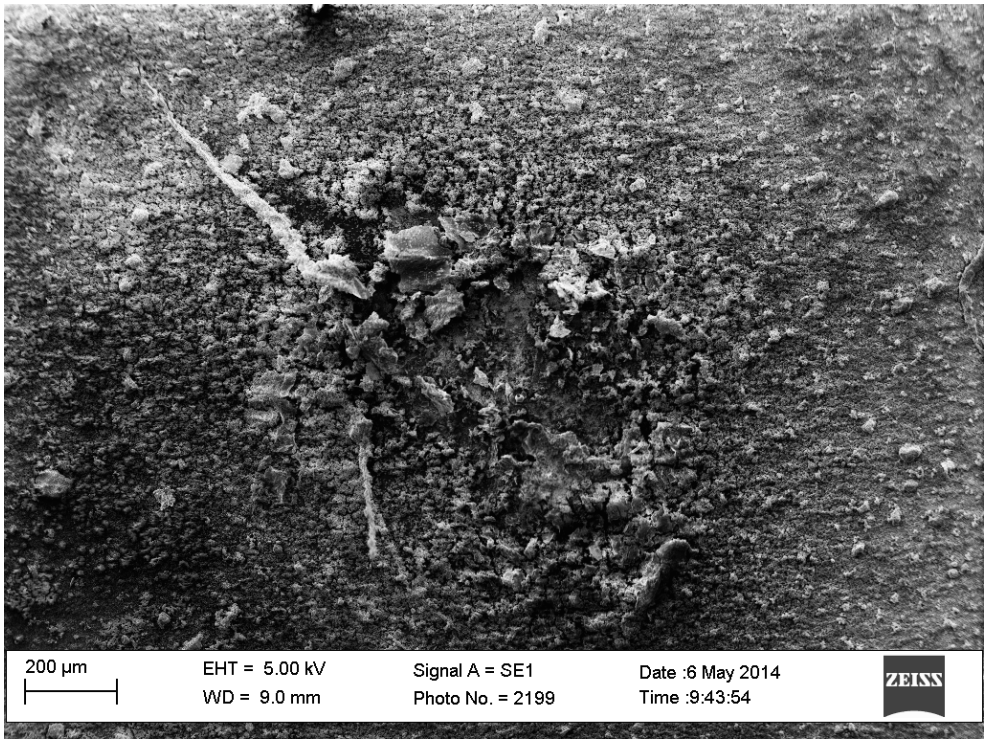

Figure 72. A SEM image of PANI Lap CP-E film (scale bar = 200 µm). The thicker region at the center was investigated for all images shown here.

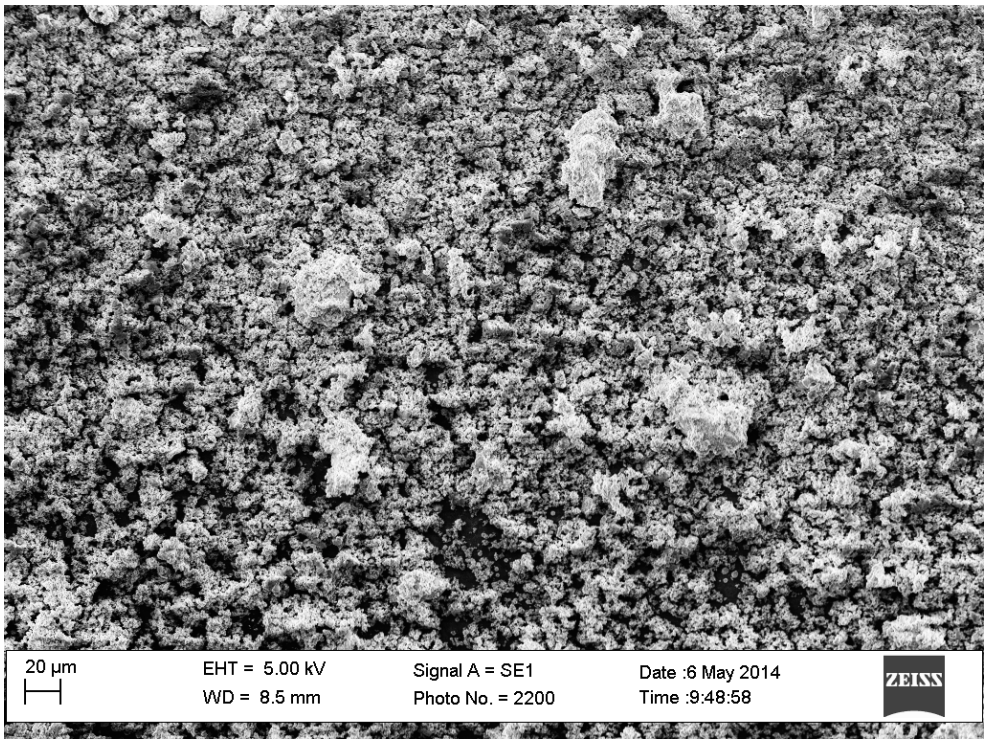

Figure 73. A SEM image of a close-up of Figure 72 showing thick polymeric growth (scale bar = 20 µm).

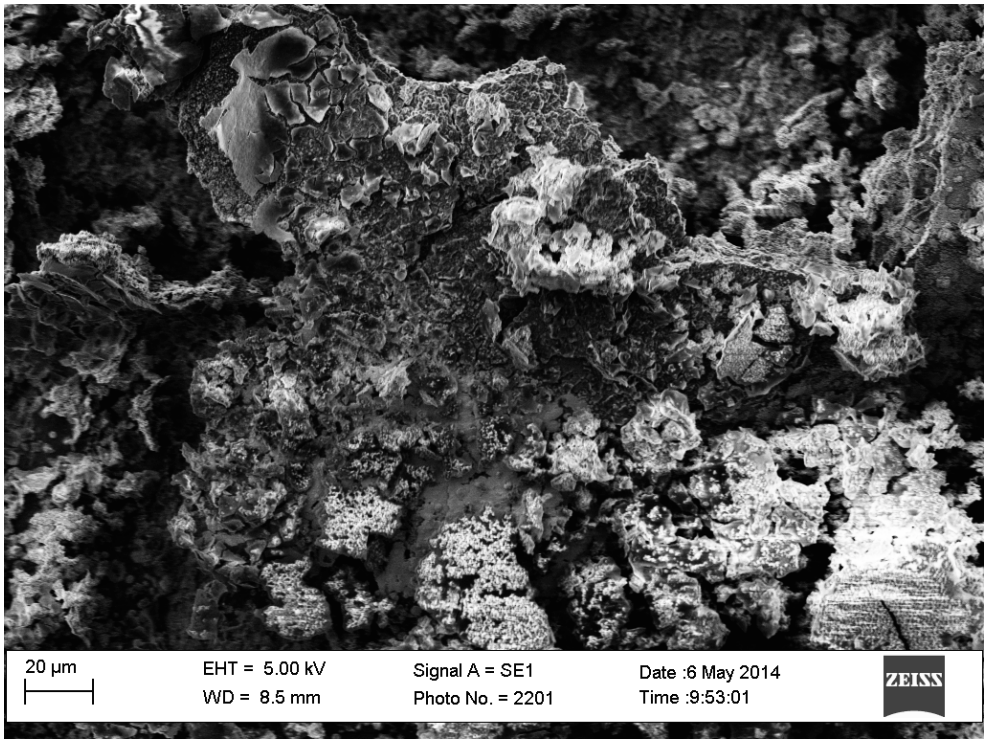

Figure 74. A SEM image of a large structure covered in sheet-like morphology is also covered in what may be Laponite nanodiscs at the bottom center (scale bar = 20 µm).

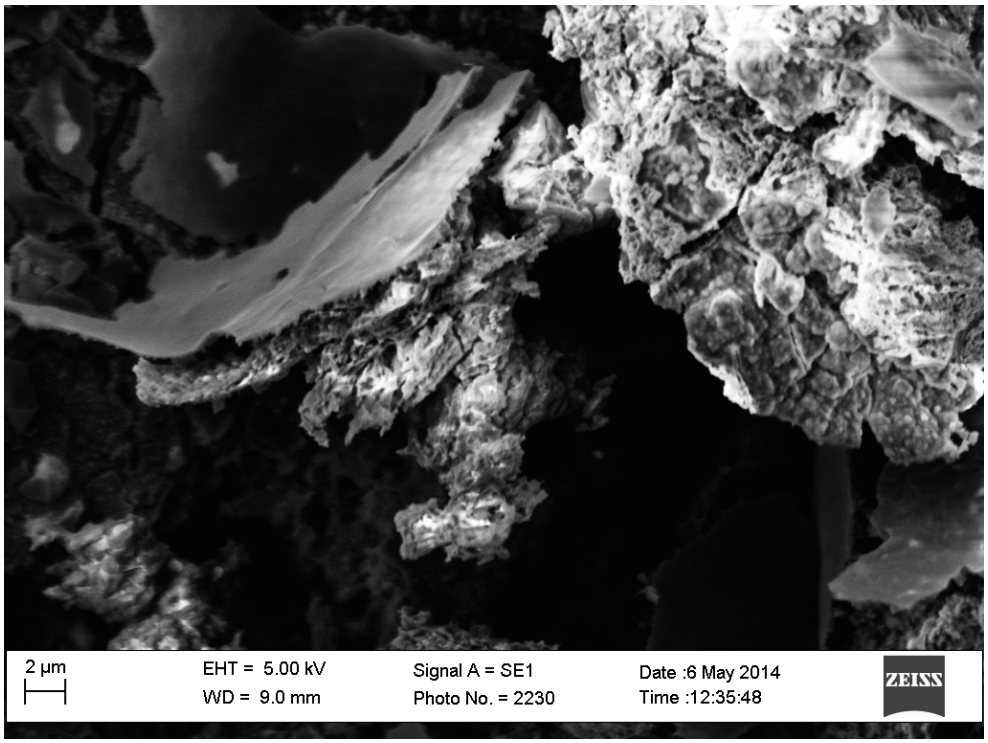

Figure 75. A SEM image of a sheet (scale bar = 2 µm). Polymeric growth can be seen off of one side, and lamellar stacking is apparent in the crystal below the sheet.

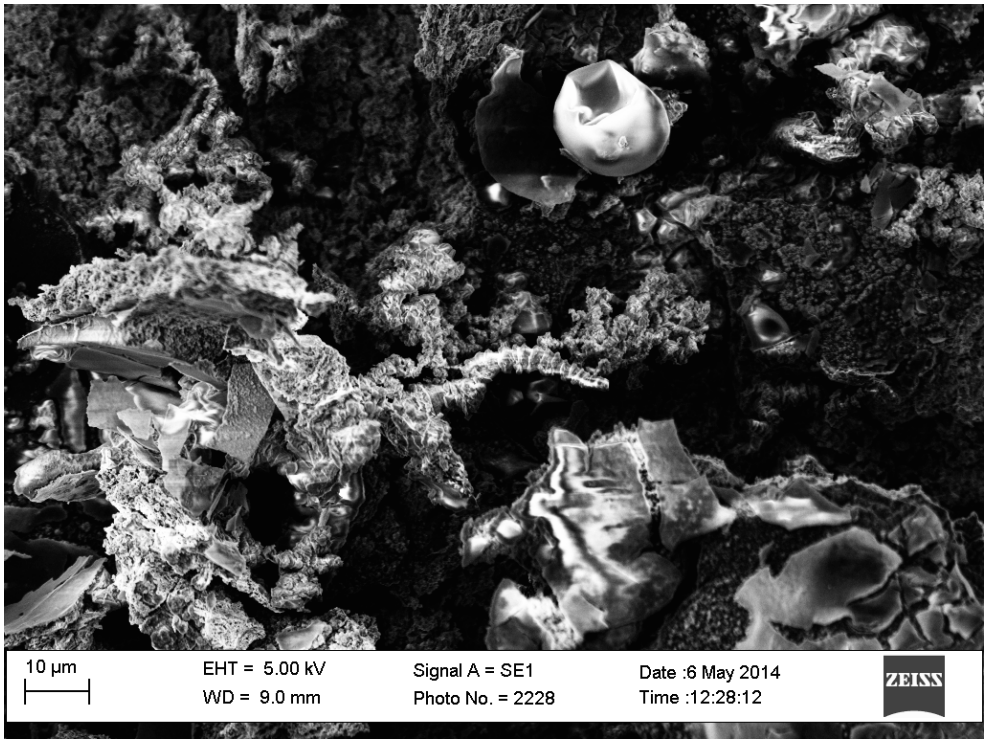

Figure 76. A SEM image of wires-upon-wires growth and a PANI hollow sphere (scale bar = 10 µm).

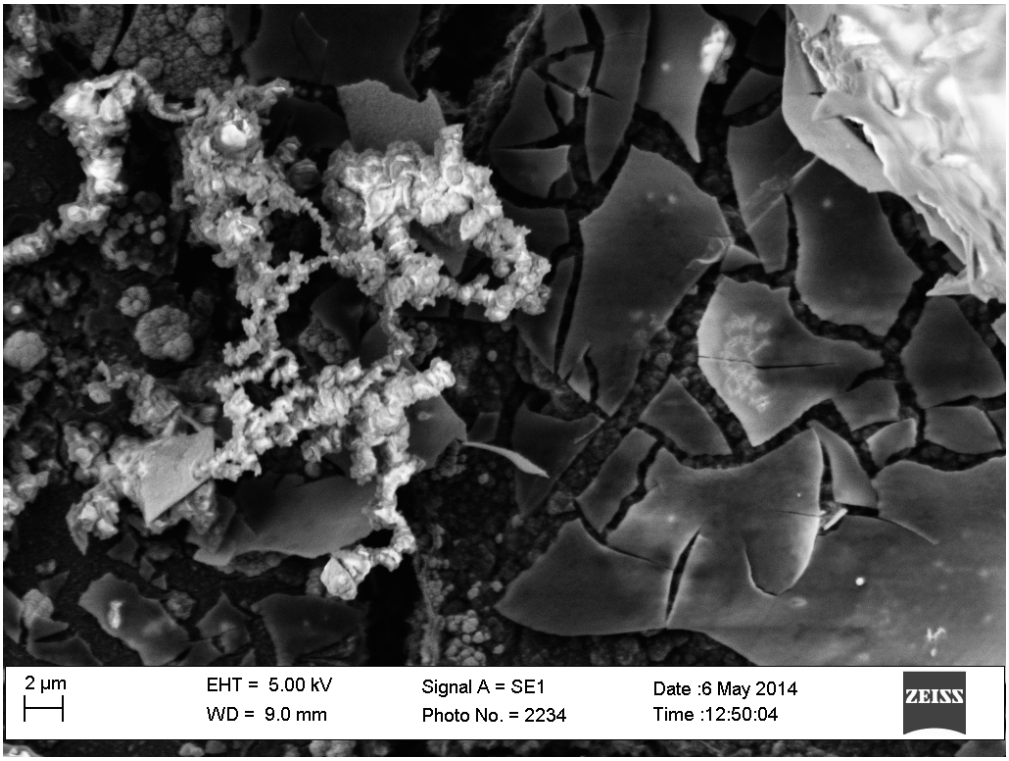

Figure 77. A SEM image of wires-upon-wires growth (scale bar = 2 µm).

4. Conclusions and Future Work

We have successfully created the first example of a bicontinuous conductive polymer network for use in hybrid QD-polymer solar cells via a mechanochemical route. This bicontinuous network is made up of polyaniline and a dicyanoaurate-based coordination polymer, is templated by Cu^{2+} Laponite RD, and can easily be extended to a tricontinuous network by the addition of PEDOT:PSS. In addition, it is our hope that the Au atoms in the CP will allow for facile attachment of evenly dispersed CdSe QDs.

Films cast from Lap CP, PANI CP, and PANI Lap CP reveal numerous different morphologies ranging from porous polymer networks to hollow spheres to nanoflowers. Control over these morphologies may be important for incorporation into devices. Various morphosynthetic parameters can be easily varied to obtain different morphologies. Testing the materials obtained through changing these morphosynthetic parameters through photoconductive atomic force microscopy (pcAFM)[36] and bulk conductivity measurements will allow us to determine which morphologies lead to the highest device efficiencies. Bulk conductivity and pcAFM measurements should also be perfomed on existing samples and devices. BHJs were constructed based on the ratios of materials given in Table 1. The BHJs are optically transparent and blue in color (Figure 78). Conductivity measurements should also be carried out for these devices. Then, more devices can be constructed based on the successes and weaknesses of these devices.

In addition, electron diffraction spectroscopy (EDS) should be performed on composite samples. EDS is a type of SEM detection method that creates an elemental "map" of samples, showing where different elements are located. In particular, the

locations of where Au, Si, and N are concentrated will allow us to determine where CP, Lap, and PANI, respectively, are located in each sample.

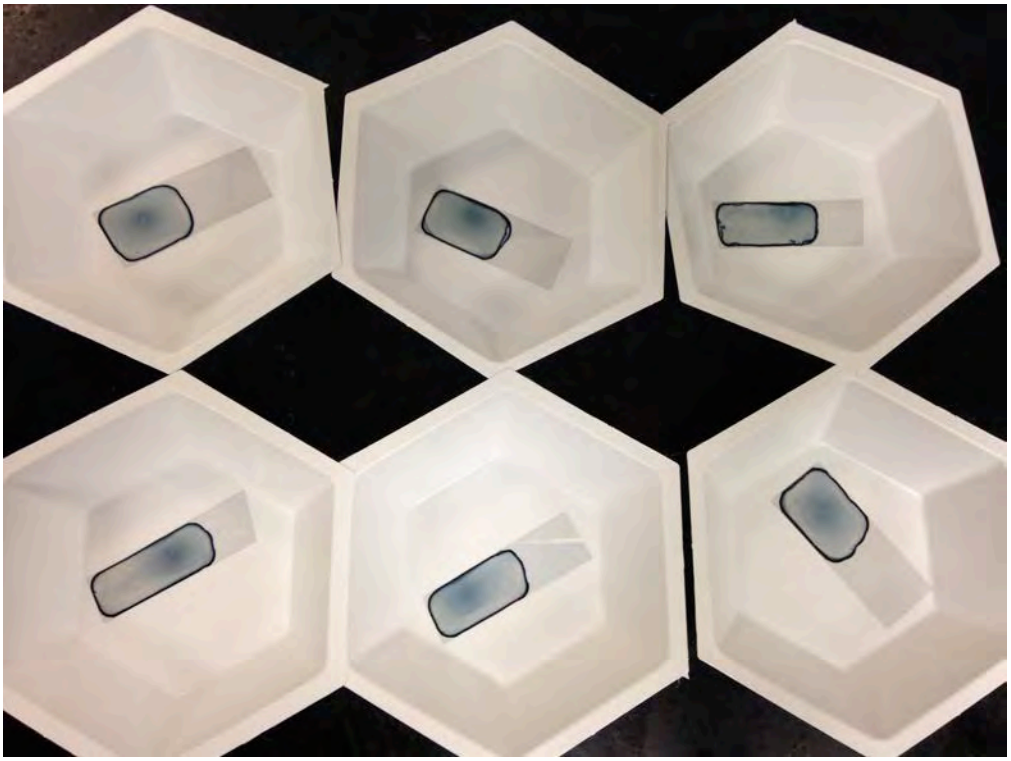

Figure 78. BHJs constructed based on the ratios of reagents in Table 1. Top, left to right: BHJ 1, 2, and 3. Bottom, left to right: BHJ 4, 5, and 6.

A recent area of interest to researchers is semiconducting perovskite solar materials. These materials are of interest as they have higher efficiencies than DSSCs or OPVs, are inexpensive and abundant, and have similar properties to bulk inorganic semiconductors.[37] The perovskite cells are generally based on organolead halide light-harvesting materials,[37-39] but recent work has also shown a large increase in efficiency by incorporating nanostructures such as ZnO nanorods[39] or TiO_2 nanosheets.[40] Some perovskite cells have also incorporated PCBM and PEDOT:PSS.[39] It would be interesting to try to incorporate our PANI/Lap CPs into a perovskite solar cell. The PANI and

Laponite nanostructures may serve to increase device efficiency in a similar fashion to the ZnO nanorods or TiO_2 nanosheets.

The incorporation of QDs into the bicontinuous network is another major undertaking. The QDs can also be functionalized with Ruthenium bipyridene (Rubipy), a Ru dye used to sensitize the QD, and with linkers to attach the QD to the CP. Once that has been done, we can determine whether the most efficient device is made using QDs alone, Rubipy-functionalized QDs, or Rubipy alone.

Finally, morphosynthetic strategies should be explored in the mechanochemical synthesis. Mechanochemical reactions have many advantages over their corresponding solvent-based reactions, especially in green chemistry, so optimizing these reactions to yield more efficient solar cells would be beneficial. The first interesting parameter to change is temperature. It has been shown that colder temperatures produce PANI with very different morphologies.[41] If the agate mortar and pestle were first cooled with liquid nitrogen before grinding, or if the grinding were performed in a cold room, we would likely see different morphologies than those that were seen from the room temperature grinding. Another morphosynthetic parameter is the PANI oxidant. We have already seen that PANI oxidized with Cu^{2+} has a very different morphology than PANI oxidized with Fe^{3+}. It would be interesting to incorporate a different metal into the CP backbone and see how the morphology of the entire composite changes, as well. Other morphosynthetic parameters to vary include time of grinding and grinding in a ball mill instead of a mortar and pestle.

5. REFERENCES

1. Prashant V. Kamat. *J. Phys. Chem. C.,* **2007**, *111* (7), 2834-2860.
2. **a.** Nathan S. Lewis and Danial G. Nocera. *Proc. Nat. Acad. Sci.,* **2006**, *103* (43), 15729-15735. **b.** Energy Information Association, *Renewable Energy Consumption and Electricity Preliminary Statistics 2008,* Table 1: U.S. Energy Consumption by Energy Source, 2004-2008.
3. Michael Grätzel. *Nature*, **2001**, *414*, 338-344.
4. "PV Education." www.pveducation.org. 16 March 2014.
5. Sen Zhang, Chunyan Ji, Zuqiang Bian, Pingrong Yu, Luhui Zhang, Dianyi Liu, Enzheng Shi, Yuanyuan Shang, Haitao Peng, Qiao Cheng, Dong Wang, Chunhui Huang, and Anyuan Cao. *ACS Nano*, **2012**, *6* (8), 7191-7198.
6. R. C. Nelson. *J. Phys. Chem.*, **1965**, *69* (5), 714-718.
7. Anders Hagfeldt, Gerrit Boschloo, Licheng Sun, Lars Kloo, and Henrik Pettersson. *Chem. Rev.*, **2010**, *110* (11), 6595-6663.
8. **a.** *NPG Asia Materials, Nature*, 2009. < http://www.nature.com/am/journal/v1/n1/full/am200914a.html)>. **b.** Brian O'Regan and Michael Grätzel. *Nature*, **1991**, *353*, 737-740.
9. Dianyi Lui, Mingyan Zhao, Zuquiang Bian, Luhui Zhang, Yuanyuan Shang, Xinyuan Xia, Sen Zhang, Daqin Yun, Zhiwei Liu, Anyuan Cao, and Chunhui Huang. *ACS Nano*, **2012**, *6* (12), 11027-11034.
10. Fang Zhang, Simiao Niu, Wenxi Guo, Guang Zhu, Ying Liu, Xiaoling Zhang, and Zhong Lin Wang. *ACS Nano*, **2013**, *7* (5), 4537–4544.
11. Tao Chen, Shutao Wang, Zhibin Yang, Quanyou Feng, Xuemei Sun, Li Li, Zhong-Sheng Wang, and Huisheng Peng. *Angew. Chem. Int. Ed.*, **2011**, *50*, 1815-1819.
12. Tao Chen, Longbin Qiu, Zhenbo Cai, Feng Gong, Zhibin Yang, Zongsheng Wang, and Huisheng Peng. *Nano Lett.*, **2012**, *12*, 2568-2572.
13. Wenxi Guo, Chen Xu, Xue Wang, Sihong Wang, Caofeng Pan, Changjian Lin, and Zhong Lin Wang. *J. Am. Chem. Soc.,* **2012**, *134* (9), 4437-4441.
14. Wenxi Guo, Chen Xu, Guang Zhu, Caofeng Pan, Changjian Lin, and Zhong Lin Wang. *Nano Energy*, **2012**, *1*, 176-182.
15. Biswajit Ray and Muhammad A. Alam. *Solar Energy Mater. & Solar Cells,* **2012**, *99*, 204-212.
16. Minh Trung Dang, Lionel Hirsch, Guillaume Wantz, and James D. Wuest. *Chem. Rev.,* **2013**, *113*, 3734-3765.
17. Alexander L. Azner, Christopher J. Tassone, Sarah H. Tolbert, and Benjamin J. Schwartz. *J. Phys. Chem. C.,* **2009**, *113* (46), 20050-20060.
18. Serap Günes, Helmut Neugebauer, and Niyazi Serdar Sariciftci. *Chem. Rev.*, **2007**, *107* (4), 1324-1338.
19. Prashant V. Kamat. *J. Phys. Chem. Lett.* **2013**, *4*, 908-918.
20. Martin K. Beyer and Hauke Clausen-Shaumann. *Chem. Rev.*, **2005**, *105* (8), 2921-2948.
21. Csaba Jobbágy, Tünde Tunyogi, Gábor Pálinkás, and Andrea Deák. *Inorg. Chem.*, **2011**, *50* (15), 7301-7308.

22. Ana Lazuen Garay, Anne Pichon, and Stuart L. James. *Chem. Soc. Rev.*, **2007**, *36*, 846-855.
23. Mary M. Caruso, Douglas A. Davis, Qilong Shen, Susan A. Odom, Nancy R. Sottos, Scott R. White, and Jeffrey S. Moore. *Chem. Rev.*, **2009**, *109* (11), 5755-5798.
24. Norbert Stock and Shyam Biswas. *Chem. Rev.*, **2012**, *112* (2), 933-969.
25. Maria Klimakow, Peter Klobes, Andreas F. Thünemann, Klaus Rademann, and Franziska Emmerling. *Chem. Mater.*, **2010**, *22* (18), 5216-5221.
26. Jiaxing Huang, James A. Moore, J. Henry Acquaye, and Richard B. Kaner. *Macromolecules*, **2005**, *38*, 317-321.
27. Henry D. Tran, Julio M. D'Arcy, Yue Wang, Peter J. Beltramo, Veronica A. Strong, and Richard B. Kaner. *J. Mater. Chem.*, **2011**, *21*, 3534-3550.
28. Dan Li, Jiaxing Huang, and Richard B. Kaner. *Acc. Chem. Res.*, **2009**, *42* (1), 135-145.
29. Dan Li and Richard B. Kaner. *J. Am. Chem. Soc.*, **2006**, *128*, 968-975.
30. BYK Additives and Instruments. "Technical Inormation B-RI 21: Laponite Performance Additives." **2014**.
31. **a.** Daniel B. Leznoff and Julie Lefebvre. *Gold Bulletin*, **2005**, *38* (2), 47-54. **b.** Takashi Okubo, Naoya Tanaka, Haruho Anma, Kyung Ho Kim, Masahiko Maekawa, and Takayoshi Kuroda-Sowa. *Polymers*, **2012**, *4*, 1613-1626. **c.** Mangayarkarasi Nagarathinam, Jialin Chen, and Jagadese J. Vittal. *Crystal Growth and Design*, **2009**, *9* (5), 2457-2463. **d.** Lijuan Zhang, Yunze Long, Zhaojia Chen, and Meixiang Wan. *Adv. Funct. Mater.*, **2004**, *14* (7), 693-698. **e.** Nanjundan Ashok Kumar, Hyuan-Jung Choi, Yeon Ran Shin, Dong Wook Chang, Liming Dai, and Jong-Beom Baek. *ACS Nano*, **2012**, *6* (2), 1715-1723.
32. Joanne D. Kehlbeck, Michael E. Hagerman, Brian D. Cohen, Jennifer Eliseo, Melissa Fox, William Hoek, David Karlin, Evan Leibner, Emily Nagle, Michael Nolan, Ian Schaefer, Alexandra Toney, Michael Topka, Richard Uluski, and Charles Wood. *Langmuir*, **2008**, *24* (17), 9727-9738.
33. Nan-Rong Chiou, L. James Lee, and Arthur J. Epstein. *Chem. Mater.*, **2007**, *19* (15), 3589-3591.
34. Zhirui Guo, Yu Zhang, Aiqun Xu, Meng Wang, Lan Huang, Kang Xu, and Ning Gu. *J. Phys. Chem. C*, **2008**, *112* (33), 12638-12645.
35. **a.** Bernadette Peace, Michael Topka, Kenneth Skorenko, Adam Kowalski, Ursula Williams, Michael Hagerman, and Rebecca Cortez. *Mat. Lett.*, **2011**, *65*, 3208-3211. **b.** Shiyong Zhang, Shuaijun Yang, Jingbo Lan, Yurong Tang, Ying Xue, and Jingson You. *J. Am Chem. Soc.*, **2009**, *131* (5), 1689-1691.
36. David C. Coffey, Obadiah G. Reid, Deanna B. Rodovsky, Glenn P. Bartholomew, and David S. Ginger. *Nano Lett.*, **2007**, *7* (3), 738-744.
37. Giles E. Eperon, Victor M. Burlakov, Alain Goriely, and Henry J. Snaith. *ACS Nano*, **2014**, *8* (1), 591-598.
38. Dae-Yong Sun, Jeong-Hyeok Im, Hui-Seon Kim, and Nam-Gyu Park. *J. Phys. Chem. C.*, Article ASAP.

39. Jingbi You, Ziruo Hong, Yang (Michael) Yang, Qi Chen, Min Cai, Tze-Bin Song, Chun-Chao Chen, Shirong Lu, Yongsheng Liu, Huanping Zhou, and Yang Yang. *ACS Nano*, **2014**, *8* (2), 1674-1680.
40. Liotz Etgar, Peng Gao, Zhaosheng Xue, Qin Peng, Aravind Kumar Chandiran, Bin Liu, Md. K. Nazeeruddin, and Michael Grätzel. *J. Am. Chem. Soc.*, **2012**, *134* (42), 17396-17399.
41. Hui-yan Ma, Yun-wu Li, Shen-xue Yang, Fei Cao, Jian Gong, and Yu-lin Deng. *J. Phys. Chem. C.*, **2010**, *114* (20), 9264-9269.